UNIVERSITÀ DEGLI STUDI DI MODENA
E REGGIO EMILIA

International Doctorate School in Information and Communication Technologies XXVIII cycle

DEPARTMENT OF ENGINEERING ENZO FERRARI (DIEF)
VIA UNIVERSITÀ 4 – 41121 – MODENA (I)
TEL. 059-2056511 • FAX 059-245156

Design and accurate characterization of a wireless, wearable and real time Active Personal Dosimeter for healthcare applications

Daniel Magalotti

Relatore:
Prof. Giovanni Verzellesi

Coordinatore:
Prof. Giogio Matteo Vitetta

Correlatori:
Ing. Pisana Placidi

A.A. 2014/2015

Abstract

Wireless Sensor Networks (WSN) are an important technology for large-scale monitoring, providing sensor measurements at high temporal and spatial resolution. In healthcare applications, a variety of system Prototypes and commercial products have been designed with the aim to provide an alternative and more efficient method for real time patient monitoring. For such applications, design constraints are limited for energy, network capacity (short communication range and low bandwidth) and processing and memory resources in each node.

In this work, a novel approach to perform on-line monitoring of the operators (surgeons and technicians) by using a device based on an Active Pixel Sensor (APS) during Interventional Radiology (IRad) procedures has been considered. The work has been performed in the framework of the Real-Time Active PIxel Dosimetry (RAPID) INFN Italian project.

The Interventional Radiology is a well-established technique in medical domain aiming to obtain a good X-ray image quality while minimizing the radiation dose absorbed by patients and operators. From a radioprotection point of view, these procedures are considered potentially harmful for the operators then individual monitoring is mandatory and it is performed by assessing effective dose, equivalent dose to the extremities and eye lens, by using passive dosimeters (e.g. Thermoluminescient Dosimeter (TLDs)) calibrated in terms of personal dose equivalent $H_P(10)$, $H_P(0.07)$ and $H_P(3)$, respectively.

In this work, we describe the design of a dedicated WSN for real time monitoring of the absorbed dose by the operators during the different IRad procedures that shows the possibility to achieve data delivery over wireless networks deployed in clinical environments. First the study and characterization of an image CMOS sensor as an X-ray detector has been described. The performance of the sensor has been evaluated with a proper experimental setup: the number of detected photons in a sensor frame and the sum of the reconstructed photon signals in a sensor frame have been assessed as dosimetric observables from frames acquired by the sensor using a two-threshold modified photon counting algorithm.

Then the implementation of different versions of the system prototypes has been described with the aim to decrease the power consumption and improve the portability of the final system. Both system response and algorithm performance have been investigated and consistency with results obtained using the same model of CMOS sensor with its own acquisition system provided by the manufacturer has been demonstrated. Moreover, the correlation of these observables with passive dosimeter dose measurements has been analyzed: a good linearity has been demonstrated, and the response difference between pulsed and continuous operational modes is reduced to less than 10%, marking a distinct improvement with respect to commercial Active Personal Dosimeters (APDs).

Finally, the experimental characterization of the prototype has been performed by using the system during several IRad procedures. The wireless link of the prototype has been characterized by measuring the Packet Error Rate (PER) of the network in different scenarios: the worst case result was lower than 0.4%, which is acceptable for the specific application. A linear correlation has also been observed between the observables during working conditions. The measurements of the absorbed dose have been calculated for different IRad procedures and compared with the response of the passive dosimeters. The measured points lie on a line with slope equal to one, showing that the systems can be used to perform both a real time monitoring of dose-rate and also to measure the total absorbed dose of the operators.

Acknowledgements

Un traguardo così importante non si raggiunge mai da soli. Per questo desidero ringraziare tutti coloro che mi hanno aiutato nella realizzazione della stesura della tesi.

Pisana che ha insistito nel farmi intraprendere il percorso di dottorato e che alla fine devo ringraziare due volte sia per avermi dato la possibilità di imparare tante cose (prima fra tutti l'analisi dati), sia per avermi trasmesso come riuscire a riassumere e a valorizzare il lavoro.

Leonello che aveva sempre il grafico giusto (forse anche troppi) al momento giusto. Nei suoi discorsi di statistica mi sono sempre perso dopo pochi minuti ma alla fine ho capito che "stare dentro le barre di errore" è quello che conta. Inoltre non è descrivibile la soddisfazione nel riuscire nell'impresa di fare un sistema "a prova di Leonello".

Lucia collega e amica che mi ha supportato sia nell'analisi dati che nei momenti di buio in cui il sistema finale era un miraggio; molto lavoro è stato possibile grazie al suo contributo.

Andrea Calandra che con la sua precisione e devozione al lavoro ha fornito un supporto fondamentale al progetto; non è facile racchiudere la professionalità, la cultura e l'umiltà in una sola persona, ma lui ci è riuscito.

Il prof. Scorzoni che ha corretto in dettaglio tutti gli articoli ma non è riuscito nell'impresa più ardua (sinceramente independent of/from non ho ancora capito quando vanno usati). I suoi consigli/correzioni/precisazioni sono stati sempre preziosi.

Ringrazio inoltre tutti coloro che hanno partecipato al progetto, i dosimetristi, in particolare Roberto C., con il suo piatto di linguine al cartoccio, i fisici medici, i dottori Maselli e Scarpignato e tutto il team, che sono stati sempre disponibili ad indossare di tutto permettendo di raccogliere una enorme quantità di dati; il prof. Verzellesi sempre pronto con il semaforo verde; i tesisti che hanno attivamente preso parte al progetto, Francesco con il disegno del primo prototipo, Marco con l'ottimizzazione del firmware del microcontrollore e Luca con l'implementazione dell'interfaccia grafica.

Infine un ringraziamento particolare va alla mia futura moglie che mi è stata sempre accanto sopportando soprattutto tutti i momenti più difficili e le noie di questo percorso. Questo lavoro e la felicità di essere arrivato a questo traguardo sono dedicati a te nella speranza che sia solamente il primo di una grande e bella lunga serie. Che Dio ti benedica.

Ultimo, ma non ultimo, una dedica particolare va al mio cagnolino *Forest* (o Tino, o Tuco, o Frustino) che ha dimostrato un vero ed attivo interesse sull'argomento.

Summary

Index of Figures

Index of Tables

List of Acronyms

ADC	Analog to Digital Converter
AmI	Ambient Intelligence
APD	Active Personal Dosimeter
APS	Active Pixel Sensor
BAN	Body Area Network
CMOS	Complementary Metal Oxide Semiconductor
COTS	Commercial Off-The-Shelf
CPLD	Complex Programmable Logic Device
CT	Computed tomography
DSA	Digital Subtraction Angiography
DIS	Direct Ion Storage
ECG	Electrocardiogram
EEG	Electroencephalogram
EMG	Electromyogram
EURATOM	European Atomic Energy Agency
GUI	Graphical User Interface
HEP	High Energy Physics
ICRP	International Commission on Radiological Protection
ICRU	International Commission on Radiation Units and Measurements
IRad	Interventional Radiology
ISM	Industrial Scientific Medical
Kerma	Kinetic Energy Released per unit

	MAss
LTCC	Low Temperature Cofired Ceramic
MAPS	Monolithic Active Pixel Sensor
MEMS	Micro-Electro-Mechanical System
MIP	Minimum Ionizing Particle
MOSFET	Metal-Oxide-Semiconductor Field-Effect Transistor
NFC	Near Filed Communication.
NSF	Number of Signal Frame
PER	Packet Error Rate
PMMA	Poly Methyl Methacrylate
PSN	Analog to Digital Converter
QoS	Quality of Service
RAPID	Real Time Active PIxel
RAPS	Radiation Active Pixel Sensors
RFID	Radio Frequency IDentification
SoC	System on Chip
SQNR	Signal-to-Quantization Noise Ratio
TL	Thermoluminescent
TLD	Thermoluminescent dosimeter
UVB	Ultra Wide Band
VGA	Video Graphics Array
VLSI	Very Large Scale Integration
WBAN	Wireless Body Area Network
WHO	World Health Organization
WLAN	Wireless Local Area Network
WMAN	Wireless Metropolitan Area Network

WPAN	Wireless Personal Area Network
WSN	Wireless Sensor Network
WWAN	Wireless Wide Area Network

Introduction

Tecnhologies advances on wireless communication and embedded systems have driven the development of portable devices with the characteristics of being small size, low-power and low cost to communicate over a short distance. The portable devices are typically part of a Wireless Sensor Network (WSN) and they are designed as ad hoc solutions for specific or generic nodes in a wide range of applications including smart homes, security, and personal healthcare.

Typically the resource constraints of the WSN are limited about several aspects such as the amount of energy, the network capacity (short communication range and low bandwidth) and the processing capability, and strongly depend on the specific application. In healthcare applications several examples in the literature have shown the potential of WSNs in developing applications such as real time patient monitoring in hospitals, monitoring of physiological parameters or fatigue tracking.

The research reported in this thesis is focused on the radiation protection techniques of the medical operators during the Interventional Radiology (IRad) procedures. Different solutions have been proposed for applications in radiation protection, where dose monitoring is a fundamental issue for patients and operators (surgeons and technicians). The exposure to ionizing radiation of the operators could be high in some applications, and could even result in harmful effects if appropriate measures for occupational rotation are not implemented. International guidelines have defined limits for equivalent dose and effective dose to be absorbed by staff members and this restricts the number of procedures that they can undertake during a given time interval.

As the benefits for the patients increase, the use of radiation in medicine exposes not only the patients but also the operators to a personal health risk during the work activity. In several international forums, among which the ORAMED project, the necessity to provide a real time measurement of the absorbed dose of the operator during the medical procedures has been highlighted.
Passive dosimeters are currently the only certified devices used for measuring individual dose. The main drawback of such devices is their inability to provide a real time measurement, as they are read at fixed time periods (e.g. once a month). On the other hand, semiconductor based active personal dosimeters are commercially available but it was pointed out that these are not the most suitable devices for IRad applications, because of the peculiarity of the scattered X ray radiation to which operators are exposed.
In the framework of the Real time Active PIxel Dosimetry (RAPID) project of the Italian Institute for Nuclear Physics (INFN), we aim to develop a portable device, called Personal Sensor Node (PSN), for the dosimetry of IRad operators with the following requirements: *i)* on line monitoring of staff operation producing an alarm when the dose exceeds a warning level; *ii)* off line storage of dose measurements in order to correlate them with the specific activities of the staff, optimizing the number and type of procedures that interventionists can undertake.
The device, based on the use of a CMOS image sensor as X ray radiation detector, was designed to overcome energy and bandwidth limitations by using a digital signal processing unit to perform an intelligent pre-processing of the data. A dedicated hardware was developed with the goal of retrieving, from sensor data frames, two different observables that are linearly correlated to dosimetric quantities and compatible with real time requirements.
A dedicated WSN has also been implemented that it consists of several PSNs monitoring the absorbed dose in different positions of the operator body (e.g. on

head or arms) to better understand the level of absorbed dose in the operator body. Each part of the body's operator is subject to different levels of radiation exposure whose measurements provide a necessary information to improve the radiation protection methods. The dose measurements can be compared with dose limits defined for each operator and can be used to identify criteria for workers to decrease the unnecessary exposure of the operators. In fact the system can also be used for education purposes of the operator correlating the absorbed dose rate with the activity of the operator and the radiographic settings during the different parts of the medical procedure.

The thesis is organized as follow: Chapter I describes the WSN applications with the focus on the monitoring systems developed for healthcare application and the Interventional Radiology application scenario; Chapter 2 deals with the basic concepts of X-ray dosimetry and the state of the art devices of passive and active dosimeters; Chapter 3 reports the characterization of the CMOS image sensor to be suitable as sensitive element for the X-ray radiation and the formal procedure to implement the data reduction algorithm to extract two observables correlated to the dosimetric quantities; Chapter 4 describes the architecture design of the system and the characterization in laboratory of the different prototypes realized to improve the power consumption and the portability of the final system; the analysis of the systems performances are explained in Chapter 5 during actual IRad procedures by measuring the wireless losses of the network and the collected signal in order to correlate the absorbed dose measurements with the passive dosimeters.

Chapter I

Wireless Sensor Networks and Healthcare monitoring applications

In this chapter, an introduction of the current technologies, mainly electronics and wireless infrastructure, used to design multi-functionality portable devices will be outlined. The systems developed to support the healthcare applications will be described and the constraints when designing a sensor node that operates in a Wireless Sensor Network (WSN) will be outlined. The attention will be focused on the use of radiation in medicine for imaging and therapy practice that exposes the medical staff to health risks especially during Interventional Radiology procedures. Then the radiation protection issue will be outlined by describing the strategic approaches proposed by the World Health Organization (WHO) to deliver practical tools to radiation medicine workers to protect medical staff. Finally the Interventional Radiology application scenario will be described by highlighting the X-ray tube characteristic and the radiation spectrum generated by the X-ray scattered from the patient's body.

I.1 State of the art

Recent advances in Micro-Electro-Mechanical Systems (MEMSs) technology, wireless communications, embedded systems and digital circuit electronics have stimulated the condition to develop low-cost, low-power, multifunctional portable sensor devices which can be used to observe and monitor physical phenomena [1].

The collaboration and synergy of sensing, processing and communication units is the basis to exploit the potentiality of this new technology. Despite the autonomy of these devices, the most powerful aspect is the definition of networks where these devices can co-operate according to various models and architectures. These networks, called WSNs, have led to research efforts in the areas of communications (protocols, routing, coding, error correction etc.), electronics (energy efficiency, miniaturization) and control (networked control system, theory and applications). Born on military application, WSN can be composed of several numbers (even thousand) of ad-hoc sensor nodes working together to accomplish a specific and common task. The design of the network is related to the specific application and to the characteristic of the external environment. Several applications have been provided by wireless sensors networks and could be classified under some general headings: military applications, environmental monitoring, healthcare applications and robotics [2].

In military applications, several areas are covered by wireless sensor networks such as enemy tracking, battlefield surveillance or intrusion detection and classification [3]. For example, mines may be regarded as dangerous and obsolete in the future and may be replaced by thousands of dispersed sensor nodes that will detect an intrusion of hostile units. Then, the prevention of intrusion will be the response of the defense system [4].

In environment applications, the capability of sensing temperature, light, status of frames (windows, doors), air streams and indoor air pollution can be used for example to control the indoor environment reducing the unnecessary heating or cooling of buildings [5].

In agriculture, the wireless sensor network can be used to enhance the productivity of cultivations by providing the capability to perceive and monitor real-time soil and weather information. The information is transmitted to a diagnosis decision center by a random self-organized wireless communication network, which provides remote monitoring and management of the agricultural environment [6].

Healthcare applications can also benefit from the use of wireless sensor networks. These systems can be used for monitoring and control the health status condition of the patient overcoming the energy and bandwidth limitations by using an intelligent preprocessing of the measurements collected by the different sensors. [7]. The overview of a simple wireless sensor network application scenario is depicted in Figure I-1.

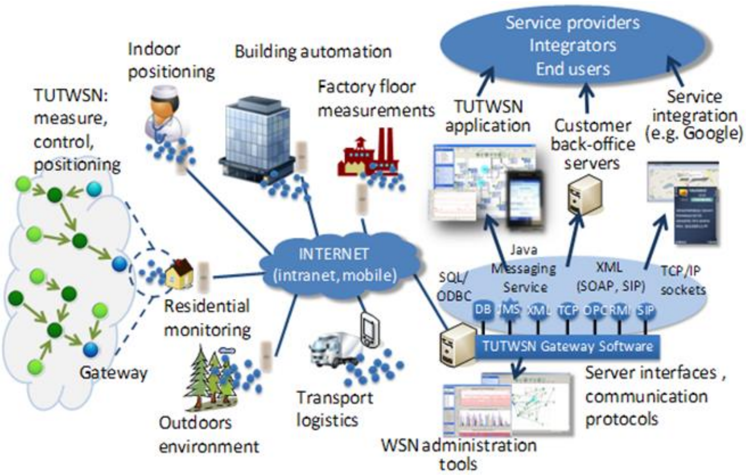

Figure I-1: Generic scenario of a Wireless Sensor Network.

Several WSNs operate autonomously in their environment and execute sensing, computing, and communication tasks. The WSN continuously collects measurements from a multiple-point network of sensor nodes while communicating with (and sending the information to) the base station which can be connected to a computer called system Gateway. The system Gateway redirects these data in a TCP/IP packet to a common database that collects physical measurements about the environment that can be accessed by users and other applications. The advantage of the database approach is that it provides a separation between the logical view of the data held by the sensor network and the actual implementation of these operations on the physical network.

The traditional networks, such as Wireless Local Area Network (WLAN) or cellular network, has the goal to optimize the Quality of Service (QoS) parameters to provide excellent throughput and higher bandwidth [8]. Otherwise the WSNs have their own design and resource constraints, which include limited amount of energy, limited network capacity (short communication range, low throughput, and low bandwidth) and reduced processing and storage resources in each node. Therefore the WSN is optimized for the specific application and the requirements, coupled with technology, lead to different hardware and software platforms developed with the goal to implement energy saving in order to increase the operational lifetime of devices.

A sensor network design is influenced by many factors, which include fault tolerance, scalability, transmission media, production costs, hardware constraints and power consumption. These factors can be used as a guideline to design and compare different schemes of WSN:

- The fault tolerance is the ability to sustain sensor network functionalities without any interruption due to sensor node failures. The failure of some sensor nodes should not affect the overall task of the sensor network [9]. Different schemes can be implemented to provide fault tolerance. Hardware backup schemes can be used to overcome hardware problems. Software techniques can be used to provide fault detection and fault tolerance. For example, multipath routing or provisioning of redundant connections can guarantee network connectivity when a node is not working.
- Scalability is referred to the number of sensors that a network can handle. The number of sensor nodes deployed in a specific application may be from

few units to the order of hundreds or thousands, and the designed schemes of a WSN must be able to work with this number of nodes [10].

TABLE I-1
FREQUENCY BANDS AVAILABLE FOR ISM APPLICATIONS [11].

Frequency band	Bandwidth	Application
6.765 MHz - 6.795 MHz	30 kHz	Fixed and Mobile services
13.553 MHz - 13.567 MHz	14 kHz	Fixed and Mobile services
26.957 MHz - 27.283 MHz	326 kHz	Fixed and Mobile services
40.66 MHz - 40.70 MHz	40 kHz	Fixed and Mobile services
433.05 MHz - 434.79 MHz	1.74 MHz	Amateur Radio, Mobile and Radar services
862 MHz - 890 MHz	26 MHz	Amateur Radio, Mobile and Radar services
2.4 GHz - 2.5 GHz	100 MHz	Fixed and Mobile, RFID and Wideband data transmission services
5.725 GHz - 5.875 GHz	150 MHz	Fixed and Mobile and Radio determination services
24.00 GHz - 24.25 GHz	250 MHz	Amateur Radio, Defense systems and Radio determination services
61.0 GHz - 61.5 GHz	500 MHz	Defense systems, Radio determination and Wideband data transmission services
122 GHz - 123 GHz	1 GHz	Amateur Radio and Microwave services
244 GHz - 246 GHz	2 GHz	Amateur Radio, Radar and Radio Astronomy services

- In a wireless sensor network, communicating nodes are linked by a wireless medium frequently by using radio links. One option for radio links is the use of Industrial, Scientific and Medical (ISM) bands, which offer license-free communication in most countries. Several frequency bands that may be made available for ISM applications are listed in TABLE I-1.

- Production costs are a very challenging issue, as matter of fact the sensor networks have to implement functionalities with a cost for the network lower than deploying traditional sensors.
- Power consumption and hardware constraints are strongly influenced due to the fact that the wireless sensor node can only be equipped with a limited power source and it influences the amount of functionalities that can be implemented directly on board. For this reason a lot of efforts are currently focusing on the design of power-aware protocols and algorithms for sensor networks to increase the operative lifetime of these devices [12].

I.1.1 The wireless sensor node

The sensor node is the basic component of a WSN and its main task is to sense, measure and gather information from the environment. The general block diagram of the system architecture has been reported in Figure I-2.

The architecture consists of four main blocks: a sensing unit, a processing unit, a communication unit and a power unit.

- *Sensing unit*. A specific sensor is used depending on the physical quantity that has to be monitored and recorded. Generally an Analog/Digital Converter (ADC) is integrated inside the sensor itself to digitalize the output data.
- *Processing unit.* A central processing unit extracts and collects raw data from the sensor. The complexity of the data elaboration and the algorithm implemented inside the processing unit is strongly related to the power consumption and the timing characteristic required by the specific applications. A memory resource could be used to increase the processing capability and to store the information before the transmission.

- *Communication unit.* A radio transceiver is used to implement wireless data transmission and to connect each node to the network. The collected data are sent to a remote PC where the data will be stored, displayed and analyzed.
- *Power unit.* The power unit is the most important component of the whole system. Because the aim is to increase the operation lifetime of the system, different solutions can be used, for example to turn off the radio transmission when it is not required or increase the amount of data elaboration on board before sending the information.

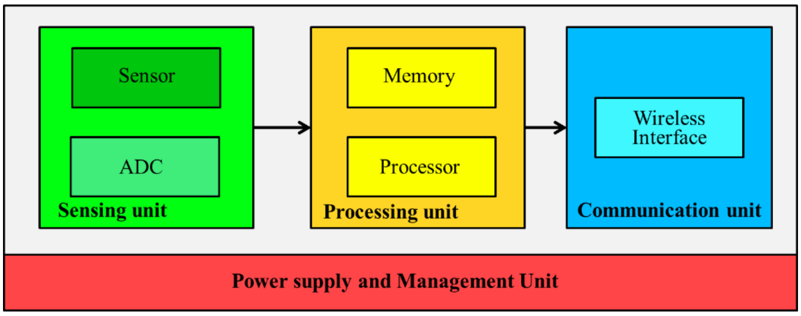

Figure I-2: Basic components of a sensor node in Wireless Sensor Network.

I.2 The Wireless Sensor Networks for healthcare applications

Healthcare is a big concern, since it involves the quality of life a given individual can have. The growing fraction of elderly population, which translates into an increasing demand for healthcare services, will be one of the major challenges of various healthcare systems. Population Reference Bureau [13] forecasts that in the next 20 years, the over 65 population in the developed countries will be nearly 20% of the overall population. Moreover, according to the WHO [14] in 2020 most of the diseases on a planetary scale will be due to chronic pathologies as diabetes, hypertension or cardiovascular diseases. The evolution of such pathologies requires numerous and expensive cares, then homecare associated to a remote medical monitoring and assistance becomes unavoidable. Traditionally, health monitoring is performed on a periodic check basis, where the patient must remember its symptoms and the doctor performs some checks and formulates a diagnostic and the treatment process.

In this context, new wireless technologies open up possibilities for providing real time feedback information about the health status condition, both to the patient himself and to a medical center that will be able to detect an emergency condition [15] and to generate an alert in case of possible health threatening conditions [16].

A new paradigm in information technology, called Ambient Intelligence (AmI) [17], in which sensors and processors will be integrated into everyday objects in order to create a sensitive, adaptive, and responsive environment suitable for human needs [18]. AmI aims to change the form of human-computer interaction, focusing on the user needs, in this way they can interact in a more seamless way with the available infrastructure.

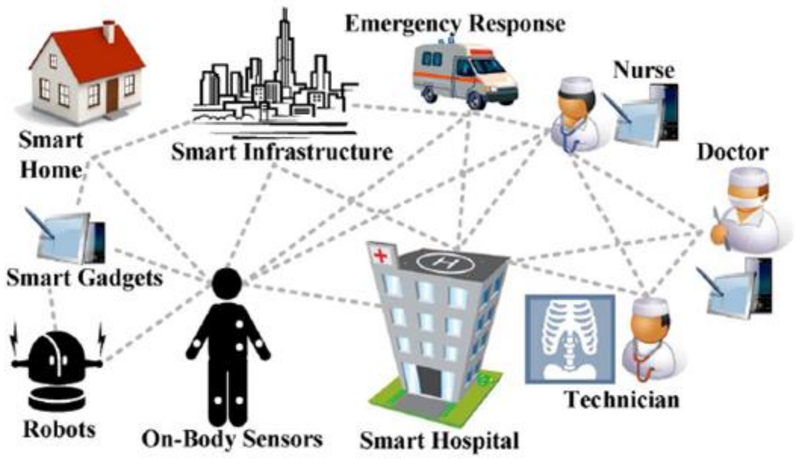

Figure I-3: Interconnection of AmI health services [18].

For example, AmI technology can be used to monitor the older adults health status or people with chronic diseases and it can provide assistive care for people with physical or mental limitations. In addition it can support the healthcare professionals in terms of providing innovative communication and monitoring tools. AmI promises the successful interpretation of the health status by means of contextual information obtained from such embedded sensors, and will adapt the environment to the user's needs in a transparent and anticipatory manner. Figure I-3 depicts how AmI systems might be used as cohesive services integrated into different environments and devices.

In the context of healthcare domain the wireless sensor network is referred to as Body Area Network (BAN), called also Wireless Body Area Network (WBAN). The BAN consists of an ad hoc network of intelligent low-power sensors and actuators which can be placed on the body or on the clothing of the humans [19]. TABLE I-2 summarizes the most common BAN applications [20].

The use of BAN infrastructures in medical field offers the possibility to implement applications for continuously monitoring health status parameters such as heartbeat, body temperature, physical activity, blood pressure, Electrocardiogram (ECG), Electroencephalogram (EEG), and Electromyogram (EMG). One of the most common physiological parameters is the body temperature that is extremely useful as indicator to detect symptoms of medical stress [21] which can determine various health condition such as stroke, heart attack and shock. Another common physiological parameter useful to monitor is the heart rate.

There are a lot of methods to measure heart rate, the most common and complete of which is the Electrocardiogram. Wearable ECG sensors provide useful information such as the rate and regularity of hearth beats used in diagnosis of cardiac diseases to detect a possible problem in advance [22]. An accelerometer is also used to monitor the human activity such as detection of falls [23], analysis of body motion [24] etc., measuring the acceleration along a definite axis and over a frequency range. The benefit of developing a BAN for healthcare applications can be identified in communication efficiency and costs reduction that can lead to expand the ubiquitous computing for healthcare applications [25].

TABLE I-2
APPLICATION OF BANS [19].

BAN application	Medical	Wearable BAN	Assessing Soldier Fatigue and Battle Readiness
			Aiding Professional and Amateur Sport Training
			Sleep Staging
			Asthma
			Wearable Health Monitoring
		Implant BAN	Cardiovascular Diseases
			Cancer Detection
		Remote Control of Medical Devices	Ambient Assisted Living (AAL)
			Patient Monitoring
			Tele-medicine Systems
	Non-Medical		Real Time Streaming
			Entertainment Applications
			Emergency (non-medical)

Two crucial aspects in developing such healthcare devices are the portability and the power consumption. The mobility of the patients is a crucial point since the patient wears the BAN devices all the time and a reduction of mobility is not acceptable. Moreover the total power consumption limits the amount of digital processing logic directly on board of the device and also the output transmission power.

The international standard IEEE 802.15.6 specifies the constraints for low power and short range wireless communications and considers the effects on portable antennas due to the presence of human body [26]. The most commonly employed wireless communication technologies suitable for a BAN are: Ultra Wide Band (UVB) [27], ZigBee and 802.15.4 [28], Bluetooth and Bluetooth Low Energy [29], and technologies like Radio Frequency IDentification (RFID) and Near Filed Communication (NFC) [30].

TABLE I-3
COMPARISON OF DIFFERENT IEEE COMMUNICATION PROTOCOL STANDARD [31].

Standard	Coverage Range	Data Rate	Frequency
Near Field Communication (NFC)	≈ 20 cm	106-424 kbps	13.56 MHz
Ultra Wide Band (UWB)	5-10 m	110-480 Mbps	3.1-10.6 GHz
RFID	1-100 m	10-100 kbps	125 kHz-134.2 kHz 13.56 MHz 860-960 MHz 2.45 GHz
ZigBee (IEEE 802.15.4)	100 m	250-500 kbps	868-915 MHz 2.4 GHz
BlueTooth (IEEE 802.15.1 WPAN)	10 m	1-3 Mbps	2.4 GHz
WiFi (IEEE 802.11 WLAN)	5 km	1-450 Mbps	2.4 GHz 3 GHz 7 GHz
WiMax (IEEE 802.11 WMAN)	15 km	75 Mbps	2.3 GHz 2.5 GHz 3.5 GHz

A comparison of different IEEE protocols currently available is shown in TABLE I-3 [31]. The choice on the most appropriate wireless standard for BAN system have to be made based on the specific requirements of the application. The requirements can be on power consumption, bandwidth for real time application, data rate and frequency. Figure I-4 reports different wireless technologies data rates as a function of power consumption.

Another important aspect that has to be considered in a wireless system is the interference of the surrounding objects with the transmission antenna. The electromagnetic interaction of the human body affects the antenna properties and the radio propagation, then different constraints have to be considered in the antenna design such as the limitation in shape, size and material type [32]. Moreover a BAN may be also interfaced with video systems, Wireless Personal Area Networks (WPAN), Wireless Local Area Networks (WLANs), the Internet and cellular networks (WWAN).

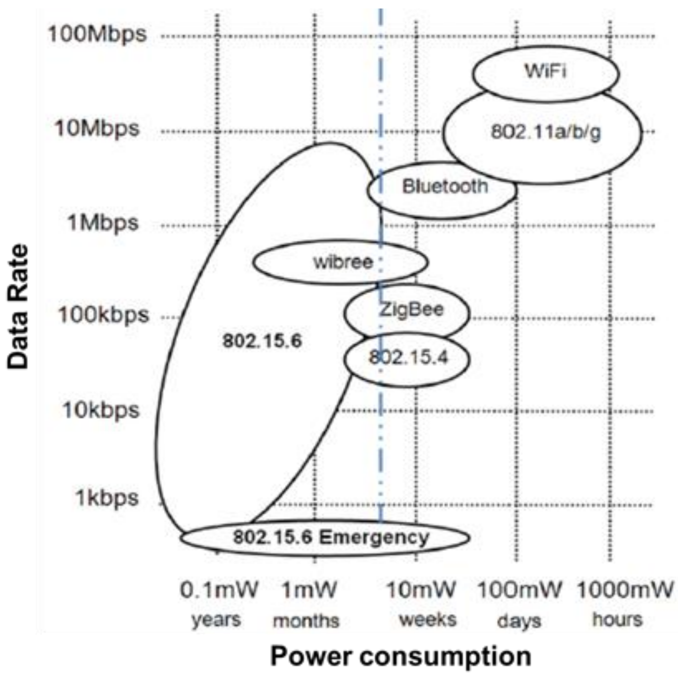

Figure I-4: Power consumption and data rate for different wireless technologies in a WBAN [19].

Figure I-5 shows the infrastructure layer that covers the range of communication from low-level to high-level design and enable the generation of an efficient BAN system for a wide range of applications. The communication of BAN with other wireless networks is a crucial point because the data have to be sent from the patients to the central health care system for monitoring health status conditions and to provide suitable solution in case of alerts [33].

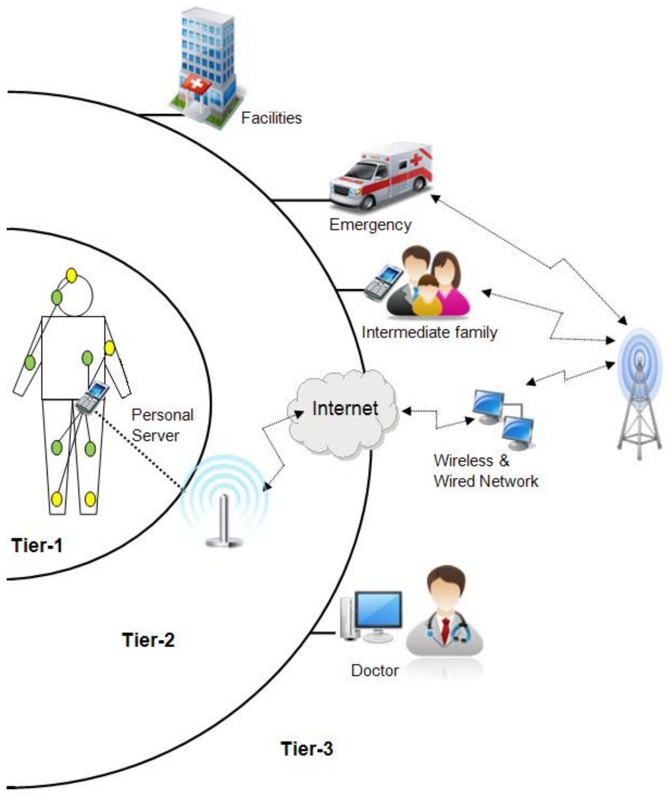

Figure I-5: The infrastructure of a BAN communication system [27].

A BAN operates close to the human body with a communication range of up to 1-2 meters. It primarily deals with the interconnection of wearable devices, whereas a

WPAN is a broader network for the surrounding environment and the communication range reaches up to 10 meters. However, WPANs do not fulfill medical and communication regulations for specific applications and they do not support the combination of data rate and reliability required for the broad range of WBAN applications. A WLAN has a communication range of up to 100 meters while WWANs cover the largest geographical region such as in mobile telephone systems and satellite communication [34].

I.3 Interventional Radiology application scenario

In the previous section, we have reported about the main technologies used in the healthcare applications to develop applications and systems that can improve the quality of life and services for the patients.

In the modern medical treatments there are an increasing use of ionizing radiation especially for imaging and therapy practice. Today, medical imaging helps to detect and diagnose diseases in earliest stages and facilitates the medical operator to determine the most appropriate and effective care where, previously, exploratory surgery was necessary to discover the cause of symptoms or the nature of diseases.

Although ionizing radiation carries risks as well as provides beneficial effects, its overall contribution is positive and, from a medical point of view, it is less harmful than exploratory surgery for the patients. As the benefits for patients increase, the use of radiation in medicine exposes not only the patient but also the medical staff to health risks during the working activity. While the development of modern health technology makes new applications safer, their inappropriate use can lead to unnecessary radiation exposition, and thus causing potential health hazards for both patients and staff [35].

Interventional Radiology refers to a range of techniques which involve the use of radiological image guidance to diagnostic and therapy. The activities of the operators include the diagnostic image interpretation and the manipulation of needles by using a tiny endoscope (a flexible tube) through a catheter placed in the patient's vein or artery to navigate around the body under imaging control. The effectiveness of treatment for these minimally invasive techniques is often better than the traditional surgery treatments due to the following reasons [36]:

- it provides less trauma to the body than does surgery;
- it requires less anesthesia and often it works in local anesthesia;
- it shortens the hospital stay and the recovery period meaning less cost for the hospital structure;
- it results in less pain as matter of fact the duration of recovery time is shorter than the classical surgery operation.

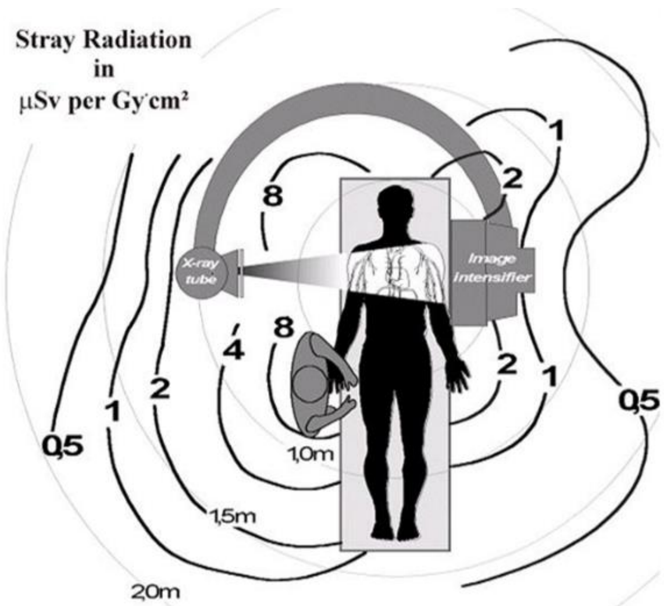

Figure I-6: The isodose for the diffused X-ray radiation generated by the scattered radiation from the patient’s body [37].

The reason why techniques exploit ionizing radiation to generate images of the body can induce health problems for the interventional operator (surgeon and technician) is due to the scattering of the X-ray beam by the patient's body in all directions so that it is partially absorbed by the operator that is located near the patient [38] (Figure I-6).

The absorbed dose measures the amount of energy imparted in a kilogram of mass received by the medical operators and it could be high in some applications, and could even result in deterministic or more probably stochastic effects if appropriate attention for radiation protection are not implemented [39].

The operator usually wears anti-X shields for radioprotection purposes; however the extremities, especially hands and eye lens, are often without protections since gloves and glasses are not always tolerated by the operator during the medical procedure. Then these parts of the body absorb, for each medical procedure, a dose even greater than 1 mSv with a dose-rate that can reach values about 0.5 mSv/s. (To understand the order of magnitude, a typical dose of a patient for a knee radiography and a mammography are 1-5 µSv and 0.4 mSv respectively).

The WHO proposed several strategic approaches by engaging and collaborating with stakeholders from the healthcare sector by delivering practical tools to radiation medicine workers to protect patients and themselves. Activities have been developed for radiation protection issues including:

- a better understanding of the risks in radiation medicine to underpin policy and decision making;
- a reduction of unnecessary medical radiation exposures;
- an enhancement of knowledge, skills and safety attitude of staff;
- a better prevention of unintended exposures;
- an increased awareness of the benefits and risks of the medical use of radiation among the stakeholders.

For the Interventional Radiology procedures, the scattered radiation depends on the spectrum and intensity of the X-ray beam used to obtain the diagnostic images.

There are many types of medical imaging procedures, each of which uses different technologies and techniques, for example: Computed tomography (CT), fluoroscopy, and radiography. All these techniques exploit ionizing radiation to generate images of the body: an X-ray beam is passed through the body where a portion of the X-ray photons are either absorbed or scattered by the internal structures, and the remaining ones are transmitted to a detector (e.g., films or specific sensible screens) for recording or further processing by a computer.

Focusing on fluoroscopy, this technique produces real-time moving images of the patient's internal structure by using an injection of contrast material, which makes arteries, veins and blood vessels show up more clearly under X-ray. Fluoroscopy is used for guidance in a number of medical procedures, including angiography, discography and image-guided biopsy.

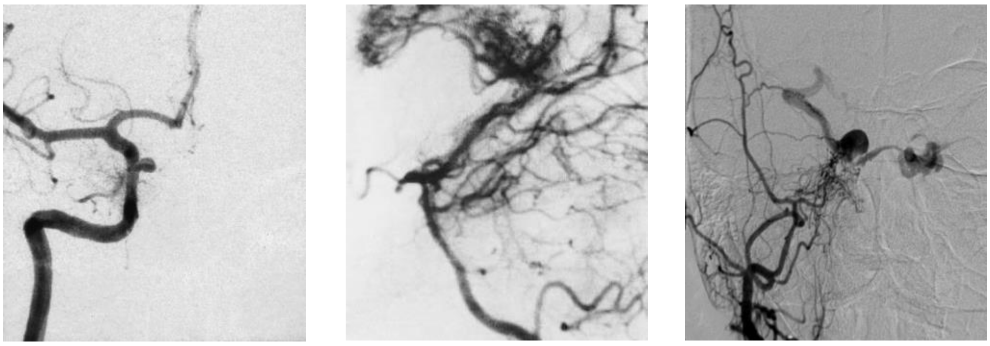

(a) (b) (c)

Figure I-7: Examples of different angiography procedures: (a) digital fluoroscopy [40]; (b) digital fluorography [41]; (c) DSA [42].

The following variations can be found during medical procedures:

- digital fluoroscopy (Figure I-7 (a)), featuring low exposure acquisitions with continuous or pulsed X-ray field. The resultant images feature low-medium resolution;
- digital fluorography (Figure I-7 (b)), featuring intense pulsed exposures, resulting in high resolution images;
- Digital Subtraction Angiography (DSA, Figure I-7 (c)), where acquisitions are performed before and after the injection of the contrast agent and the images are digitally subtracted. The DSA is a type of fluoroscopy technique.

The X-ray tube parameters such as tube voltage, tube current, pulse frequency and pulse width, can be varied to optimize the acquired images depending on the different IRad procedures. An example of combinations of these parameters is summarized in TABLE I-4 for different procedures.

Two modalities of the X-ray tube can be arranged by the operator during the IRad procedures:

- *continuous mode*: the X-ray beam does not have a defined temporal structure apart from the ramp-up and ramp-down phase. The parameters that can be controlled are the tube voltage and the tube current;
- *pulsed mode*: the X-ray beam has a defined temporal structure containing a certain number of pulses per second. The parameters that can be controlled are the number of pulses per second and the width of each pulse as well as the tube voltage and tube current.

The different settings of the X-ray tube in addition to the part of the patient's body to be examined and the physic characteristic of the patient itself generate a different shape of the diffused radiation spectrum. A measurement of the diffused radiation spectrum has been performed in San Giovanni Battista [37] hospital in Foligno, Italy by using a Poly Methyl Methacrylate (PMMA) phantom of size $20 \times 20 \times 30 \times \text{cm}^3$ that simulates the patient's body relative to the diffusion of X-ray radiation with the tube voltage varied in the range between 60 kV and 110 kV.

The diffused X-ray radiation spectra are measured by using an Amptek X-123 precision spectrometer [43] placed at 20 cm of distance from the PMMA (Figure I-8).

TABLE I-4
ANGIOGRAPH X-RAY TUBE PARAMETERS FOR TYPICAL IRAD PROCEDURES AT THE SAN GIOVANNI BATTISTA HOSPITAL, FOLIGNO (ITALY). [37].

Procedures	**Fluoroscopy (mean values/procedure)**				**Fluorography (mean values/procedure)**		
	Exposure number	Tube Voltage (kV)	Tube Current (mA)	Exposure time (s)	Tube Voltage (kV)	Tube Current (mA)	Procedure Duration (min)
Pace Maker	n.a	n.a.	n.a.	n.a.	80	30	2-5
Percutaneous Transluminal Angioplasty	14	76	400	4	80	30	10-45
Endoscopic Retrograde Cholangio Pancreotography	8	74	160	0.5	80	30	10-30
Percutaneous Transluminal Coronary Angioplastic	10	76	320	6	80	30	15-60

All peaks of the diffused radiation spectra are centered between 30 - 40 keV, with an energy range extending from 10 keV to 100 keV. The characterization and measurement of the spectrum shape define the upper and lower limit of the energy interval where a system designed to detect the X-ray radiation has to work.

Personal dosimetry is currently performed by using passive dosimeters which are certified devices but their results are not available until one month after the procedures have been completed and they don't provide a feedback to the operator during the single medical procedure.

A method to perform real-time calculation and to display the absorbed dose by using active dosimeter can be the best solution to make all possible efforts to reduce radiation dose while maintaining adequate imaging quality for diagnostic and intervention. A dosimeter able to record the real time dose and dose rate is useful because it can be correlated to the different operations performed by the operator during the procedure and can also be used to modify the "modus operandi" of the operator in order to significantly reduce the absorbed dose during the procedure [44]. Moreover it facilitates the storage of the data, improving the radioprotection of the operators for the medical physics [45].

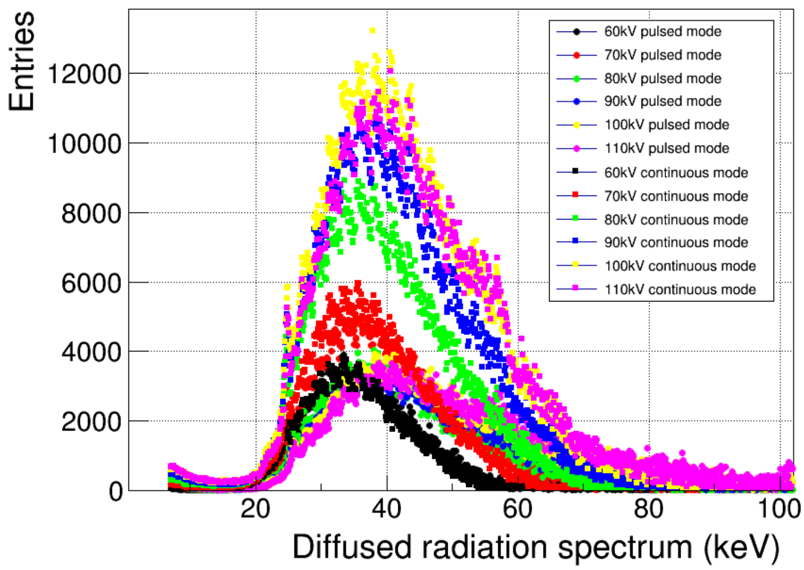

Figure I-8: Diffused radiation spectrum for different IRad medical procedure using the phantom. Different modalities were adopted, continuous and pulsed. The measurements have been performed by using an Amptek X-123 spectrometer.

Chapter II

Dosimetry in Interventional Radiology

In this chapter, the basic description of the quantities and units used to characterize the X-ray radiation exposure during the IRad medical procedures will be illustrated. International Commissions, such as the International Commission on Radiological Protection (ICRP) [46], the International Commission on Radiation Units and Measurements (ICRU) [47] and the European Atomic Energy Agency (EURATOM) [48] are concerned with the effects associated to the exposure to ionizing radiation and with the radiation protection suggesting measures to prevent cancer and other radiation induced diseases. These recommendations include basic concepts and guidelines for radiation protection and the definition of different quantities for quantify the radiation exposure. Then the current state of art of the dosimeters used for individual monitoring will be presented with the focus on current technologies for Active Personal Dosimeters (APDs) that can provide a real-time measurement of personal absorbed dose of operators during IRad procedures. The limitations of these devices will be highlighted and finally the INFN Real Time Active PIxel (RAPID) project will be introduced, focused on the design and production of an active dosimeter with the performances comparable to the passive ones. The RAPID project is a collaboration between of National Institute of Nuclear Physics (INFN of Perugia), the University of Perugia, and the Azienda Unità Sanitaria Locale (AUSL) institutions AUSL Umbria 1 and AUSL Umbria 2

II.1 X-ray radiation: generation and properties

The previous chapter highlighted the advantages of using X-ray radiation in the IRad procedures. There are also other medical application fields such as radiotherapy, computed tomography, fluoroscopy, nuclear medicine where the X-ray radiation is widely used.

The artificial X-ray radiation is typically generated by the X-ray tube, schematically shown in Figure II-1. It consists of a cathode and an anode, facing one another, hermetically sealed in an envelope which provides vacuum, support and electrical insulation [49]. The anode (positive electrode) consists of a large piece of metal, at the end of which a target area is placed, from where the X-rays are emitted. The target area, dubbed focal spot, typically consists of tungsten material. The cathode (negative electrode) consists of a filament (wire coil) that emits electrons when heated, a phenomenon called thermionic emission.

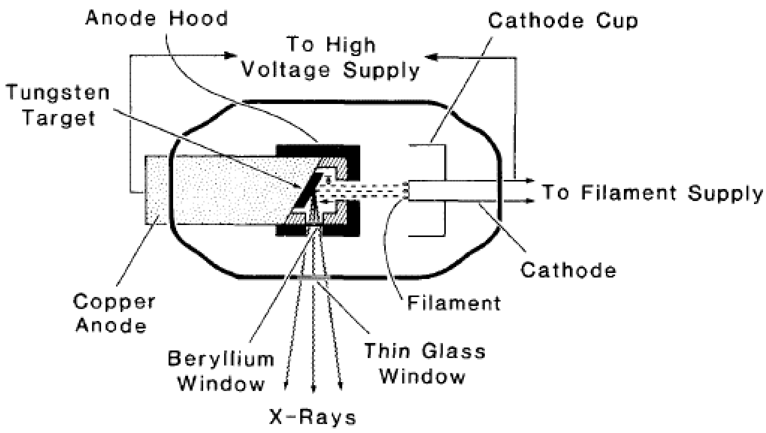

Figure II-1: Schematic diagram of X-ray tube and circuit.

Two different parts can be identified in the circuit: the low-voltage circuit that provides supply current to the filament to emit electrons, and the high voltage circuit that provides the acceleration voltage to the electrons toward the anode. When the electrons are stopped in the anode, the X-ray radiations are emitted in all directions mainly by means of an effect called Bremsstrahlung. The tube voltage and the current at the filament are the main parameters that control the X-ray intensity.

Figure II-2 shows the typical relationship between the tube voltage and the tube current. The shapes of the curves depend upon many factors, such as the distance between anode and cathode, the configuration of the cathode and the filament temperature, which is in turn determined by the filament current.

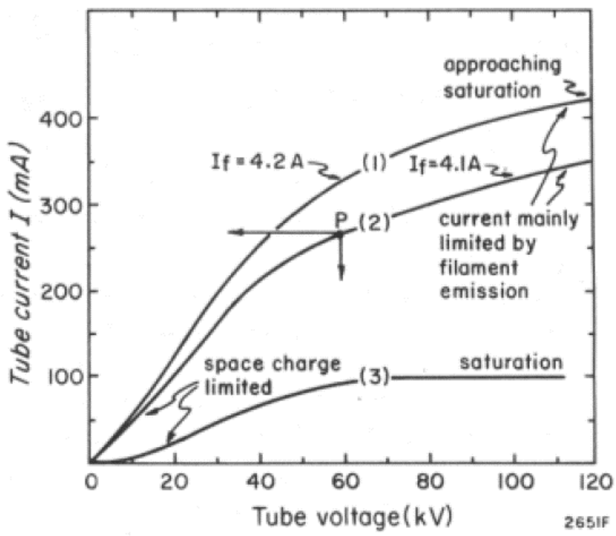

Figure II-2: Tube current as function of tube voltage.

As soon as emitted by the filament, the electrons form a cloud surrounding the filament before being accelerated to the anode. When a voltage of few kilovolts is applied to the tube, the resulting current is small because of space charge effects. As the voltage increases, those electrons get pulled away and the effect is gradually overcome, until the saturation region is reached where all the liberated electrons are pulled to the anode.

Two main types of interactions of the incoming electrons inside the target can be identified, producing respectively two different kinds of X-ray radiation: *i)* interactions with electron shells produce the so called characteristic X-ray photons with well-defined, discrete energies specific to the target material (lines spectrum); *ii)* interactions with atomic nuclei produce the so called Bremsstrahlung or braking X-ray photons, with continuously distributed energies (continuous part of the emission spectrum).

The Bremsstrahlung process is the interaction that produces the most photons in the process. Electrons that penetrate the anode material and pass near a nucleus may be strongly deflected and slowed down by the action of the Coulomb force of attraction from the nucleus and like all strongly accelerating charged particles lose energy as high frequency electromagnetic radiation (Figure II-3).

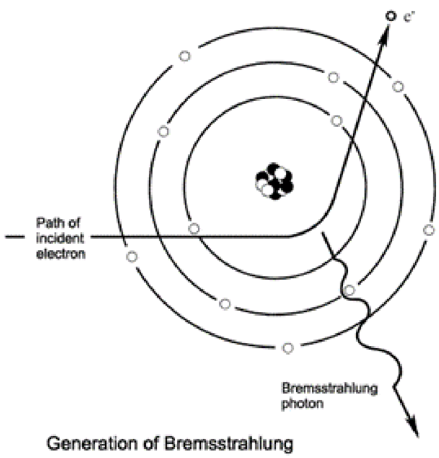

Figure II-3: Illustration of the Bremsstrahlung process.

As a result, a fraction of the electron energy is removed from the electrons for every interaction with nuclei and appears in the form of photons that propagate in free space as electromagnetic radiation with a direction which is a function of the incident energy of the electrons.

The other kind of interaction that generates a characteristic radiation involves a collision between the incoming electrons and the orbital electrons in the atom (Figure II-4).

After the collision, the hit electron is dislodged from the atom and it leaves a vacancy that is filled by an electron from a higher energy level. As the filling electron moves down to occupy the vacancy, it gets rid of its excess energy in the form of an X-ray photon of a well-defined energy, exactly equal to the difference between the energy levels involved in the atomic transition. This phenomenon is called characteristic radiation because the energies of the emitted photon are characteristic of the chemical element that serves as target for the anode material.

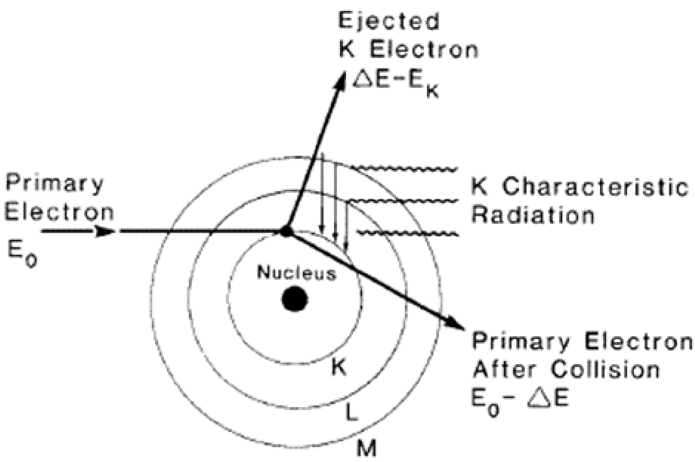

Figure II-4: The generation process of the characteristic radiation.

The typical energy spectral distribution of the photons generated by a diagnostic X-ray tube at different tube voltages is represented in Figure II-5.

The relative number of photons as a function of the photon energy is shown in Figure II-5 (a), and the area under the curves is proportional to the total number of photons emitted. The relative energy is drawn in Figure II-5 (b) and is obtained from the first chart by multiplying each ordinate by the energy of the photon at that ordinate and the area under the curves is proportional to the energy carried by the beam.

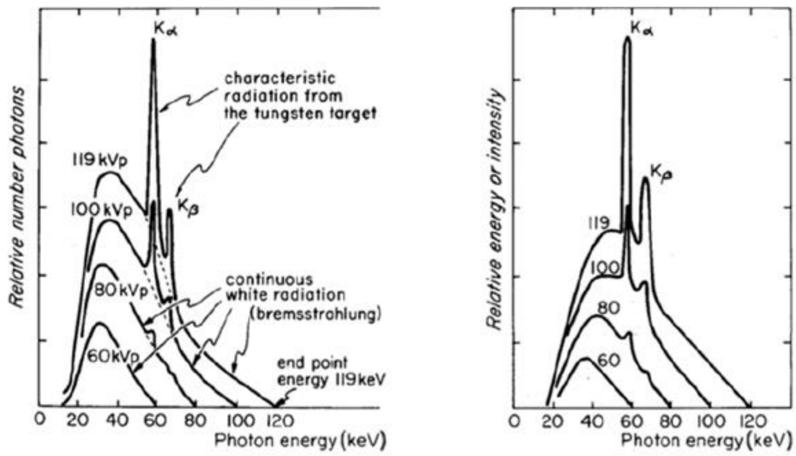

Figure II-5: Observed spectra from a diagnostic X-ray tube excited at 60, 80, 100 and 119 kVp. (a) Relative number of photons vs photon energy; (b) relative energy of photons vs photon energy [50].

Therefore, the energy spectrum of the X-ray radiation shows a continuous distribution of energy for the Bremsstrahlung photons superimposed to characteristic radiation lines of discrete energy. Of course the upper energy limit of the spectrum is equal to the energy of the incident electrons due to the applied kilovolt voltage peak (kV_p), and is reached when the electron losses all its energy in the first collision. Hence to avoid the anode spectrum lines it is enough to lower the kV_p value under the K_α characteristic radiation energy of tungsten.

II.1.1 X-ray dosimetry

A radiation beam involves two distinct aspects: the description of the photons beam in terms of the number and energies of all photons of the beam (flux and photon beam spectrum), and the description of the amount of energy per unit mass (absorbed dose) that the photon beam may deposit in a given medium.

In order to define these quantities, we first assume that the beam is mono-energetic. Fluence is defined as the number of photons dN crossing an imaginary sphere of cross-sectional maximum area dA.

$$\Phi = \frac{dN}{dA} \tag{II.1}$$

The amount of energy dE carried by the photons, called energy fluence, is defined in the following way:

$$\Psi = \frac{dE}{dA} = \frac{dN \cdot h\nu}{dA} \tag{II.2}$$

where $h\nu$ is the energy associated to each photon.

It is also possible to define the fluence rate and the energy fluence rate, respectively, considering the time dt :

$$\phi = \frac{d\Phi}{dt} \tag{II.3}$$

$$\psi = \frac{d\Psi}{dt}$$

In real conditions, however, the X-ray beam is almost never monochromatic and the quantities described above cannot be used in practice. Indeed corresponding spectral density quantities are defined, but they are again difficult to measure. Then a more useful way to quantify photons beams is by evaluating the energy transfer to a medium when interacting with it. This shifts the focus on the effects of the interaction of radiation with matter.

The ICRU has introduced a quantity called kerma (Kinetic Energy Released per unit Mass) [51] to express, at a point of the radiation field, the result of the first step of the interaction process that leads to the energy absorption by the medium; kerma in fact gives the concentration per unit mass of material of the energy transferred by the primary particles (photons) to the secondary ones (electrons), which are the true responsible of the final imparted energy to the medium.

Kerma is a measure of the amount of initial kinetic energy dE_{tr} of all the charged ionizing particles, actually transferred from a photons (X-rays in our case) in a unit mass dm.

$$K = \frac{dE_{tr}}{dm} \tag{II.4}$$

In most of the cases when the so-called *charged particles equilibrium* exists and the radiative losses are negligible, Kerma is the quantity that directly connects the description of the radiation beam with its effects. In these instances, it coincides with the absorbed dose and it is measured in J/kg, named Gray (Gy) for the SI unit.

For a photon beam crossing a medium, kerma is directly proportional to the particles fluence and is given by:

$$K = \Phi \cdot \left(\frac{\mu}{\rho}\right) \cdot \overline{E_{tr}} \quad \text{(II.5)}$$

where μ is the attenuation coefficient, ρ is the mass density, $\left(\frac{\mu}{\rho}\right)$ is the mass energy attenuation coefficient for the medium and $\overline{E_{tr}}$ is the average amount of energy transferred to electrons of the medium at each interaction.
Finally, if the photon beam is not mono-energetic, in order to obtain the final value, the kerma is integrated over all photons energies contained in the spectrum.

$$K = \int_0^{h\nu_{\max}} \frac{d\Phi(h\nu)}{dh\nu} \cdot \left(\frac{\mu(h\nu)}{\rho}\right) \cdot E_{tr}(h\nu) d(h\nu) \quad \text{(II.6)}$$

In the calculation of the kerma, the sum of the initial kinetic energy of all charged particles produced by the incoming photons in a certain volume element of mass dm has been considered. Due to Bremsstrahlung process not all the energy transferred to the electrons is retained in the medium within a specific volume element, even if this effect is relatively small in biological matter and becomes important only for high energies and high atomic number material. In radiotherapy and radiobiology only the portion of energy that is actually retained in the medium at point of interest is needed to be considered. For this purpose, ICRU has defined another quantity called absorbed dose, which is the most fundamental one in dosimetry and is introduced in the following way [51]:

$$D = \frac{dE_{ab}}{dm} \quad \text{(II.7)}$$

where dE_{ab} is the mean energy deposited by the ionizing radiation to the matter in a small volume of infinitesimal mass dm. The SI unit for the absorbed dose is the same as that for the kerma, i.e. the gray (Gy) defined as:

$$1\,Gy = 1\,{}^{J}\!/\!{}_{kg} \tag{II.8}$$

The quantity absorbed dose has been defined in such a way that it is valid to describe the quantity of energy deposited in any material by all types of radiations (directly or indirectly ionizing particles), of any energy. While it is possible to relate kerma to fluence in a quite simple manner, the absorbed dose cannot be related to kerma in an equally simple way, unless a particular state of equilibrium exists in the medium between the secondary charged particles that enter and leave an elementary volume.

Then in order to correlate the two quantities we have to describe the so-called *charged particle equilibrium*. Such an equilibrium exists when the number, the energy and the direction of the charged particles remain constant inside the material volume of interest. To understand the consequences of the onset of this equilibrium in a medium irradiated by a photon beam, regarding the relationship between dose and kerma, let us consider a free beam of high energy photons hitting a medium. We can identify two different regions in the medium, in both cases of negligible attenuation of the primary beam (ideal) (Figure II-6 (a)) or partial attenuation of the primary beam (real) (Figure II-6 (b)): the initial build-up region where the absorbed dose increases until it reaches its maximum at depth *R* and a region of electronic equilibrium. In the build-up region the generated electrons set in motion by the incident photons are ejected from the surface and the subsequent layers. The most part of these electrons deposits their energy a significant distance away from their site of origin and hence the absorbed dose increases with depth until a maximum is reached. On the contrary, since kerma represents the energy transferred from photons to directly ionizing electrons it is maximum at the entrance surface.

If it is assumed that there is no attenuation of photons (Figure II-6 (a)), the same number of electron tracks is set in motion in each square from A to G and kerma is uniform toward the inside. Regarding the absorbed dose, after the initial build-up region it is also constant with depth. Thus beyond the buildup region where kerma and absorbed dose are both constant with depth, there is *charged particle equilibrium* and the two quantities assume the same value.

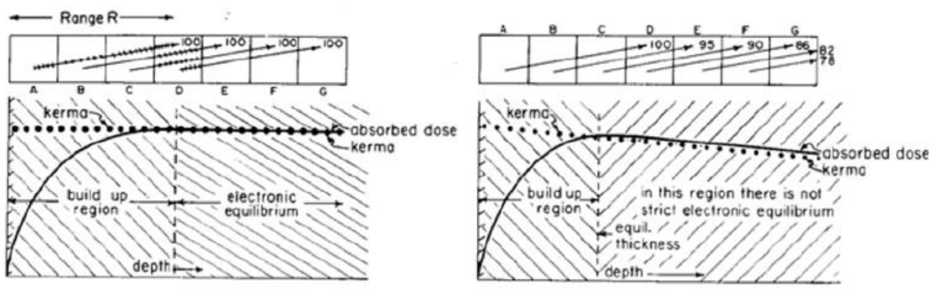

Figure II-6: Relationship between kerma and absorbed dose (a) without attenuation and (b) with attenuation of the photon beam [49].

In real condition (Figure II-6 (b)), when attenuation of the primary beam is taken into account, after the build-up region, the absorbed dose decreases as kerma continues to decrease, but the absorbed dose curve is always above the kerma curve. This means that true electronic equilibrium is never established except that at the point where kerma and dose curves intersect. Yet there is a wide region where kerma and absorbed dose remain strictly proportional to each other in a condition of quasi-equilibrium. In these regions the equilibrium condition relations may still be applied but introducing some corrective factors. At last, in the special simplified case of electronic equilibrium, if radiative losses by charged secondaries must be considered, instead of putting the simple equality $D = K$ it is possible to relate absorbed dose with kerma with the following equation

$$K = \Phi \cdot \left(\frac{\mu}{\rho}\right) \cdot \overline{E_{ab}} = K \cdot (1 - g) \qquad \text{(II.9)}$$

where $\overline{E_{ab}}$ is the part of the average kinetic energy transferred to electrons that contribute to ionization, g is the fraction of the energy that is lost by Bremsstrahlung from charged secondaries and K is the kerma.

II.2 Radiation protection quantities and radiological risk

Kerma and the absorbed dose are not appropriate to interpret and fully quantify the effects caused by the energy transfer from radiation to living matter. Then the ICRP has developed a series of quantities for the so-called *radiation protection* which is a branch of science engaged in the protection of men and environment from the possible damages depending on the use of ionizing radiations in human activities. These quantities may be classified in two main categories: *i) primary limiting dose quantities* (protection quantities) taking into account the human body properties; *ii) operational dose quantities* for practical monitoring of external exposure [52].

The *primary limiting dose quantities* are related to the risk of harmful effects for the human body resulting from the exposure to ionizing radiation sources, taking into account the different radiation sensitivities of various organs and tissues and the different kinds of radiation. The aim is to prevent such effects or to keep the risks within reasonably acceptable limits [53]. Unfortunately these quantities are not easily measurable and then the *operational dose quantities* are used for monitoring external exposure. In fact they are an estimate of an upper limit for the value of the limiting quantities relative to an exposed or potentially exposed person and are often used in place of those quantities in practical regulations. The two most important *operational dose quantities* are: the deep personal dose equivalent and the superficial personal dose equivalent.

The European Council Directives are issued on the basis of documents prepared by the EURATOM, which in turn shares most of the ICRP recommendations; these Council Directives are the normative reference in Europe for radiation protection and set radiation exposure limits [54]. The total effective dose which an individual is exposed to consists of two contributions, originating respectively from: *i) natural background radiation* constituted by cosmic rays, external gamma rays emitted by radioactive materials contained in the earth's crust and internal irradiation from radioactive element ingested into the human body (this accounts for about 2.4 mSv in average per year [55]); *ii) man-made radiation* that includes various sources, mainly diagnostic and therapeutic X and γ-rays employed in medicine, with little additions from radiations used for industrial purposes, deriving from nuclear power plants or nuclear weapons tests in high atmosphere and of course also from occupational exposure.

Concerning this latter exposition for workers exposed to radiological risk, the limits imposed by the Italian law, both for the effective dose and for the equivalent doses to particular organs or tissues, are defined in TABLE II-1. The corresponding limits are divided in two categories, called *exposed* or *unexposed* workers, recognized by the Italian law. The workers that receive in a calendar year a dose greater than the values set out on the Italian decree are classified in category A; the other ones are classified in category B.

TABLE II-1
EFFECTIVE DOSE LIMITS AND EQUIVALENT DOSE LIMITS FOR CERTAIN ORGANS AND TISSUES, PER YEAR, ACCORDING TO THE ITALIAN LAW [56].

Exposed external body part	**Effective dose limit (mSv/year) and equivalent dose limit for certain organs and tissues**		
	Exposed workers		**Non-exposed workers**
	Category A	**Category B**	
Total body	20	6	1
Eye lens	150	50	15
Skin	500	150	50
Extremities	500	150	50

Monitoring the individual radiation exposure is mandatory and several publications prove the relevance of this issue [57] [58] [59]. An efficient planning of the procedures is necessary, in order to keep the received dose as low as possible (in accordance with one of the cardinal principles of radiation protection) and in any case below the normative limits [60].

II.2.1 Protection quantities

As mentioned above all of the quantities that have been introduced and described, are physical quantities that can be measured. However, for determining the amount of radiation delivered to a body and the relationship to the biological effects or to the biological impact of the radiation exposure, the absorbed dose does not fulfill this task completely and rigorously. Firstly different types of radiation might not produce the same biological impact, even when the absorbed dose or energy delivered to the tissue is the same. Then, the quantity named *equivalent dose* has been introduced to express the relative biological impact of different kinds of radiations on a certain organ or tissue and regarding a specific effect; it is defined as:

$$H_T = \sum_R \omega_R D_{T,R} \tag{II.10}$$

where D_T is the mean absorbed dose in the organ or tissue T from radiation of type R incident on the human body and ω_R are radiation weighting factors characterizing the biological effectiveness of the specific radiation R with respect to reference photons. The sum is taken over all types of radiation involved. While absorbed dose D is measured in grays, ICRP recommends the use of a unit called sievert (Sv) for equivalent dose, even if they have the same dimensions:

$$1\,Sv = 1\,{}^{J}\!/\!_{kg} \tag{II.11}$$

ICRP uses radiation weighting factors ω_R to connect absorbed dose to the protection quantity dose equivalent. The values of the radiation weighting factors ω_R are summarized in TABLE II-2.

The different parts of the body and organs are not equally sensitive to the stochastic adverse effects of radiation (essentially cancer), then ICRP has defined another quantity called effective dose that takes into account the specific organs and areas of the body that are exposed and their diverse capability to develop a tumor. The definition is:

$$E = \sum_T H_T \omega_T \quad \text{with} \quad \sum_T \omega_T = 1 \tag{II.12}$$

where the different areas and organs have been assigned tissue weighting factor ω_T values.

TABLE II-2

RADIATION WEIGHTING FACTORS ω_R FOR DIFFERENT TYPES OF RADIATION [61].

Radiation	Radiation weighting factors ω_R
Photons, electrons and muons of all energies	1
Neutrons	See Figure II-7
Protons >2 MeV (except recoil protons)	2
Alpha particles and heavy ions	20

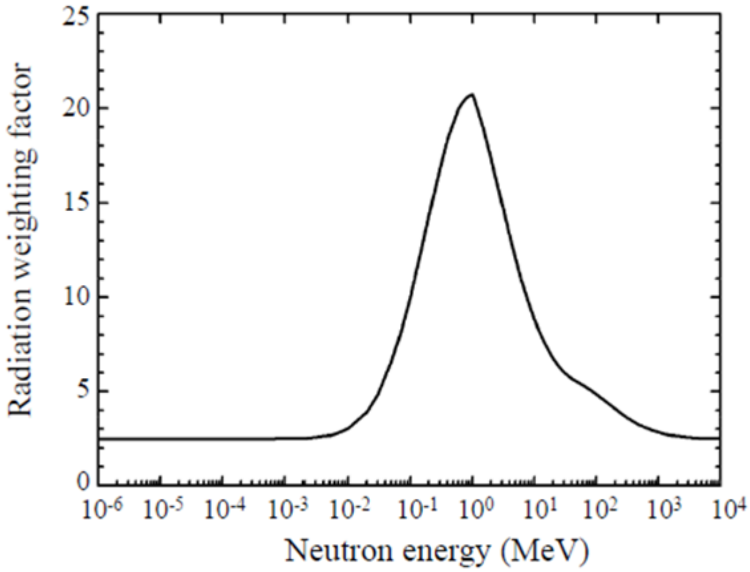

Figure II-7: Radiation weighting factor ω_R as a function of neutron energy [61].

If more than one area has been exposed, then the total body effective dose is just the sum of the effective doses for each exposed area, as indicated in the above formula. The values of the tissue weighting factors ω_T are summarized in TABLE II-3.

The tissue weighting factors are calculated for reference male and female using a family of reference phantoms. Then effective dose is not based on data from any one individual person and does not provide an individual specific dose assessment but rather that for a reference person under a given exposure situation. Effective dose is therefore suitable for risk assessments for individuals especially in the prospective dose assessment for planning and optimization in radiological protection. It is also a practical value for comparing potential stochastic effects from different diagnostic examinations. On the contrary effective dose is neither recommended for epidemiological evaluations, nor should it be used for detailed specific retrospective investigations of individual exposure and risk.

TABLE II-3

TISSUE WEIGHTING FACTORS ω_T FOR DIFFERENT ORGANS AND TISSUES [61]. *MEAN FOR DRENALS, EXTRATHORACIC AIRWAYS, GALLBLADDER, HEART, KIDNEYS, LYMPH NODES, SKELETAL MUSCLE, ORAL MUCOSA, PANCREAS, SPLEEN, THYMUS, PROSTATE/UTERUS–CERVIX.

Organ/tissue	**Tissue weighting factors ω_T**
Bone marrow, colon, lung, stomach, breast, remainder*	0.12
Gonads	0.08
Bladder, liver, oesophagus, thyroid	0.04
Bone surface, skin, brain, salivary glands	0.01

II.2.2 Operational quantities

The human body-related protection quantities, equivalent dose in an organ/tissue and effective dose, are easily measurable. For this reason ICRU has introduced and defined a set of operational quantities, which can be measured and which are intended to provide a reasonable estimate for the protection quantities. These

quantities aim to provide a conservative estimate for the value of the protection quantities avoiding both underestimation and too much overestimation.
They are based on the so called dose equivalent H at a specific point in a tissue or tissue-equivalent material, defined as:

$$H = Q \cdot D \tag{II.13}$$

where D is the absorbed dose at the point of interest and Q is, at the same point, a quality factor weighting the relative biological effectiveness of the different types of ionizing radiation. Q is defined as a function of the linear energy transfer in water for a charged particle.
The personal dose equivalent $H_P(d)$ is the operational quantity for individual monitoring and is the dose equivalent in ICRU soft tissue (a material equivalent to the body) at an appropriate depth d. The depth d is expressed in millimeters and used to select superficial or deep organ doses. ICRU recommendations are: for superficial organs (skin) depths of 0.07 mm, and for lens of the eye depths of 3 mm. The personal dose equivalents for those depths are denoted by $H_P(0.07)$ and $H_P(3)$, respectively. A depth of 10 mm is used, $H_P(10)$, for deep organs and to control the effective dose.

II.3 Dosimeters

The dosimeter is a device currently used in the medical field to estimate the value of radiation dose absorbed by operators in facilities where workers are exposed to ionizing radiation. Two different types of dosimeter are available: passive dosimeters and active dosimeters. Passive dosimeters are used to evaluate the so-called *primary dosimetry* of the health care workers and usually consisted of radio

Thermoluminescent (TL) materials, able to record and accumulate the amount of radiation absorbed. Active dosimeters have been used for the so-called *secondary dosimetry* that is to perform a real time monitoring of the radiation exposure. The main characteristic of the active dosimeter is the ability to supply incremental real time readings to the operator integrated into video monitoring control systems. For this characteristic they have become a key part of some radiation protection programs with educational purposes. They aimed to minimize the dose received by operators in interventional radiology procedures, in accordance to the optimization principle of radiation protection.

II.3.1 Passive dosimeters

Despite the rapid development of active real-time electronic dosimeters, passive dosimeters still remain the certified devices for individual dose measuring.

Certified devices for individual dose measuring are passive dosimeters, such as film badge dosimeters and Thermoluminescent dosimeters (TLDs). Film badge dosimeters (no longer used) consist of a holder containing a photographic film. The silver film emulsion is sensitive to radiation and the exposed areas blacken in response to incident radiation after development, corresponding to an increase of optical density; a densitometer is used for measuring such a density in the film.

On the other hand, luminescence dosimeters are now currently used for the dosimetry of the operators. The principle of luminescence materials for the dosimetry of ionizing radiation relies on the relationship between the absorbed dose and the intensity of light emission under a stimulus. In particular, according to this principle, certain crystalline materials (e.g. lithium fluoride (LiF), calcium fluoride (CaF_2), beryllium oxide (BeO)), when heated, emit light proportionally to the amount of radiation previously absorbed by them [62].

The common luminescence detectors applied in personal dosimetry are just the thermoluminescent detectors. The TLDs are made of materials that exhibit high concentration of “trapping centers”, coincident with impurities or lattice defects in the crystals, within the band gap placed between the valence and the conduction bands. When the incident radiation hits the material, in the radiation-matter interaction, the valence electrons are temporarily raised to the conduction band and when they try to return in the fundamental state they may be captured at various trapping centers. If the distance between the energy level of trapping centers and the bottom of conduction band is large enough there is a small probability that the trapped electrons are promoted into the conduction band by thermal excitation. So the exposure to a source of ionizing radiation lead to a progressive increase of the number of trapped electrons.

After the exposure, the TLD sample is read out by increasing the temperature in a controlled manner that is according to a specified raising profile. The heat supplied by the increasing temperature, based on the value of the trap energy level, leads the released electron to go back to the conduction band with the subsequent emission of a photon when it goes down to the valence band. Ideally the total number of photons can be used as an indicator of the number of electron-hole pairs created by the incident radiation. The light yield is recorded as a function of sample temperature in a glow curve of the type of Figure II-8.

The basic signal related to the radiation exposure is the total number of emitted photons associated with a certain peak; this is in turn proportional to the area under the selected glow curve peak. The major advantages of thermoluminescence dosimeters are:

- high sensitivity to low doses such as 1 mGy or even much lower;
- linear response with dose up to at least 1 Gy;
- small size and ease of manipulation;

- atomic number often near to that of biological tissues;
- response independent of dose rate.

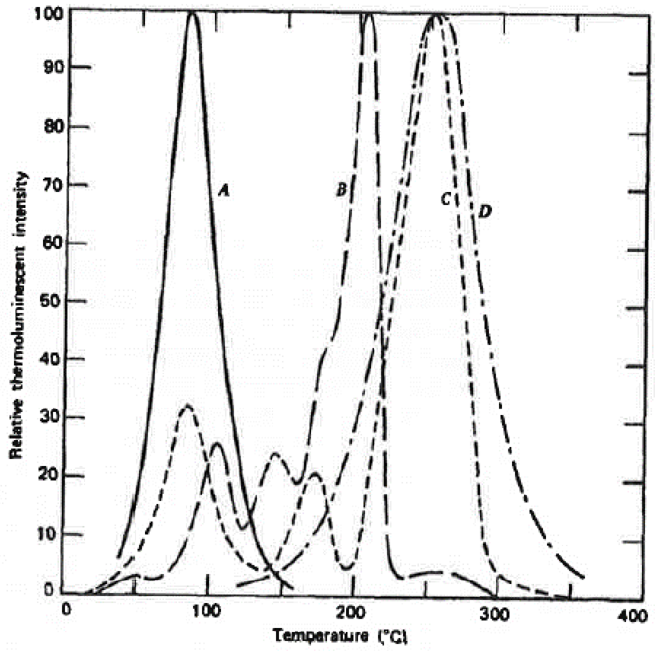

Figure II-8: Typical thermoluminescent "glow curves" normalized to the same maximum intensity. Materials are: A- $CaSO_4$: Mn; B – LiF: Mg, Ti; C- CaF_2 and D- CaF_2 : Mn. Details of these curves depend on various factors: pre-irradiation annealing procedures, radiation exposure level and heating rate during readout [62].

Some of the requirements for personal dosimeters used for determining the value of $H_P(10)$ (IEC 62387-1, 2007) are listed in TABLE II-4.

A drawback is instead that TLDs are used for determining the total dose of ionizing radiation accumulated over a certain time interval, typically one to three months and do not provide a real time measurement: in this way, operators cannot be aware of an over-exposure during the procedures. Moreover, because the dose measurement is integrated over the procedures, TLDs are unable to provide specific information for each of them and cannot therefore be used for a real time optimization of the single exposure.

TABLE II-4
SELECTED REQUIREMENTS OF PERSONAL DOSIMETERS BASED ON TLDS USED FOR MEASUREMENTS OF $H_P(10)$ AND $H_P(0.07)$.

Characteristics under test	**Minimal measuring range**	**Performance requirement**
Relative response due to the non-linearity	0.1 mSv < $H_P(10)$ <1 Sv	-9% to +11%
Relative response due to mean photon energy and angular response (for $H_P(10)$)	80 keV to 1.25 MeV and angles from 0° to ±60°	-29% to +67%
Relative response due to mean beta radiation energy (for $H_P(10)$)	0.8 MeV	Indicated value maximum 10% of $H_P(0.07)$
Relative response due to mean beta energy (for $H_P(0.07)$)	0.2 MeV to 0.8 MeV and angles from 0° to ±60°	-29% to +67%

II.3.2 Active dosimeters

Passive dosimeters in the IRad procedures are used for their high sensitivity in the energy range between 10 keV and 3 MeV and their good accuracy of 10% but there are also some disadvantages in using them, the main of which is that the dose readout is done at fixed time intervals, i.e. once a month, without a sufficient time resolution on the different exposures of the operators during the single procedure so it is difficult to estimate the absorbed doses in each phase of the intervention [62]. To find criteria for workers to optimize the radiation protection and decrease the unnecessary exposure, several studies have shown a possible solution by using Active Personal Dosimeters [63].

The main feature of an APD is the possibility to assess the equivalent dose and the equivalent dose rate in real time, and a visual or acoustic alarm can be set when a certain value of dose is exceeded. Moreover the active dosimeters are an efficient instrument to obtain the information on occupational dose rate and the correlation between the dose and the relative position of the operator and radiographic factors during different phases of the medical procedures.

Figure II-9: Examples of commercial semiconductor APDs: MGPi DMC2000XB [64]; Thermo Scientific EPD-Mk2+ [65]; Dosilab EDM-III [66]; Unfors EDD-30 [67]; Atomtex AT3509C [68]; Philips DoseAware [69]; RaySafe (same package of Philips DoseAware) [70].

There are several types of APDs. The Direct Ion Storage (DIS) dosimeters are based on the coupling of a gas-filled ion chamber with a semiconductor non-volatile memory cell in Metal-Oxide-Semiconductor Field-Effect Transistor (MOSFET) technology. The device performance can be optimized by choosing the most appropriate material for the chamber walls and the fill gas. The solid state semiconductor dosimeter is another type of APDs. The ionizing radiation interacting within the depletion region of the semiconductor p-n junction produces electron-hole pairs that are separated and collected by applying an external voltage to the terminals of the two electrodes. This effect produces an electric pulse which is subsequently processed by dedicated electronics [71].

In the framework of The European Commission ORAMED FP7 project a set of commercial APDs have been tested in different conditions in order to evaluate their performances. Tests both in laboratory [72] and in clinical environment [73] using continuous and pulsed X-ray fields have been performed. The following semiconductor APDs were chosen for testing: DMC2000XB by MGPi, EPD Mk2.3 by Thermo, EDM III by Dosilab, EDD 30 by Unfors, AT3509C by Atomtex and DoseAware by Philips.

All these APDs are optimized in portability, their connectivity is based on a wireless interface, except for the EDD 30 and they feature an alarm, acoustic or visual, that will be activated if the level of absorbed dose exceeds the preset limit. The APDs were tested with continuous and pulsed X-ray field to determine the response in terms of personal dose, energy, personal dose equivalent rate and angle.

TABLE II-5 summarizes the comparison between the different APDs. The results of this ORAMED project have shown a limit of the current technology of APDs due to the specificity of the X-ray radiation used in IRad procedures, which often features low energies. It can also be noticed that most commercial APDs feature an energy range with a lower bound greater than that of passive dosimeters (i.e., 10 keV), which are the certified devices for radiation protection [74].

The performances of the APDs are good by considering continuous beams, as a matter of fact the personal equivalent dose response is linear up to 500 mSv and the energy response of tested APDs is within the interval required in the IEC 61526 standard [75] from 1.25 MeV (S-Co energy) down to 24 keV (N-30 radiation quality) for all APDs except EDD30 and DoseAware. The response of these dosimeters instead worsens when the personal equivalent dose rate increases and by considering a pulsed X-ray beam regime.

For most APDs, the response decreases when the personal dose equivalent rate increases. For personal dose equivalent rates lower than 0. 2 Sv/h, the deviation with reference is within 20% and fall down more or less rapidly for higher dose rates.

TABLE II-5
COMPARATIVE TABLE OF THE SPECIFICATION OF THE COMMERCIAL APDS.

Device name	**Energy range**	**Dose rate range**	**Personal Dose range ($H_p(10)$)**	**Dimensions**	**PSN**
MGPi DMC2000XB [64];	20 keV-6 MeV	1 µSv-10 Sv	0.1 µSv/h-10 Sv/h	87 × 48 × 28 mm^3	no
Thermoscientific EPD Mk2+ [65]	15 - 10000 keV (±20%)	0 µSv/h – 4 Sv/h	0 Sv - 16 Sv	85 × 63 × 19 mm^3	no
Dosilab EDM III [66]	20 - 6000 keV	0.5 µSv/h – 1 Sv/h	1 µSv - 1 Sv	n.a.	no
Unfors EDD-30 [67]	14 - 120 keV (±10%)	0.03 mSv/h – 24 Sv/h	10 nSv - 9999 Sv	6 × 11 × 22 mm^3	no
Atomtex AT3509C [68]	15 -10000 keV	0.1 µSv/h 5 Sv/h	1 µSv – 10 Sv	105 × 58 × 23 mm^3	no
Philips DoseAware [69]	48 - 118 keV (±30%)	40 µSv/h – 300 mSv/h	1 µSv - 10 Sv	45 × 45 × 10 mm^3	yes
RaySafe i2 [70]	33 – 101 keV	40 µSv/h – 300 mSv/h	1 µSv – 10 Sv	45 × 45 × 10 mm^3	yes

The limitations in the current technology of the APDs have promoted the establishment of a research project called Real time Active PIxel Dosimetry (RAPID), a collaboration between the Perugia unit of the National Institute of Nuclear Physics (INFN), the University of Perugia, and the Azienda Unità Sanitaria Locale (AUSL) institutions AUSL Umbria 1 and AUSL Umbria 2.

The goal is to design an APD based on the innovative approach of using a commercial CMOS image sensor as sensing device [76][77] that provides:

- a better awareness of ionizing radiation exposure, very useful for the optimization of technical procedures with the aim of dose reduction, not only for operators, but also for patients, by modifying their modus operandi; the operator can manage his own position with respect to the patient, and therefore with respect to the radiation beam, resulting in a significant decrease of the delivered dose;
- the information about the absorbed dose during each acquisition, that could help to reach the optimization of the exposure time, and therefore to reduce the dose to operators, population and patient;
- the implementation of surveillance procedures by the radioprotection expert, with immediate intervention in case of very high doses conditions;
- the data recording in a remote archive, collecting offline the dose of operators, thus feeding data for a detailed study of the exposure levels for each procedure and helping the planning of the number and type of procedures that interventionists can undertake in a given period.

Chapter III

The CMOS image sensor as X-ray detector

This chapter is focused on the description of the silicon radiation sensors by considering the Monolithic Active Pixel Sensor (MAPS) and the interaction of the photons with the matter. The MT9V011 CMOS image sensor of the Aptina family has been studied as the sensitive element for the X-ray radiation. The photons counting algorithm has been described and the procedure to extract two dosimetric observables linearly correlated with the absorbed dose and dose-rate has been reported. Finally the calibration of the sensor in a certified center has been described.

III.1 Silicon radiation sensor

A radiation detector consists of an absorbing material in which a fraction of incident radiation is converted into a detectable signal, usually in the electric domain. Different interactions between radiation and material take place depending on the type and energy of particles involved [78]. Charged particles (e.g. protons, electrons) interact with the electrons in the absorbed medium through the Coulomb force. On the contrary, the interaction of uncharged particles (e.g. photons), results in the full or partial energy transfer from the incident radiation to the electrons or the atomic nuclei. In a semiconductor radiation detector, the incident radiation interacts with detector material, such as Silicon (Si) or Germanium (Ge), and the overall significant effect is the creation of electron-hole pairs in a small volume of the sensitive material. The ionization process pushes electrons to the conduction band while leaving in the valence band an equal number of holes. The generation of electron-hole pairs can be described by the approximated relation:

$$n = \frac{E}{E_{e-h-av}} \tag{III.1}$$

where *n* is the number of generated electron-hole pairs, *E* is the energy released by the particle and E_{e-h-av} is the average energy for the creation of an electron-hole pair (different from the band-gap energy of the semiconductor).

The main advantage of semiconductor detectors with respect to the gaseous ones lies in the different electronic level structure of the ionization energy: the value of E_{e-h-av} for silicon is 3.6 eV compared with about 30 eV required in typical gas-filled detectors [62]. Therefore the quantity of ionization produced by an event and the number of charge carriers is approximately 10 times greater for a given energy deposited in a semiconductor detector with respect to the gaseous ones.

The main benefits concern the achievable energy resolution: *i)* lower statistical fluctuation in the number of carriers per pulse and *ii)* better signal-to-noise ratio (S/N) at low energies, where the resolution may be limited by electronic noise.

III.1.1 The Monolithic Active Pixel Sensor

In monolithic sensors, both electronics and sensor are integrated in the same substrate. Mostly used for detection of visible photons, they feature an inverse biased photodiode as sensing element and are produced in a CMOS technology [79][80][81]. The electron-hole pairs generated by the incoming radiation move in the electric field induced by the inverse voltage and give rise to a “leakage” photo-current through the photodiode, which can be measured as a voltage drop at the ends of the junction.

In order to collect the maximum amount of generated charge, a typical approach is to use a doped p^+ substrate with an epitaxial p^- layer containing the n-well designed to collect the electrons that are diffusing in the material after their generation [82]. The thickness of the epitaxial layer determines the maximum energy of detectable photons due primarily to their interaction probability (absorption length).

The photo-current discharges the photodiode that is periodically recharged by applying the inverse biasing for a given time interval (reset time) while for the rest of the time is left floating (Figure III-1). The voltage drop when the junction is left floating depends on *i)* the leakage current of the photodiode and *ii)* the integral of the current generated by the radiation during this time. This time interval is called integration time.

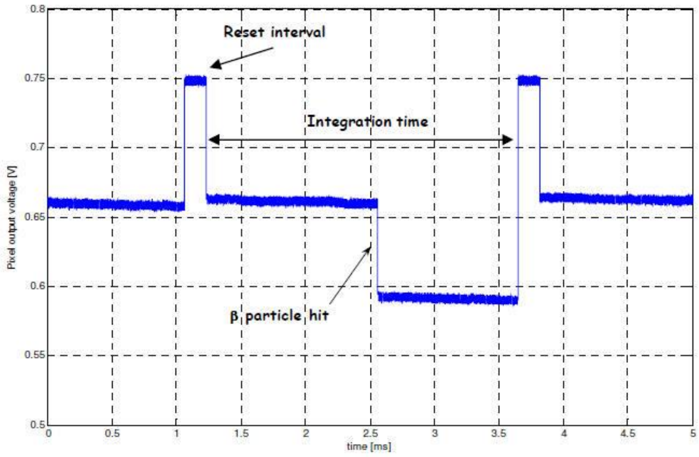

Figure III-1: A typical output voltage of an APS crossed by a beta particle. The charge generated by the particle causes a clear voltage drop in a small time interval (few ns).

Currently most monolithic CMOS sensors have an Active Pixel Sensor (APS) structure. In APS, the photodiode is typically integrated in a pixel together with three transistors: a reset switch M_{rst}, an input M_{sf} and a selection switch M_{sel} (Figure III-2 (a)).

The described pixel structure is replicated and arranged in a matrix to obtain the sensor (Figure III-2 (b)). The readout of each pixel is performed row by row by turning on all the M_{sel} transistors of the same row and imposing a current on each column line. At the end of each column the voltage of the corresponding pixel of the selected row can be read by peripheral electronic and digitally converted.

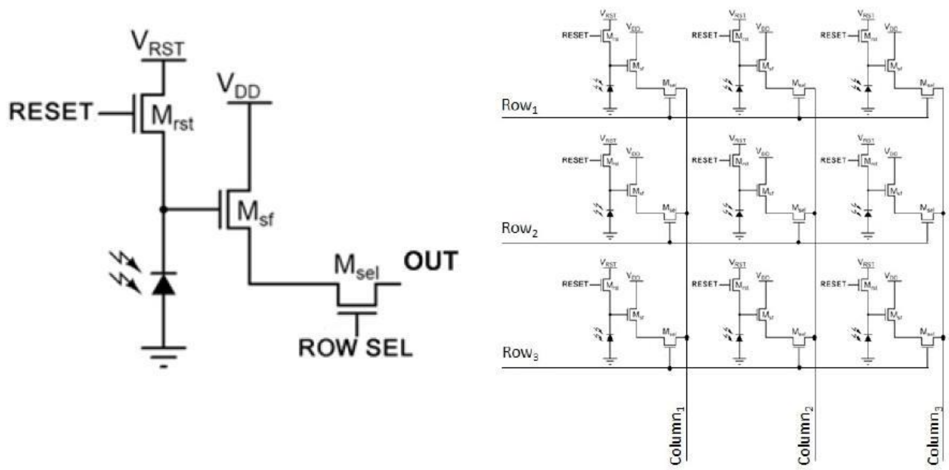

(a) (b)

Figure III-2: (a) Electrical scheme of a standard three transistor APS, and (b) a simple 3x3 pixels matrix.

CMOS sensors are optimized for visible light applications (e.g. imaging) but are also interesting for other applications, mainly due to the following characteristics [80]:

- low cost, because they are fabricated in a standard Very Large Scale Integration (VLSI) technology;
- low power, because the circuitry in each pixel is active only during readout;
- increased functionalities, thanks to the benefits provided by the CMOS technology: the control logic can be integrated in the same substrate as the sensor array.

These sensors can be used for the detection of electromagnetic radiation from the infrared up to the X-ray range: this qualifies them for a wide range of imaging applications, from commercial photo cameras up to biomedical applications [82].

In recent years CMOS sensors have also been proposed for the detection of single ionizing particles, such as Minimum Ionizing Particles (MIPs) in High Energy Physics (HEP) applications or X-ray radiation [83][84][85].

The benefits related to the use of these devices for such applications are due to the following features:

- spatial resolution: the pixel size is usually between 10 and 20 times the minimal size feature of the fabrication process;
- very low multiple scattering, because the substrate can, in principle, be thinned down to a few tens of microns;
- radiation tolerance, taking advantage of the reduced radiation sensitivity offered by current submicron VLSI processes. Typical radiation hardness requirements are in the order of Mrads or tens of Mrads and of 10^{14}- 10^{15} hadrons/cm^2 for space or high energy physics applications.
- high S/N ratios due to both the low noise and the amount of electron-hole pairs created by a single ionizing radiation interaction (values of 30 have been obtained for minimum ionizing particles) [86].

III.2 Interaction of photons with matter

Interactions of photons are fundamentally different from ionization processes of charged particles because in every photon interaction, the photon is either completely absorbed (photoelectric effect, pair production) or scattered through a relatively large angle (Compton effect) in the energy range below 1 MeV. As consequence of such a variety of interactions, a photon that interacts with the target is completely removed from the incident beam that is not degraded in energy but only attenuated in intensity.

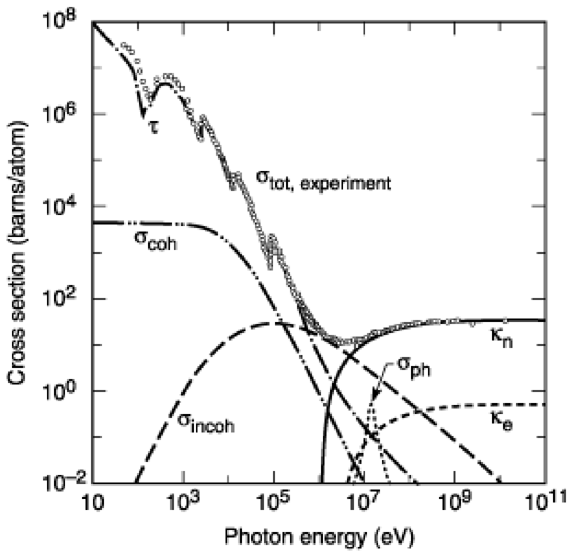

Figure III-3: Total photon cross section in carbon, as a function of energy, showing the contributions of different processes: σ_{coh} coherent scattering (photoelectric effect), σ_{incoh} incoherent scattering (Compton effect), κ_e and κ_p pair production. [86].

The attenuation of the incident beam is exponential with the thickness of the absorbing medium and can be expressed by the following Lambert-Beer relation:

$$I(x) = I_0 e^{-\mu x} \tag{III.2}$$

where μ is the linear attenuation coefficient, I_0 is the incident beam intensity and x the thickness of the material. The linear attenuation coefficient is related to the cumulative cross section of the material by the relation:

$$\mu = \eta_A \sigma_{tot} \tag{III.3}$$

where η_A is the number of atoms per unit of mass and σ_{tot} is the total cross section, that is the sum of all the cross sections of the interactions mentioned above and strongly depend on the material. A plot of the cross section as function of photons energy is shown in Figure III-3 where the contribution of the different interactions have been highlighted.

III.2.1 Photoelectric effect

In the photoelectric effect (the most important up to 100 keV) the photon interacts with an atom and an electron is ejected by the atom (Figure III-4). In this process, the photon disappears and its entire energy is first absorbed by the atom and then transferred to the emitted electron. The energy of the dislodged electron is given by the difference between the incoming photon energy and the atomic binding energy of the electron.

After the electron has been ejected from the atom, a vacancy is created in the shell, thus leaving the atom in an excited state. The vacancy can be filled by an outer orbital electron releasing a photon with energy equal to the binding energy. There is also the possibility of emission of Auger electrons [62], which are mono-energetic electrons produced by the absorption of characteristic X-rays internally by the atom.

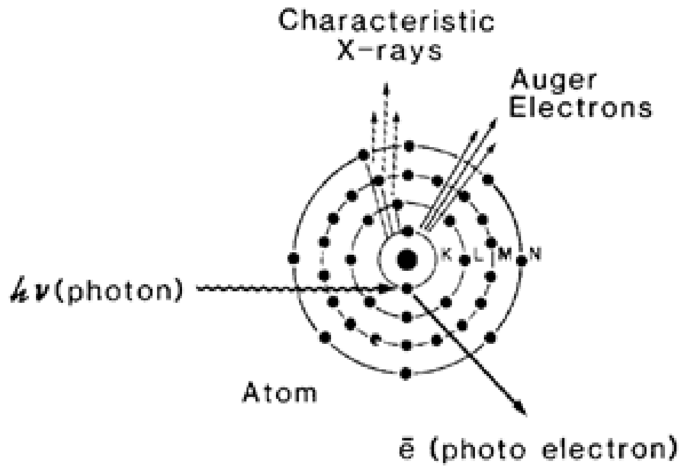

Figure III-4: Illustration of the photoelectric effect.

III.2.2 Compton interaction

Increasing the energy of incoming photons, the binding energy of the electron to the atom becomes irrelevant and the Compton interaction, which describes a collision between a photon and a free electron or a loosely bound electron in an outer shell, becomes important.

Compton interaction is an ionizing event, where the incoming photons transfer a portion of energy to the loosely bound electron that is scattered at a variable angle θ. The incoming photons with reduced energy is deflected through an angle ϕ with respect to the original trajectory, as visible in Figure III-5.

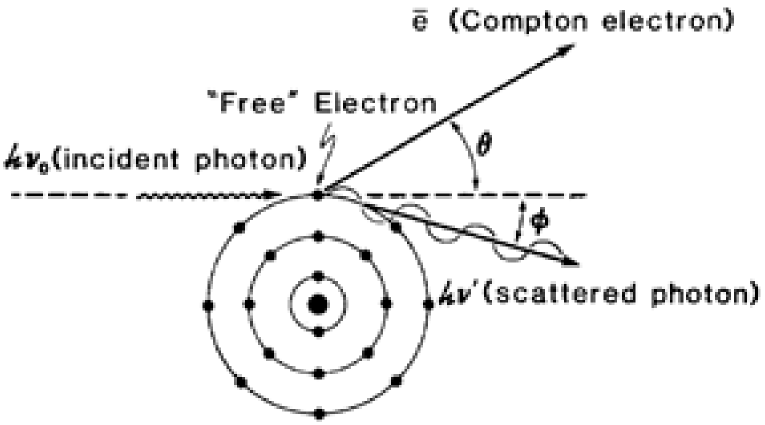

Figure III-5: Illustration of the Compton scattering.

III.2.3 Electron-positron pair production

The effect of the pair production happens when the energy of photons is higher than 1 MeV and it is observed to occur when the energy of a photon is twice the rest-mass energy of an electron (greater than 1.02 MeV).

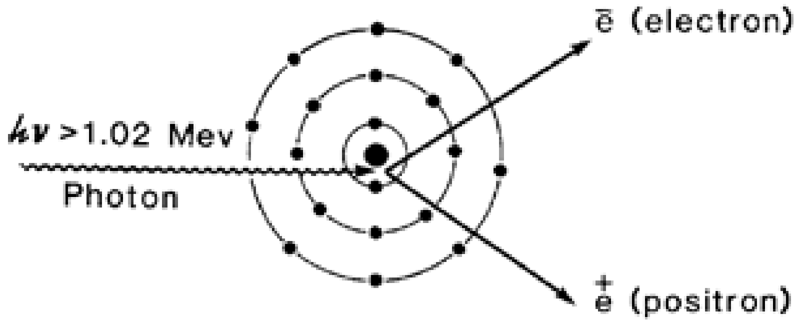

Figure III-6: Illustration of electron-positron pair production.

In this phenomenon the photon interacts with the nucleus and disappears to form an electron-positron pair (Figure III-6). All the remaining energy carried by the photon becomes kinetic energy shared by the positron and the electron. Because the positron will annihilate shortly (less than 1 mm) after slowing down in the absorbing medium, two annihilation photons of 511 keV are normally produced as secondary interaction products.

III.3 Image sensor as X-ray detector

The INFN RAPID project has analyzed the possibility to use the CMOS image sensor as X-ray detector for the energy range typical of the diffused photons during Interventional Radiology procedures. Several types of sensor were studied as X-ray detectors [89][90] both prototype and commercial device. In the Radiation Active Pixel Sensors (RAPS) INFN project, a dedicated CMOS sensor prototype realized in a 0.18 µm technology and featuring 10 µm pixel pitch and no epitaxial layer has been analyzed. Results show a reasonable efficiency for photon energies up to several tens of keV, and also a good energy resolution (3 - 4%) in the same energy range for the photons fully contained in the sensitive volume.
Moreover commercial devices were studied and in particular the possibility of using commercial MAPS as detectors for X-ray radiation and charged particles [91][92][93]. This kind of sensors features a high spatial segmentation (0.3 Mpixel) and each channel is sampled separately and has a dynamic range from 2 keV to 150 keV that allows to measure high photon fluxes (up to 100.000 photons $\cdot$ $mm^{-2} \cdot s^{-1}$) with small statistical uncertainty (~ 1%), without saturation effects.

III.4 The MT9V011 image sensor

The image sensor chosen for the RAPID system is the MT9V011 produced by Aptina Imaging (former Micron Imaging). Figure III-7 report its characteristic [94].

Parameter		Value
Optical format		1/4-inch (4:3)
Active imager size		3.58mm(H) x 2.69mm(V), 4.48mm Diagonal
Active pixels		640H x 480V
Pixel size		5.6μm x 5.6μm
Color filter array		RGB Bayer pattern
Shutter type		Electronic rolling shutter (ERS)
Maximum data rate/ master clock		13.5 MPS/27 MHz
Frame rate	VGA (640 x 480)	30 fps at 27 MHz
	CIF (352 x 288)	Programmable up to 60 fps
	QVGA (320 x 240)	Programmable up to 90 fps
ADC resolution		10-bit, on-chip
Responsivity		2.0 V/lux-sec (550nm)
Dynamic range		60dB
SNR_{MAX}		45dB
Supply voltage		2.8V ±0.25V
Power consumption		70mW at 2.8V, 27 MHz, 30 fps
Operating temperature		–20°C to +60°C
Packaging		28-Pin PLCC

Figure III-7: Summary of the Micron MT9V011 CMOS APS image sensor characteristics.

The sensor is a standard Video Graphics Array (VGA) CMOS sensor featuring a 668 × 496 pixels matrix and 5.6 × 5.6 × μm^2 of pixel size, with a 4.0 µm epitaxial layer. Even if the MT9V011's pixels array is 668 columns by 496 rows, the first 18 columns and the first 6 rows of pixels are optically black and can be used to monitor the black level. The last column and row of pixels are also optically black. The black row data is used internally for automatic black level adjustment. The package form factor is 11.43 × 11.43 mm^2 making it suitable for a wearable device. The registers of the sensor can be configured through a simple two-wire serial bus interface. The most important registers are the gain and the integration time. The gain can be adjusted from 1 up to 16, whereas the integration time can be adjusted from 56 µs to 267 ms, with a default value of 33.3 ms. The device also has a built-in 10-bit A/D conversion capability. The declared power consumption of the sensor is 70 mW with 2.8 V supply voltage and a maximum master clock frequency of 27 MHz. A schematic block diagram of the sensor is shown in Figure III-8.

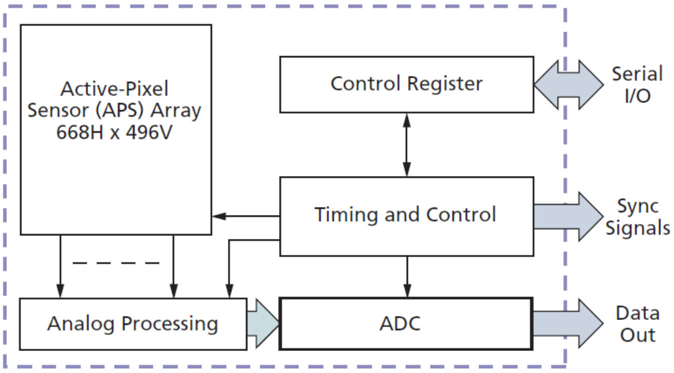

Figure III-8: Block diagram of the MT9V011 image sensor.

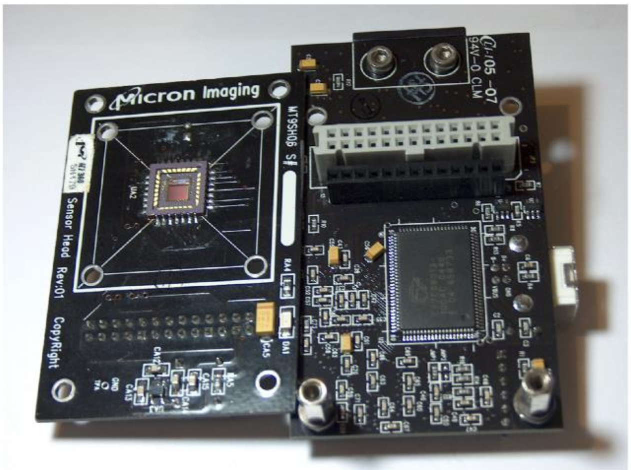

Figure III-9: The off the shelf data acquisition system (Demo2 board) on the right provided by the manufacturer and the image sensor board on the left.

The main building blocks are the following:

- APS array: it is the 668 × 496 active pixels matrix;
- analog processing: the analog pixel signal is filtered from noise components and its dynamic range is adapted to the ADC in order to maximize the Signal-to-Quantization Noise Ratio (SQNR);
- ADC: each pixel of the matrix is represented with 10 bits, which due to the transmission protocol are splitted in 2 bytes, resulting in more than 600 kB of information per frame;
- timing and control: it provides timing and control logic to the system;
- control register: these are the programmable digital registers of the sensor.

The readout of the sensor is performed by its demo kit, composed by two little boards: the sensor board (the PCB on left in Figure III-9) which contains the sensor, and the Demo2 board (the PCB on right in Figure III-9) that acts as interface between the sensor and a computer using a USB2.0 connection.

III.4.1 Analysis of MT9V011 sensor in dark condition

Before the evaluation of the sensor performances as X-ray dosimeter, the sensor response in absence of an external stimulus (dark conditions) has been performed to identify a mean value for the background level of the noise. A set of eight sensors has been characterized in dark condition as a function of different values of gain (1 -16), integration time (50 ms – 250 ms) and temperature (15°C – 30°C) (see Section III.5).

The characterization in dark condition was conducted in laboratory in a thermally controlled environment by using a climatic chamber and aimed to estimate the inter-chip variability. It should be underlined that during all the experiments the sensors are shielded from the ambient light.

III.4.1.1 Pixel pedestal and noise distributions

The first study concerned the determination of the average response of the single pixel in dark conditions. Figure III-10 reports the distribution of the single pixel of the matrix in dark conditions showing a small variation around the average value. The mean value and the standard deviation of the distribution are obtained with a Gaussian fit, considering the independence of the statistic fluctuation, in fact the χ^2 value confirms that the distribution of the single pixel is Gaussian. The mean value of the distribution is called *"pedestal"* (Fixed Pattern Noise) and the standard deviation *"noise"* (Time Dependent Noise). The distribution is essentially due to the thermal noise that produces the so-called "dark current" or leakage current.

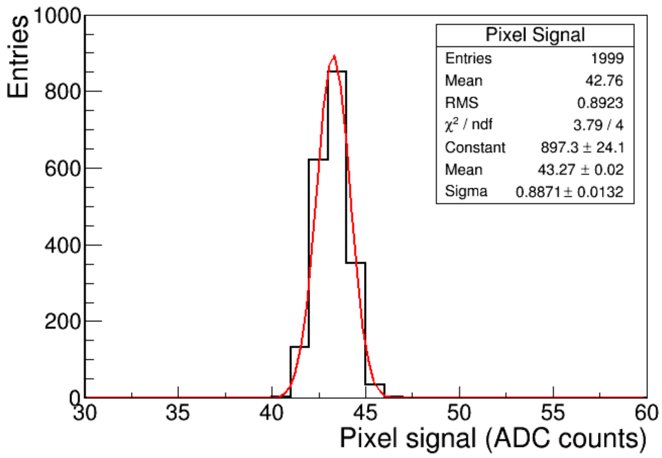

Figure III-10: Single pixel signal distribution (in this particular case the signal comes from the central pixel of the sensor matrix) in dark condition at temperature of 25°C, integration time of 100 ms and unitary gain.

The single pixel pedestal $V_{ped}(i,j)$ and noise variance $\sigma(i,j)$ have been defined in the following equations:

$$V_{ped}(i,j) = \frac{\sum_k V(k,i,j)}{N}$$
$$\sigma(i,j) = \sqrt{\frac{\sum_k \left(V(k,i,j) - V_{ped}(i,j)\right)^2}{N}} \quad \text{(III.4)}$$

where k is the index of the frame, i and j are the indexes of the row and column of the matrix, $V(k,i,j)$ is the ADC value of the pixel, and N is the total number of acquired frames.

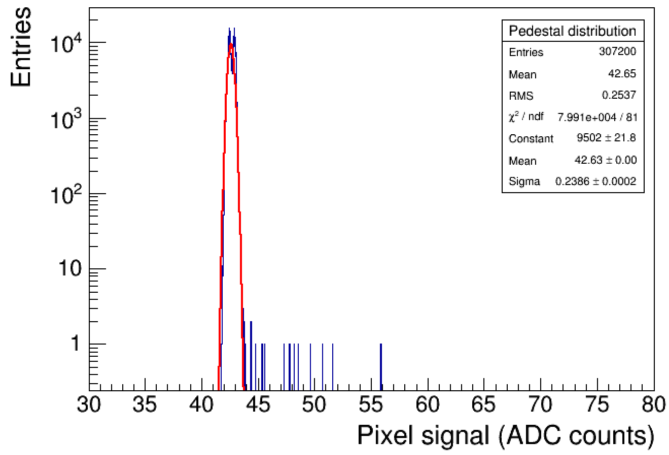

Figure III-11: Statistical distribution of pixel pedestals of the sensor. (100 ms integration time, temperature 25°C, unitary gain).

The pedestal and noise values can be used to characterize the response of the sensor matrix and an analysis of all the pixels has been performed. Figure III-11 shows the distribution of the pixels pedestal. The region of Gaussian fit in the range of 40-44 ADC counts contains almost all the pixels. The mean value of the pedestal in dark condition is 42.65 ± 0.25 ADC counts.

Figure III-12 shows the distribution of noise. The distribution is essentially Gaussian with a slight asymmetry toward higher noise values, and it is contained in the 0.7 - 1.5 ADC range. The mean value of the noise in dark condition is 0.87 ± 0.02 ADC counts.

The single pixel maps of the pedestal and noise, plotted in Figure III-13, shows that the sensor response is homogeneous all over the surface and that there are no gradients or asymmetries along any given directions. It should be also remarked that such uniformity, due to the requirements for an imager, will be very important in assessing the dosimetric capability of the device.

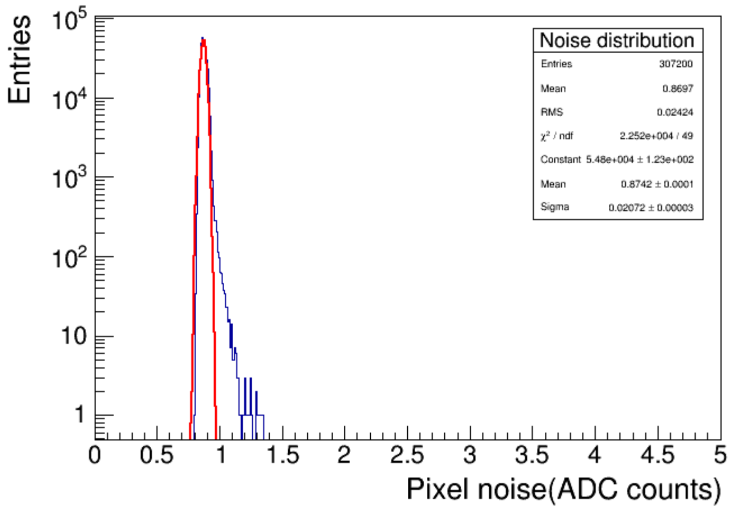

Figure III-12: Statistical distribution of pixel noise of the sensor A (100 ms integration time, temperature 25°C, unitary gain).

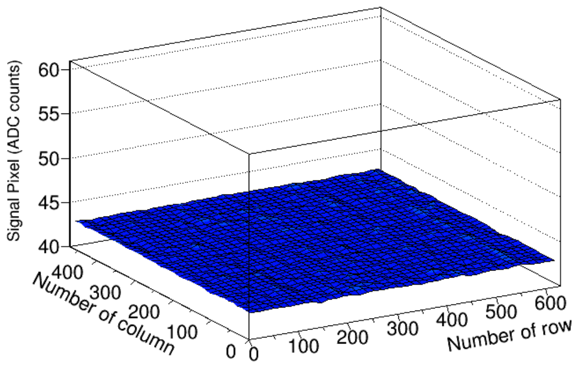

(a)

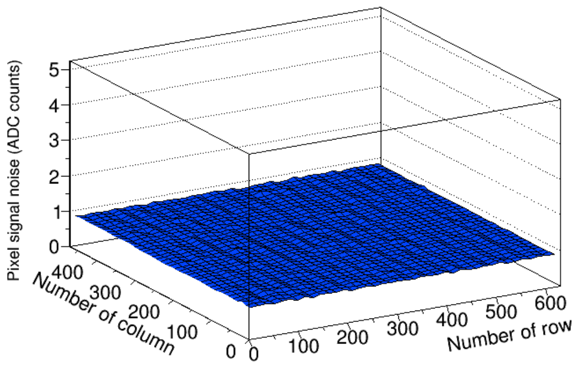

(b)

Figure III-13: (a) Single pixel map of (a) the pixel pedestals and (b) pixel noise for the sensor (100 ms integration time, temperature 25°C, unitary gain).

III.4.2 Photons identification algorithm

Several researches have pointed out the possibility to use the photon identification or photon counting technique for measuring the amount of energy deposited by the impinging photon beam in the sensor as a methodology to obtain dosimetric measurements [95][96][97].

These techniques are used for hybrid pixel detectors in which the generated charge is always contained inside a single pixel due to the dimension of the pixel size that is bigger than 200 ×200 μm^2. This technique is not as straightforward for a standard MAPS detector, where a single X-ray photon interacting within the sensitive volume of the sensor induces signal among adjacent pixels (Figure III-14): this signal sharing is caused by the diffusion of the generated electron-hole pairs that get collected by more than one pixel, resulting in a so-called cluster [95].

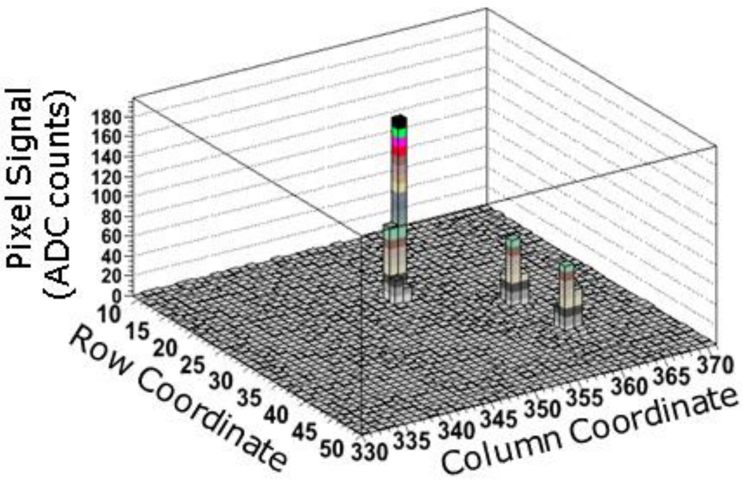

Figure III-14: Response of the sensor matrix where a photons hit the sensor

Moreover, the photons that interact with the sensor have different energies and the photon energy is only partially collected in the sensitive volume, depending on the charge collection efficiency profile of the sensor. For this reason a cluster photon counting algorithm was elaborated to better isolate the signal from the noise [76].

This algorithm is based on a two thresholds mechanism: a primary threshold ($V_{primary}$) to define the existence of a photon, and a secondary threshold ($V_{adjacent}$), to identify and measure the collected energy released by the incident photons in the sensitive volume. The formal procedure for selecting the thresholds has the goal to *i)* maximize the number of detected photons (i.e. maximize the efficiency) and minimize at the same time the number of false photons (primary threshold), that are detected because of noise fluctuations (i.e. minimize false positives) and *ii)* maximize the reconstructed photon signal (secondary threshold) by considering only the contribution of interested pixels and excluding those with noise fluctuations.

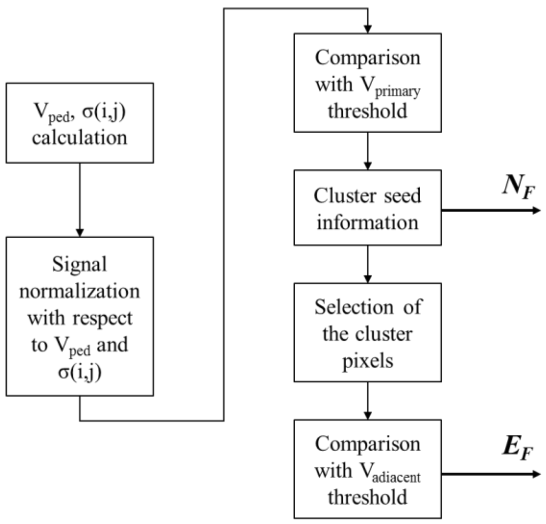

Figure III-15: Flow diagram of the cluster photon counting algorithm [76].

Figure III-15 shows the flow diagram of the photon counting algorithm. The algorithm requires the calculation of the pedestal and noise value for each pixel and the choice of the two threshold values.

The signal of each pixel has been normalized with respect to the pedestal and the pixel noise as from the following formula:

$$S(k,i,j)=\frac{V(k,i,j)-V_{ped}(i,j)}{\sigma(i,j)} \tag{III.5}$$

where $S(k,i,j)$ is the normalized signal value of the coordinate *i* and *j* for the *k*-th frame, $V(k,i,j)$ is the pixel signal value, $V_{ped}(i,j)$ is the pedestal value of the pixel and $\sigma(i,j)$ is the mean value of the pixel noise.

The normalized pixel signal of (III.5) is compared to the V_{primary}: each signal greater than V_{primary} is a candidate seed, i.e. the central pixel of the cluster. Then in order to verify that the candidate seed is an actual seed (i.e. a photon), a search for the pixel with maximum signal is done, based on the 3 × 3 matrix of the surrounding pixels. The total number of seeds in a frame is therefore equal to the first observable N_F, whereas the total photon signal of the cluster seeds and the other pixels belonging to the cluster is equal to the second observable E_F. A pixel belongs to a cluster if:

- the pixel is topologically connected to the seed, i.e. it shares at least one vertex or one side with it;
- the normalized pixel signal is greater than the V_{adjacent} threshold.

III.4.2.1 Justification of the choice of the threshold values

The best value for the V_{primary} threshold has been identified by considering the distribution and the integral of the normalized pixel signals of a single frame (Figure III-16). The condition to have few pixels over threshold without external stimulus is V_{primary} greater than 4.

The condition is different among different sensors and the threshold is different for each sensor. Generally it is in the range between 4 and 10 times the value of the single pixel noise which means a value between 3.6 and 8.9 ADC counts.

Concerning the $V_{adjacent}$ threshold a value between 2.5 and 3 times the single pixel noise is a safe choice, because the number of pixels that are topologically connected to the seed is small and up to 99.7% of noisy pixels get excluded from the signal integration.

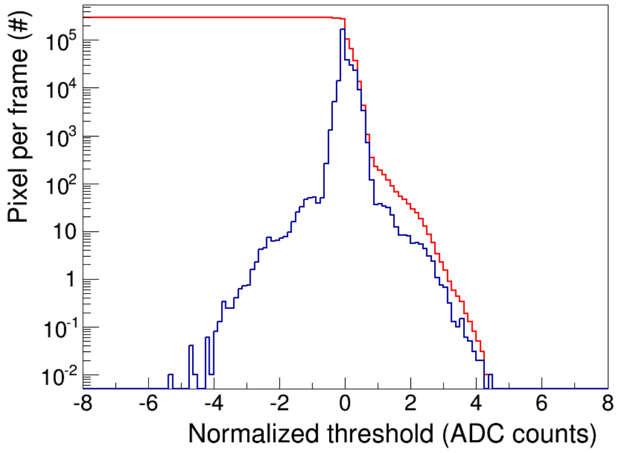

Figure III-16: Distribution (blue line) and integral distribution (red line) of the normalized signal for the sensor without external stimulus in dark condition.

III.4.2.2 Response of the sensor to single photons

The sensor has been exposed to an X-ray beam with photons at different energies in the range up to 60 keV. Each frame read from the sensor has been analyzed by identifying all the 7 × 7 cluster matrix where the central pixel of the cluster is over the $V_{primary}$ threshold and summing the contribution of the adjacent pixels over the secondary threshold $V_{adjacent}$.

Figure III-17 (a) shows the fraction of collected signal from the central pixel of the clusters as a function of the total value of the average cluster signal for incident photons of energy 17.5 keV (fluorescence X-rays from Molybdenum (Mo) target).

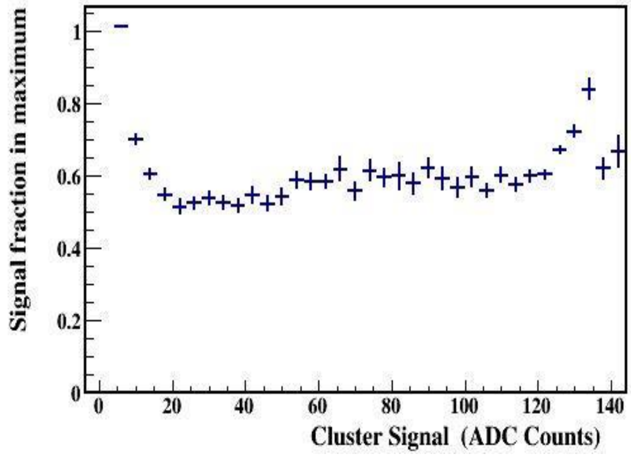

(a)

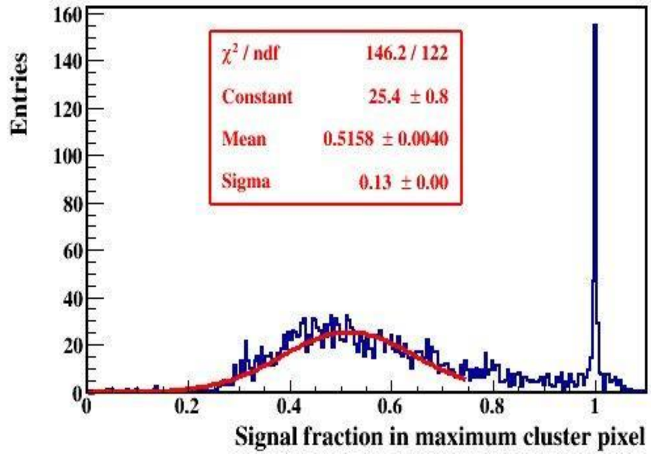

(b)

Figure III-17: (a) Distribution of the mean value of the fraction of signal collected by the central pixel of the cluster as a function of the total value of the cluster signal. (b) Distribution of the fraction of signal collected by the central pixel of the cluster for the photons at 17.5 keV.

In average the fraction of collected signal from the central pixel of the cluster is always more than 50%, therefore with a collected signal bigger than 10 ADC a primary threshold of 7 ADC would identify the vast majority of photons and should not depend on the collected energy of the incident photons.

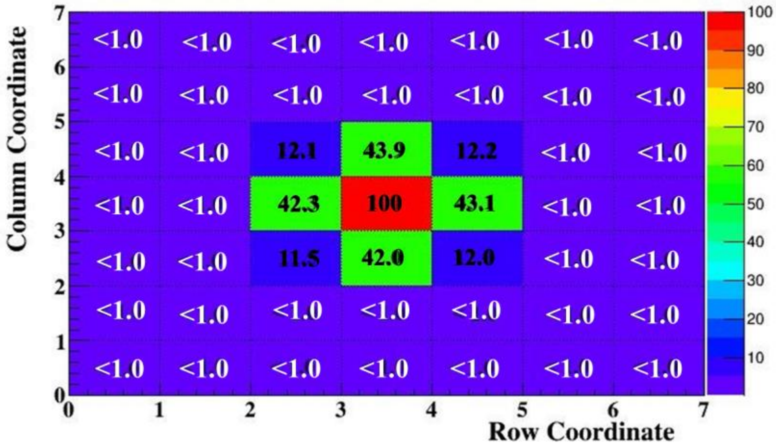

(a)

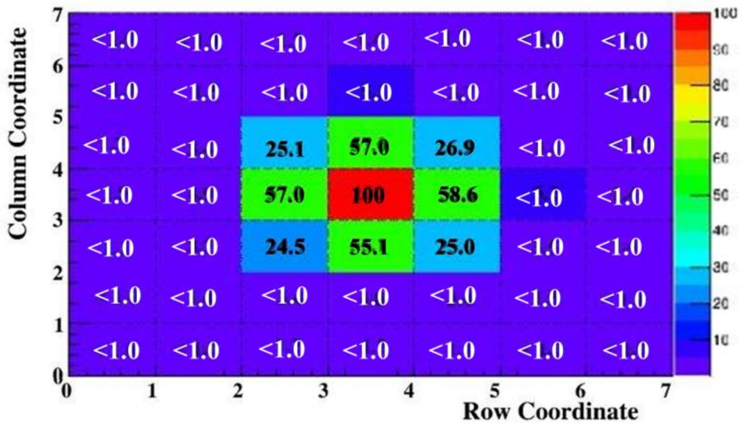

(b)

Figure III-18: Frequency counting of the pixel over a threshold three times the mean value of the noise signal for the 7×7 cluster matrix centered around the maximum pixel signal. (a) photons energy of 17.5 keV; (b) photons energy of 60 keV.

As a further crosscheck of the goodness of $V_{primary}$ choice, Figure III-17 (b) shows the distribution of the fraction of the signal collected by the central pixel of the cluster for all the events. Small deposited energy photons are represented in Figure

III-17 (b) in the region with fraction about 1, while the lower part of the distribution (below 0.5) is due to higher energy photons, with signal that is shared among several pixels. The most probable value is 50% and in the worst case the value is always bigger than 20% of the entire energy of the incident photons.
Concerning the secondary threshold V_{adjacent}, the value has been chosen equals to 3 times the mean value of the noise value $\sigma(i,j)$ of each pixel. The energy dependence of the cluster size has then been studied.
The dimension of the cluster is related to the energy of the incident photons and Figure III-18 (a) and (b) show the frequency in percentage of the pixels over the $V_{adjacent}$ threshold for the 7 × 7 cluster matrix respectively when on the sensor are impinging photons at the energy of 17.5 keV and 60 keV.
The normalization has been done with respect to the central pixel of the cluster that has the value of 100% (always selected). In both cases the number of pixels belonging to the cluster with a frequency of more than 2% is contained in the 5 × 5 matrix around the central pixel. The symmetry of the cluster matrix is evident with no preferential direction in the distribution of the collected signal of the incident photon. A symmetric charge sharing is visible in average for both orthogonal and diagonal directions, with similar fractions for symmetric pixels respect to the central one (Figure III-18). Besides, the diagonal pixels, due to the lower contact region of their sensitive volume with the central pixel's one, have a lower fraction. When the photon energy increases, the absolute value of the shared charge also increase, causing a bigger cluster in average.

III.4.2.3 Response of the sensor to the fully contained photons

The incident photons events with energy completely contained inside the sensitive volume of the sensor (fully contained photons) has been analyzed by evaluating the response for several photon energies in the range up to 60 keV (the maximum energy available in our laboratory).

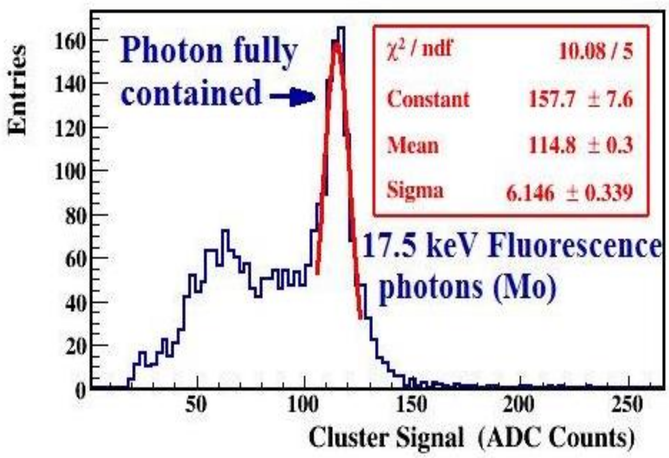

(a)

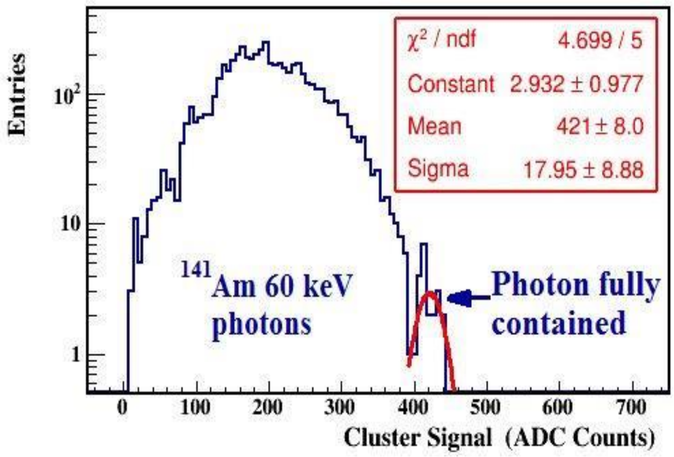

(b)

Figure III-19: Cluster signal for the sensor with an overlapping of the Gaussian fit in the region of the completely contained photons in the sensible volume for (a) photons of 17.5 keV and (b) 60 keV of energy.

Figure III-19 (a) and (b) show the response of the sensor for two photon energies, 17.5 keV (Mo) and 60.0 keV (Americium ^{141}Am), that depends on the different energy of incident photons. In particular, the fraction of events with fully contained signal is decreasing with the photon energy (integral area under the Gaussian fit). By considering the fraction of the events with fully contained photons signal, it is possible to build a calibration relation linking the deposited energy with the sensor signal expressed in terms of ADC counts.

Figure III-20 shows such linear correlation up to 60 keV and the calibration factor for this sensor is 6.93 ± 0.063 keV/ADC counts.

The next step is the determination of the correlation among incoming photon energy and number of pixels belonging to the cluster. Figure III-21 shows the linear correlation between the number of pixels obtained by considering the signal over the V_{adjacent} threshold as function of different energies of incident photons.

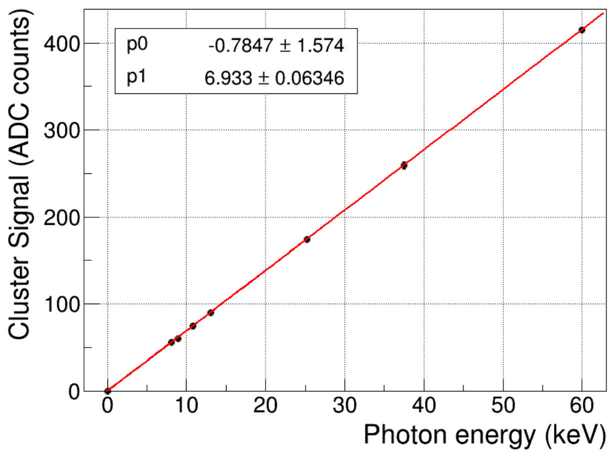

Figure III-20: Calibration of the sensor as a function of different energies of incident photons by considering the energy fully contained inside the sensible volume.

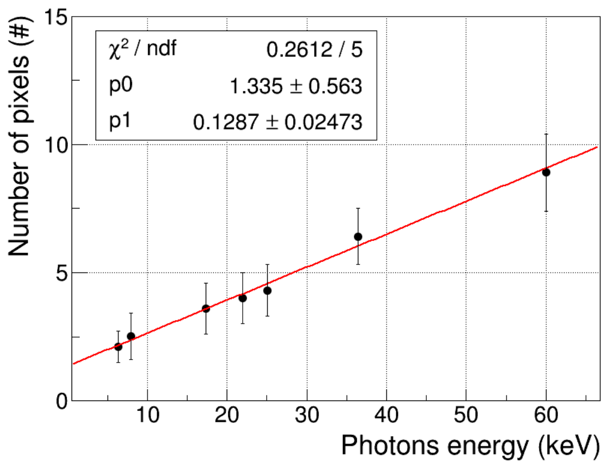

Figure III-21: Number of pixels with energy over the $V_{adjacent}$ threshold as a function of the incident photons energy.

III.4.2.4 Response of the sensor to the photons not-fully contained

The correlation between the number of pixels and the photons energy has been also evaluated by studying the response of the sensor to the photons with energy not completely contained in the sensitive volume (not-fully contained photons).

Figure III-22 (a) shows the number of pixels over the $V_{adjacent}$ threshold as a function of the cluster signal for photons at 31.4 keV. The blu circle identifies the photons completely collected inside the sensitive volume and the red circle identifies the region of the primary photoelectrons escaping almost immediately from the sensitive volume.

The remaining region contains all the photons that share the signal among adjacent pixels with a reduced signal collection. However there is an almost constant number of pixels over the $V_{adjacent}$ threshold regardless of the cluster signal. Figure III-22 (b) shows the average number of pixels as a function of the cluster signal for incident photons at 17.5 keV. It should be noted that the mean number of the pixels with a signal over the $V_{adjacent}$ threshold has a constant behavior after a certain value of the cluster signal. (over 40 ADC counts) valid for the 80% of the entire set of events. This characteristic is still valid also for other photon energies.

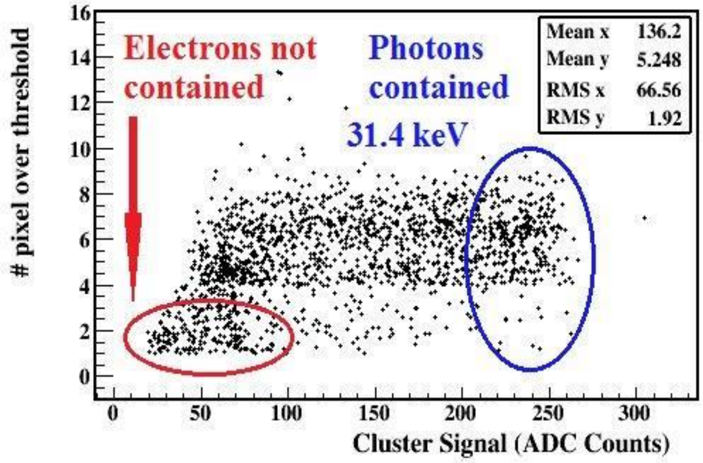

(a)

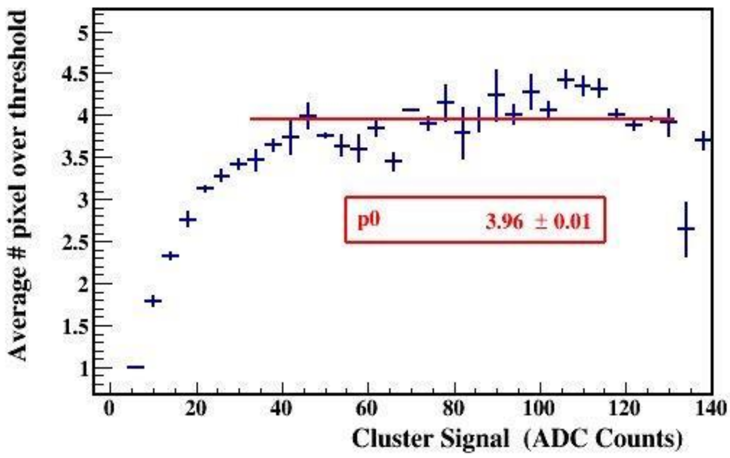

(b)

Figure III-22: (a) Number of pixels of the cluster as a function of the cluster signal for 31.4 keV of photon energy. The blu circle identifies the photons completely collected inside the sensible volume and the red circle identifies the region of the photons not completely contained in the sensible volume. (b) Mean number of the pixels over the $V_{adjacent}$ threhsold for the 17.5 keV as a function of the cluster signal.

Then we can defined a new observable linearly correlated to the incident photon energy as:

- N_F is the number of pixels in a frame belonging to a cluster with a signal over the V_{adjacent} threshold.

$$N_F = \sum_{k-th} \theta\big(S(k,i,j) - V_{adjacent}\big) \tag{III.6}$$

where *k-th* is the number of the frame and the function $\theta(x)$ is defined as $\theta(x) = 1$ for $x > 0$; $\theta(x) = 0$ for $x < 0$ with $x = S(k,i,j) - V_{adjacent}$.

A second observable (E_F) has been introduced to compensate the condition of intense fluxes of diffused photons in which the number of pixels over threshold could saturate:

- E_F is the sum of the energy of the pixels of the cluster matrix featuring a signal over the threshold.

$$E_F = \sum_{k-th} V(k,i,j) \cdot \theta\big(S(k,i,j) - V_{adjacent}\big) \tag{III.7}$$

III.4.3 The N_F and E_F dosimetric observables

The validity of the two variables, N_F and E_F, as dosimetric observables (i.e. proportional to the absorbed dose) has been demonstrated by considering the spectrum of the radiation diffused by the body of the patient for IRad procedures. To this purpose, the diffusion spectra obtained using a phantom made of PMMA slabs under the X-ray emission of an angiographic system have been measured for different medical protocols, spanning the entire range of variability of the X-ray tube parameters (i.e. tube voltage and current). The diffusion spectra (Figure I-8) have been recorded by using an Amptek X-123 spectrometer [43].

The total amount of energy of the incident photons, for each spectrum, has been evaluated and the corresponding number of pixels over threshold has been obtained by multiplying the number of photons of a given energy for the mean number of the pixels over threshold for such an energy by considering the relation in Figure III-21.

To study if the dosimetric observables yield the same response for the same amount of incident energy, the spectra have all been normalized to 10 µJ, and Figure III-23 shows the number of the pixels with signal over threshold. The measures are all distributed according to a Gaussian distribution with a RMS lower than 1% showing a homogeneity in the measure of the incident energy better than the typical figure of 10% of the passive dosimeters and an independency of the sensor response with respect to the emission spectrum of the same amount of energy.

The next step is to verify if the relation is linear with the amount of incident energy. Figure III-24 reports the correlation between the total number of pixels over threshold for a given spectrum and the integral of the spectrum (i.e. the incident energy on the sensor).

Once again the correlation is linear and the uncertainty on the fit parameters is smaller than 2%. These results have been obtained with the assumption that all the photons interact with the sensor (perfect detector). To transform the linear relation in a property between the absorbed dose in the sensor and the generated signal we have to multiply by the interaction probability of each photon with the sensor (Figure III-25).

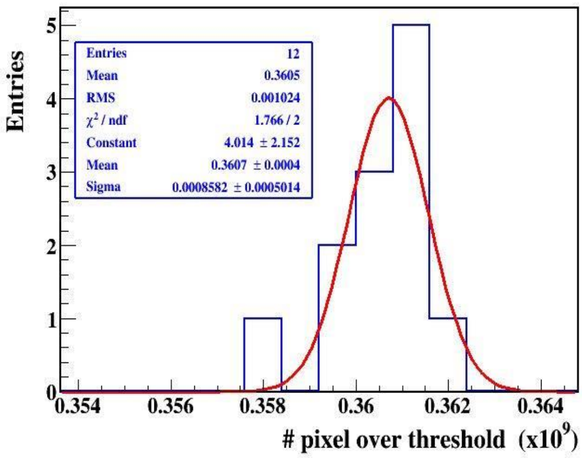

Figure III-23: Number of pixels over threshold for the twelve emission spectra normalized at the energy of 10 μJ.

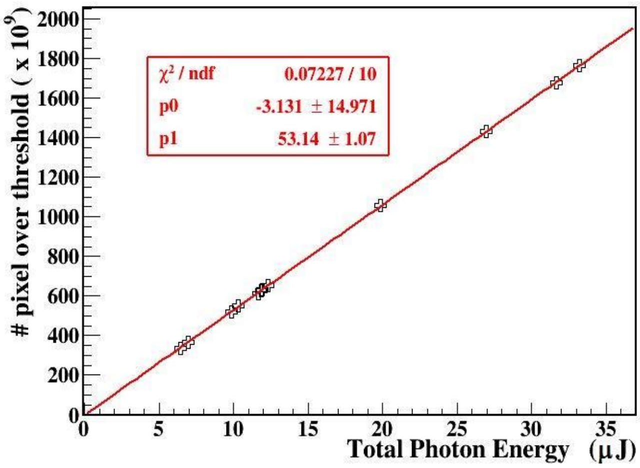

Figure III-24: Number of pixels over the $V_{adjacent}$ threshold for the spectrum of Figure I-8 as a function of the total energy of the spectrum for a perfect detector.

Figure III-25 reports the relationship between the attenuation coefficient of the protons in the silicon as a function of the photon energy in the interval 10-100 keV (obtained by means of the XCOM tool [98]). In this energy range, the attenuation coefficient changes by a factor of 20 for photon energies between 20 keV and 80 keV.

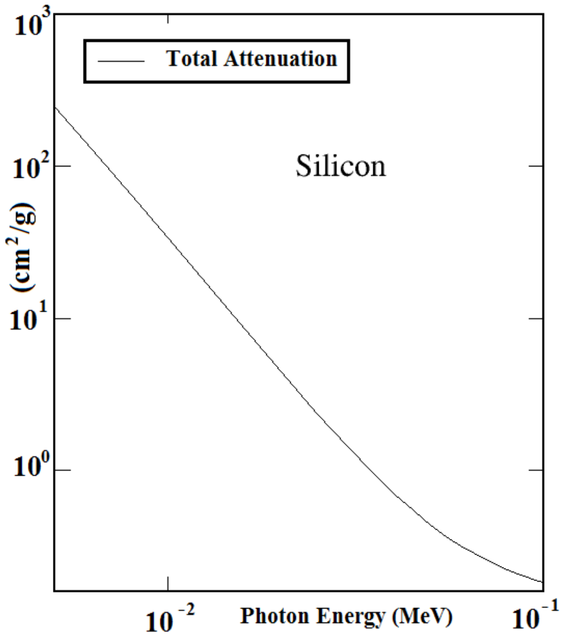

Figure III-25: Attenuation coefficient of the protons in the Silicon as a function of the energy in the interval 20-80 keV (obtained from the XCOM tool [98]).

Figure III-26 shows that the linear correlation between the dosimetric signal (number of pixels over threshold) and the incident energy holds even after the multiplication by the attenuation coefficient (red line). This confirms that the observable can be used to measure the dose rate and the total absorbed dose. Moreover the response of the sensor is independent of the different IRad procedures, the different parameters of the X-ray tube and of the diffused photon spectrum.

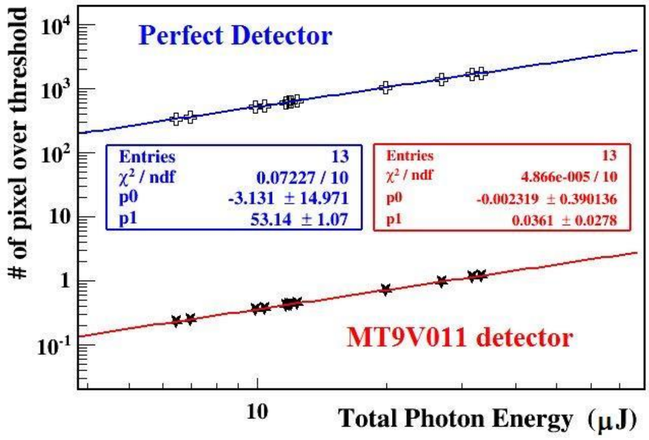

Figure III-26: Number of pixels over threshold for the perfect detector (blue line) and the MT9V011 sensor (red line).

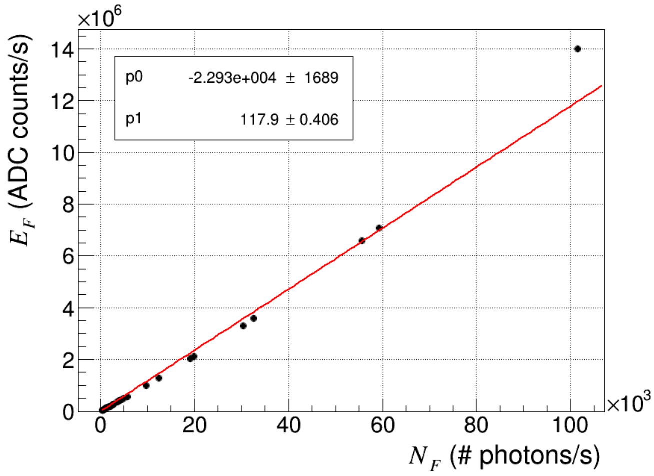

Figure III-27: Correlation between the integral value of the two dosimetric observables N_F and E_F for different acquisitions.

TABLE III-1
THE PEDESTAL AND NOISE VALUE OBTAINED FOR THE EIGHT MT9V011 SENSORS IN DARK CONDITIONS BY CONSIDERING AN AMBIENT TEMPERATURE.

Sensor	Pedestal (ADC counts)					Noise (ADC counts)				
	Integration Time (ms)					Integration Time (ms)				
	50	100	150	200	250	50	100	150	200	250
$MT9V011_A$	42,59	42,62	42,63	42,63	42,65	0.89	0.90	0.90	0.90	0.90
$MTV9011_B$	damaged									
$MTV9011_C$	42.62	42.65	42.69	42.71	42.76	0.81	0.81	0.81	0.81	0.83
$MTV9011_D$	42.35	42.37	42.40	42.42	42.46	0.80	0.80	0.80	0.80	0.81
$MTV9011_E$	42.53	42.55	42.6	42.61	42.64	0.88	0.88	0.88	0.88	0.88
$MTV9011_F$	42.52	42.56	42.58	42.60	42.63	0.85	0.86	0.86	0.86	0.86
$MTV9011_G$	42.36	42.37	42.40	42.41	42.43	0.87	0.87	0.88	0.88	0.88
$MTV9011_H$	42.51	42.53	42.57	42.58	42.61	0.90	0.90	0.90	0.90	0.90

To correct for eventual nonlinearity due to the counting algorithm the E_F observable has been introduced.

Figure III-27 shows the correlation of the integral value of the two observables and a good linearity for all the operating conditions can be observed except for the last point in which we have a very high photon flux that has been excluded during the fitting procedure. In this case, the high photon multiplicity leads to overlap neighboring clusters, thus reducing their detected number (N_F) without a further algorithm refinement. Instead the charge collected (E_F) in a frame is less sensitive to this working condition because cluster overlap will result in higher signal for the pixels thus recovering the information.

III.5 The inter-chip variability

A set of eight MT9V011 sensors has been characterized in laboratory in order to evaluate the variability of the pixels response among several sensors.

The response of the sensors has been evaluated in dark condition in order to calculate the pedestal and noise value by considering the ambient temperature and varying only the integration time. TABLE III-1 summarizes the value of the pedestal and noise as a function of different integration time values. From these values it is measured the inter-chip variability that is at the level of 0.06 % concerning the average pedestal value and at 0.1 % concerning the average noise value.

Moreover each sensor has also been calibrated by using the same procedure explained in the Section III.4.2.2. TABLE III-2 summarizes the calibration factor obtained for all the considered sensors.

TABLE III-2
THE CALIBRATION FACTOR OBTAINED FOR THE EIGHT SENSORS.

Sensor	X-ray calibration factor (ADC count/keV)
$MT9V011_A$	7.19 ± 0.23
$MTV9011_B$	damaged
$MTV9011_C$	6.93 ± 0.18
$MTV9011_D$	7.04 ± 0.14
$MTV9011_E$	6.77 ± 0.20
$MTV9011_F$	7.48 ± 0.24
$MTV9011_G$	7.15 ± 0.23
$MTV9011_H$	7.75 ± 0.21

The variability of the calibration parameters is within1 %.

III.6 Calibration with certified beam

The main goal of the characterization of the sensor as sensible element for a dosimetric system is to demonstrate that the behavior of the sensor is the same of certified dosimeters in IRad operating conditions.

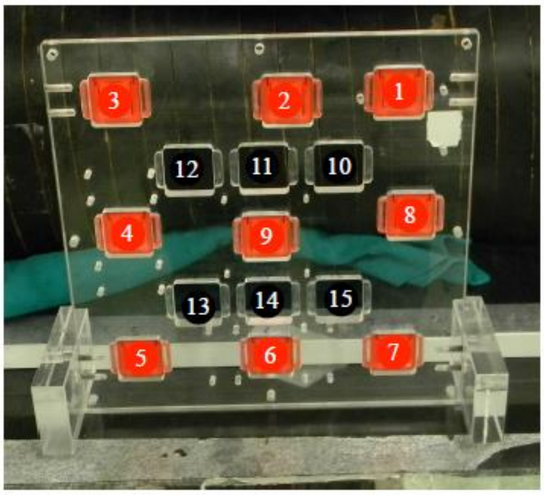

Figure III-28: TLDs in the plastic holder for geometrical mapping of the diffused radiation field in the transverse *xy* plane.

As described in Section II.3, TLDs are the certified devices adopted for radiation protection in IRad, but their operating principle is different from a MAPS: for a TLD the total dose equivalent is the relevant quantity, because it integrates X-ray radiation during procedures; for the CMOS sensor, on the other hand, the observable rate is more relevant, because charge is refreshed at each integration time.

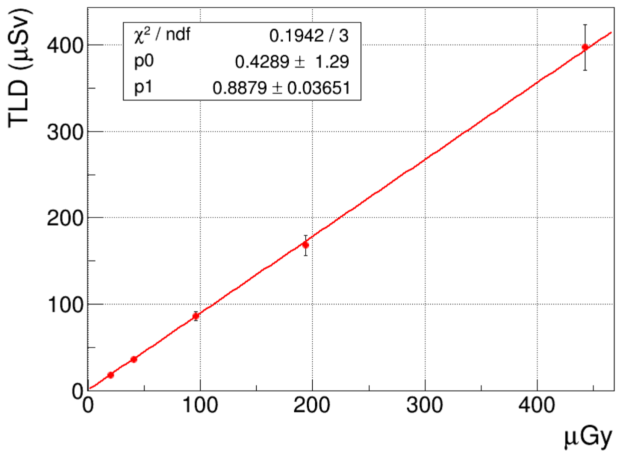

(a)

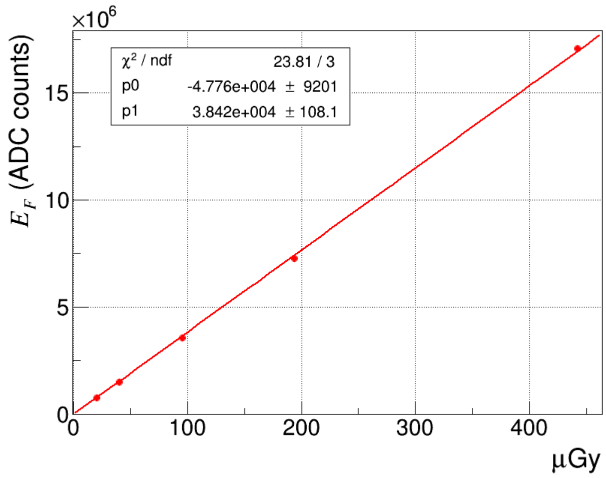

(b)

Figure III-29: (a) Correlation between kerma rate from certified beam and dose equivalent rate carried out from TLD measurements; (b) correlation between kerma rate from certified beam and rate of collected charge carried out from the MT9V011 sensor (100 ms integration time).

Therefore, the correlation should be investigated between the observable rates and the dose rate obtained by dividing the TLD dose equivalent by the irradiation time.

Both the sensor and the TLDs were calibrated with a certified X-ray beam at the Comecer calibration center (Castel Bolognese, Ravenna, Italy). For these measurements the TLDs were installed in the plastic holder in positions 8-10-12-13-15 (Figure III-28), while the sensor was placed in position 4.

For the calibration an A4-type beam was used, featuring an energy spectrum similar to that of the scattered X-ray beam radiation in IRad, with a peak in the 33 – 38 keV range (37.3 keV). Acquisitions were performed by using 100 ms of sensor integration time. The certified kerma rate was first compared with the average dose equivalent rate measured by the five TLDs.

The results, reported in Figure III-29 (a), show a linear correlation between the two quantities, with a calibration factor of 0.89.

Similarly, results can be linearly fitted for the correlation between certified kerma rate and the observable rate E_F (Figure III-29 (b)): the resulting conversion factor for calibrating the sensor with a certified beam is 38,420. A linearity is observed up to 450 μGy/s, where the detection efficiency of commercial APDs is reduced.

After applying the conversion factors to both the TLD and sensor measurements, a linear correlation with unitary slope is expected between them.

This was verified not only for the data acquired at the Comecer calibration center (Figure III-30 (a)), but also for those acquired during characterization in operating room, as shown in Figure III-30 (b). This confirms the correctness of the proposed approach and makes the MT9V011 sensor a suitable candidate to be use in the RAPID dosimetric system.

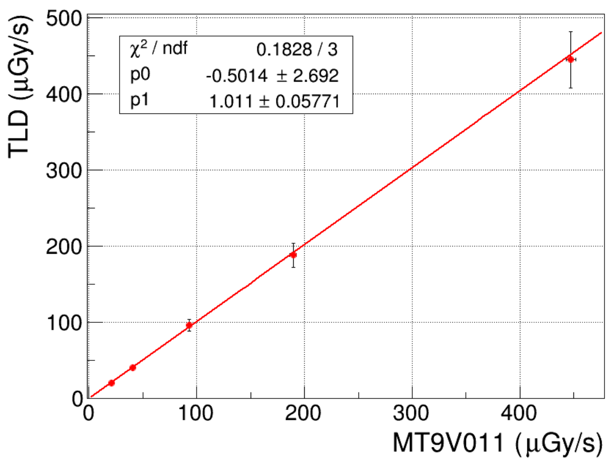

(a)

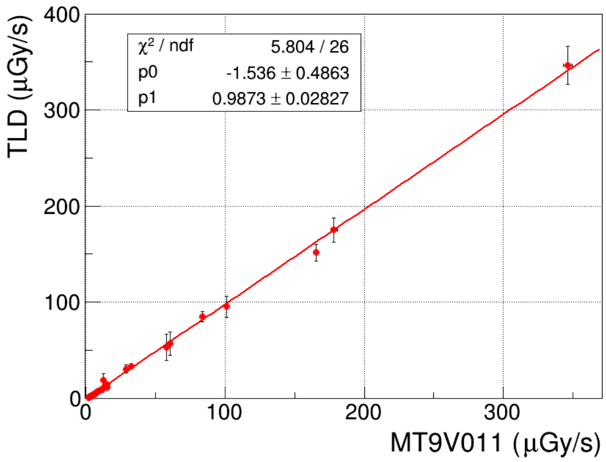

(b)

Figure III-30: Correlation between TLD dose equivalent rate and sensor rate of the collected charge obtained during acquisitions (a) at the Comecer calibration center and (b) in operating room and modified using the conversion factors determined in calibration.

Chapter IV

Design and implementation of the RAPID system

This chapter is focused on the design and implementation of the RAPID system. The realized architecture of the system has been described in detail of each building block. A Graphical User Interface (GUI) has been purposely designed for monitoring and controlling the data acquisition by using the C# programming language. Three different prototype versions of the system have been designed: *i)* the Prototype 1 aims to reduce the power consumption; *ii)* the Prototype 1.5 optimizes the wireless interface by using a compact solution for the RF antenna interface; *iii)* the final Prototype 2 integrates in a single board all the components increasing the portability of the entire system. Each prototype has been characterized in laboratory by focusing on the electrical and wireless interface performances.

IV.1 Requirements of the system

The aim of the RAPID project is to design a network of dosimeters to measure the dose and dose rate absorbed by the operators during the Interventional Radiology procedures. The monitoring network scenario (Figure IV-1) consists of one or more dosimeters, identified as Personal Sensor Nodes (PSNs), and a receiver unit. The operator wears the PSNs on the head and on the arms, each of which working as a transmitter unit, that collects data from the sensor, processes and transmits wireless packets. The receiver unit is located in a fixed position inside the operating room and it is connected to a remote station which merges and stores all the received data for off line data processing.

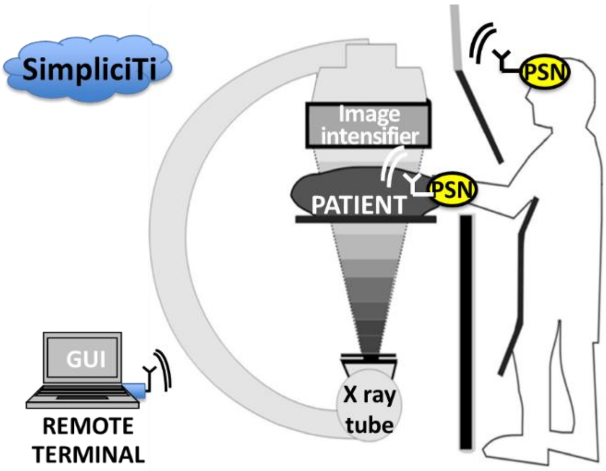

Figure IV-1: Monitoring network scenario inside the operating room. The operator wears the PSNs on the arms and on the hand.

The system requirements for the PSN are defined as following [77]:

- sensitivity to the energy spectrum of diffused X-ray photons for a typical IRad procedure (10 to several tens of keV) both in continuous and pulsed mode;
- dose and dose rate measurement accuracy better than 10% (current limit of passive dosimeters);
- real-time dose rate monitoring and off-line storage of the measurements;
- lightweight device with a small form factor to be wearable on the hand or/and on the arms of the operator;
- wireless device for indoor application (transmission range about 10 m). Previous studies have in fact shown the issues related to the use of wired devices [100];

- low power consumption with an operative time of about 8 h, compatible with the duration of different types of IRad procedures.

IV.2 The proposed system architecture

The main blocks of the proposed architecture of the system are reported in Figure IV-2 [101]:

- a commercial CMOS image sensor (MT9V011);
- a digital signal processing unit;
- a wireless interface and control unit;
- a remote station with a Graphical User Interface (GUI) for data acquisition.

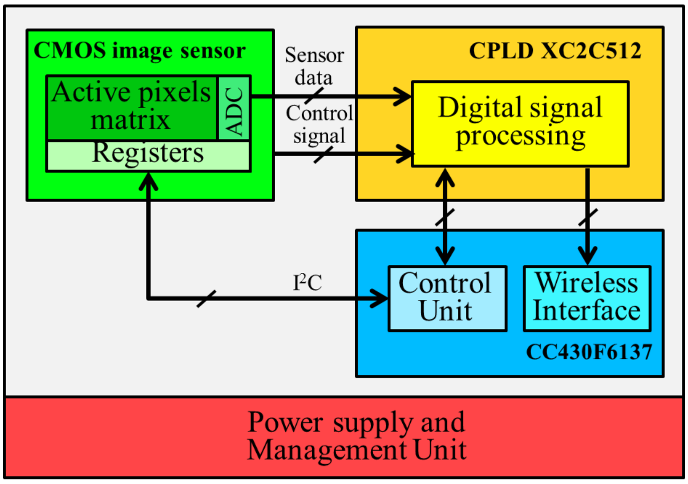

Figure IV-2: The block diagram of the PSN architecture.

As demonstrated in Chapter III, the MT9V011 commercial CMOS image sensor is suitable as sensing element for the specific application.

A digital signal processing unit, Complex Programmable Logic Device (CPLD), implements the data reduction algorithm that extracts two observables correlated to the dosimetric quantities. The data reduction algorithm reduces the amount of data to be transmitted by using a wireless transmission to the receiver unit.

The wireless interface and control unit are implemented in a System on Chip (SoC) (CC430F6137) provided by Texas Instruments, which combines a MSP430 core and a RF module together [102] and features of low power consumption. SimpliciTI® by Texas Instruments has been adopted as the wireless protocol: this protocol works in the Industrial/Scientific/Medical (ISM) frequency bands (915 MHz American standard, 868 MHz European standard) [103].

The receiver unit consists of a SoC (CC1111F32) provided by Texas Instruments, which integrates an 8051 core and a RF transceiver. The device, housed in a USB dongle, implements a serial communication to the PC, receiving data from the transmitter units and forwarding them to the PC [104]. A dedicated Graphical User Interface (GUI) has been implemented in the remote PC using the C# programming language to control the data acquisition of the PSNs.

IV.2.1 The MT9V011 sensor

The MT9V011 sensor as described in Section III.4 is a standard VGA image sensor with $5.6 \times 5.6\ \mu m^2$ pixel size and a package form factor of $11.43 \times 11.43\ mm^2$.

The most important signals of the sensor with reference to the system functionalities are summarized in the TABLE IV-1.

The sensor pixels are read-out in a progressive scan controlled by the LINE_VALID and FRAME_VALID signals. FRAME_VALID signal is asserted for all the duration of the sensor frame, while LINE_VALID is asserted during the read-out of a row of the sensor matrix. When LINE_VALID is asserted the one 10-

bits pixel data, DOUT [9:0], is output every PIXCLK period (Figure IV-3). The clock frequency of the sensor is 13.3 MHz.

TABLE IV-1
PINOUT DESCRIPTION OF THE MT9V011 SENSOR.

Pin name	Description
VAA, VAAPIX, VDD	supply voltage for the analog and the digital part (2.8 V)
CLK_IN	input master clock signal
DOUT [9:0]	pixel data output
PIXCLK	pixel clock output signal
FRAME_VALID	asserted during a frame of valid pixel data
LINE_VALID	asserted during a row of valid pixel data
SCLK, SDATA	serial bus (i.e. I^2C) signals

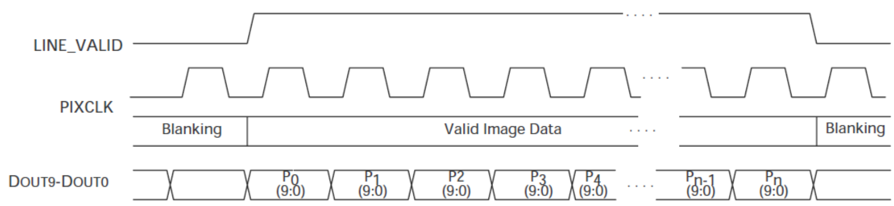

Figure IV-3: Timing diagram of the matrix sensor scan [94].

IV.2.2 The digital signal processing unit

The digital signal processing unit consists of a CPLD connected to the sensor and the SoC as shown in Figure IV-4.

The CPLD retrieves the data from the sensor and implements the data reduction algorithm, described in Section III.4, that consists of two different thresholds, a primary threshold ($V_{primary}$) and a secondary threshold ($V_{adjacent}$), used to measure the collected energy released by the incident photons on the sensitive volume. The flow diagram of the algorithm (Figure III-15) requires the calculation of the pedestal and noise value for each sensor pixel and the implementation of the equation (III.5) that calculates the normalized pixel signal before the comparison with the thresholds. The implementation of the equation (III.5) requires a lot of processing and memory resource to be compatible with the real-time requirement and the power consumption of the system.

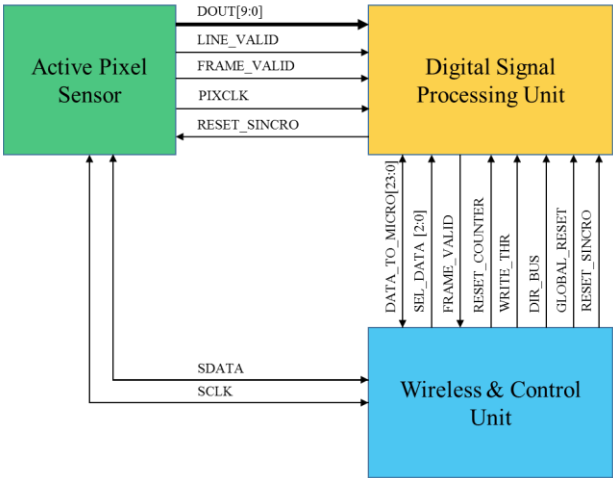

Figure IV-4: Block diagram of the interconnection between the sensor, the digital signal processing unit and the wireless/control unit.

A less demanding algorithm from the point of view of computational resources has been studied and implemented: a single threshold has been directly applied to the raw pixel value coming out from the sensor (Figure IV-5). The equation consists of:

$$V(k,i,j) > V_{threshold} \qquad \text{(IV.1)}$$

where the $V_{threshold}$ is the absolute threshold.

After the comparison of the pixels signal with the single threshold, two new system observables, correlated to dosimetric quantities [105], are calculated:

- *N* is the number of pixels over threshold in a sensor frame;
- *E* is the sum of the energy of the pixels over the threshold in a sensor frame (ADC counts).
-

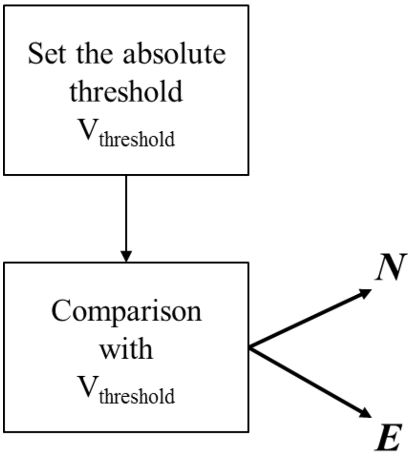

Figure IV-5: Diagram flow of the simplified one threshold algorithm.

It is important to point out that the decision of allocating the digital signal processing section to the transmitter unit instead of the remote terminal was driven by the requirement of real time operation. In fact the one-threshold algorithm implemented in the CPLD contributes to a significant packet size reduction for each frame acquired by the sensor without losing the information to reconstruct the dosimetric quantities. In the Chapter V, the performances of the simplified algorithm with respect to the complete algorithm will be described in more details.

The main block of the one threshold algorithm are reported in Figure IV-6 and consists of:

- a comparator between the pixel signal and the configured threshold;
- a 24-bit counter that computes the N observable;
- a 24-bit counter that computes the E observable;
- a 24-bit counter that computes the sequential counter for sensor frame (NUM_FRAME);
- a 24-bit counter that computes the N_{global} observable;
- a 24-bit counter that computes the E_{global} observable.

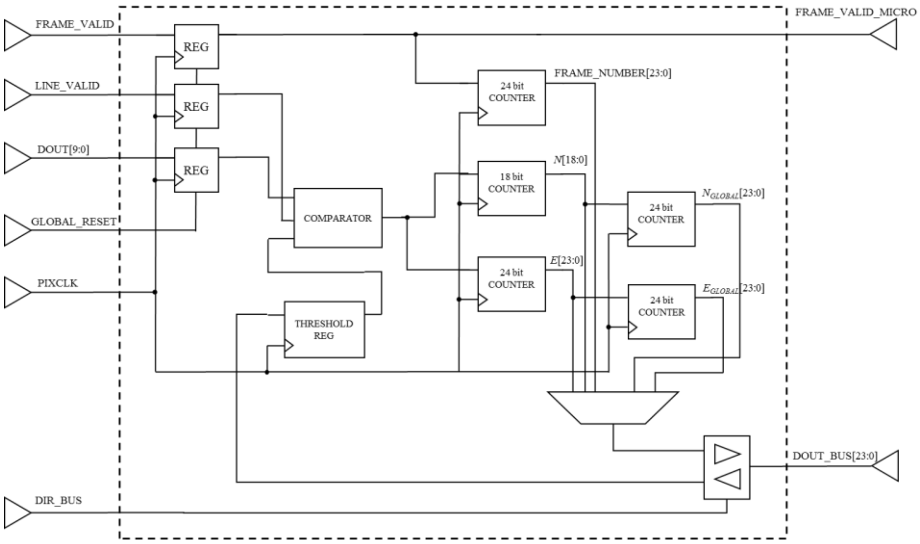

Figure IV-6: Schematic of the digital processing circuit logic implemented in the CPLD.

The sensor output signals (DOUT [9:0], LINE_VALID and FRAME_VALID) are connected to the CPLD and the PIXCLK signal is the master clock for all the sequential logics. Two resets are used: a RESET_SINCRO signal is used to synchronize the PSNs at the start of acquisition, whereas a GLOBAL_RESET is used to reset the logic of the CPLD.

The threshold, GLOBAL_THR [9:0], is a software-defined value configured by the user which is written into an internal register. The write operation is enabled by the WRITE_THR signal.

After the elaboration of a sensor frame, according to the SEL_DATA [2:0] signal (see TABLE IV-2 for the detailed coding), the selected results are received and elaborated by the SoC (DATA_TO_MICRO [23:0] bus).

TABLE IV-2
CPLD OUTPUT SELECTION OF THE MULTIPLEXER BY CONSIDERING THE SEL_DATA SIGNAL

SEL_DATA [2:0]	**CPLD output on the bus**
000	-----
001	E [23:0]
010	N [23:0]
011	GLOBAL_THR [9:0]
100	FRAME_NUM [23:0]
110	N_{GLOBAL} [23:0]
101	E_{GLOBAL} [27:4]
111	-------

The direction of the bus is controlled by an Input/Output (I/O) bidirectional tri-state buffer which uses the DIR_BUS enable signal:

- if DIR_BUS is low, DATA_TO_MICRO [23:0] is an output signal for the CPLD (corresponding to the multiplexer output);
- if DIR_BUS is high, it is an input signal for the CPLD (used to write the software-defined threshold value).

A sequential counter has been added to define a timestamp for the sensor frames. The counter is incremented each frame valid read from the sensor and it is used to monitor the lost packets because of the wireless interface.

The counter for the *N* observable and the *E* observable are reset after the elaboration of each sensor frame by asserting the RESET_COUNTER signal.

The logic resources inside the CPLD are also used to implement two counters to recover the information lost due to the wireless transmission. The observables, extracted from each sensor frame, are sent both wirelessly to the remote station and are accumulated in two internal CPLD counters to store locally the integrated value of the *N* and *E* observables during the entire IRad procedure. These two global counters are sent to the remote station only at the end of the acquisition to recover the information carried by lost packets.

The two counters, N_{Global} and E_{Global} (represented with 24bits), are defined by the following equations:

$$\begin{aligned} N_{Global} &= \sum_k N_{tot}^k \\ E_{Global} &= \sum_k E_{tot}^k \end{aligned} \qquad \text{(IV.2)}$$

where N_{tot}^k and E_{tot}^k are the values of the observables extracted each *k*-th sensor frame.

The digital processing circuit is described in VHDL (Very High Speed Integrated Circuit Hardware Description Language) and the design flow is elaborated by using the ISE Xilinx environment.

Functional verification has been performed by using the ModelSim environment by Mentor Graphics in order to prove that the circuit to be implemented on CPLD meets the timing requirement driven by the user clock frequency.

IV.2.3 The control/wireless unit

After the elaboration provided by the digital signal processing unit, the results of the algorithm should be sent to the remote station through the wireless link by using a CC430 Texas Instrument SoC featuring of RF device. An interrupt mechanism is used for the data transmission between the CC430 and the CPLD devices: a request is produced at the falling edge of the FRAME_VALID signal to transmit the elaborated results from the algorithm.

The SoC controls the I^2C signals used to configure the sensor register and the signal from/to the CPLD.

The firmware implemented in the SoC is summarized in the flow diagram of Figure IV-7.

After the power-on of the system, the start-up operation is the initialization of the pinout and of the wireless interface; then the SoC operates with an interrupt mechanism based on commands sent by the GUI software.

A *Time Division Multiple Access* (TDMA) scheme has been implemented to manage the transmission of several PSNs sharing the same frequency channel. An unique identifier has been associated to each PSN to identify the system and the dedicated time slot for the data transmission.

A set of seven remote commands are used:

- DISCOVERY: a broadcast message is used to discover the dosimeters available on the network. If the dosimeter is available on the network it sends back the own identifier;
- READ_REGISTER: read the selected sensor register through I2C and send the value to the remote PC;
- WRITE_REGISTER: write the selected sensor register through I2C and read back the written value;

- READ_THRESHOLD: read the threshold value stored in the threshold register inside the CPLD and send the value to the remote PC;
- WRITE_THRESHOLD: write the threshold value in the threshold register of the CPLD;

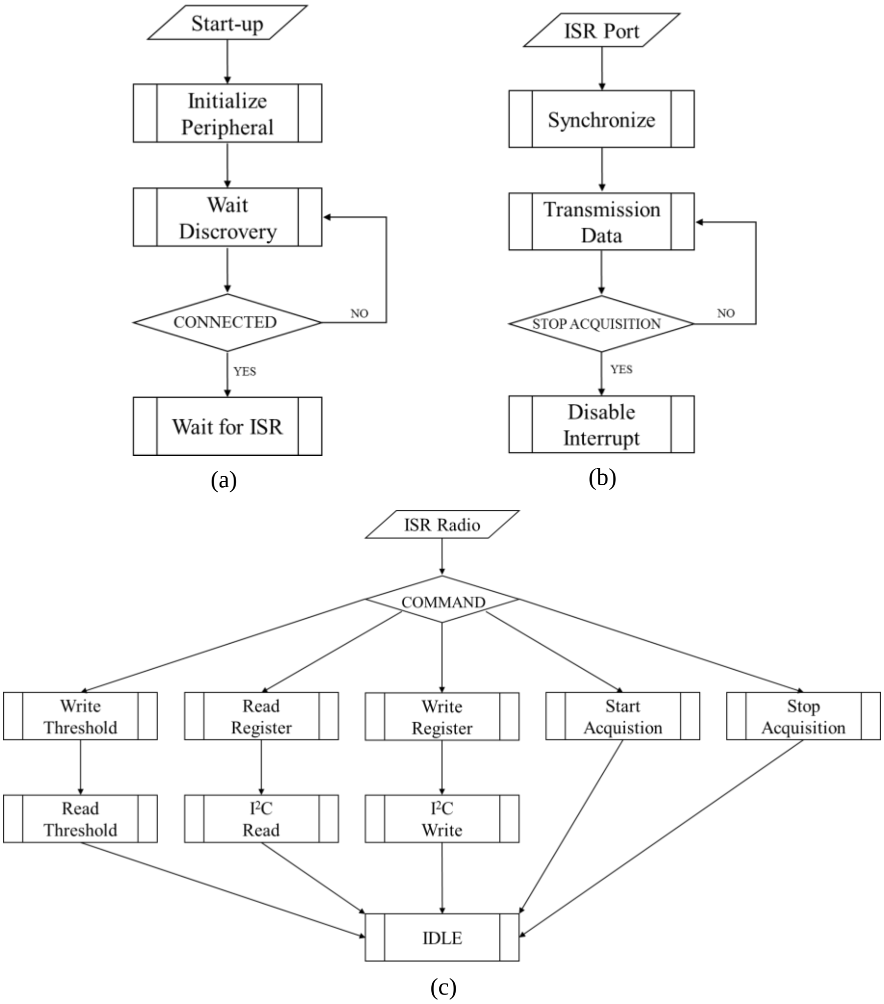

Figure IV-7: Flow diagram of the firmware implemented in SoC CC430F6137 for (a) start-up operation, (b) data acquisition and (c) remote command execution.

- START_ACQUISITION: enable interrupt request (IRQ) on the falling edge of the FRAME_VALID signal. At the end of each frame, in the interrupt service routine (ISR), the *N* and *E* observables and the FRAME_NUM value are read from the CPLD by setting the SEL_DATA signal according to TABLE IV-2; a RESET_COUNTER pulse is then produced for initializing the counters in the CPLD. A synchronization phase has been performed at the start of acquisition skipping the number of frames in according to the identifier in order to separate the time slot for the transmission of each PSN;
- STOP_ACQUISITION: disable IRQ and the result of two global counters are sent to the remote PC.

The format of the transmitted packet is shown in Figure IV-8. The first byte contains the identifier number (ID) of the PSNs. Three bytes are used for the *N* and *E* observables. The last 3 bytes are the sequential counter.

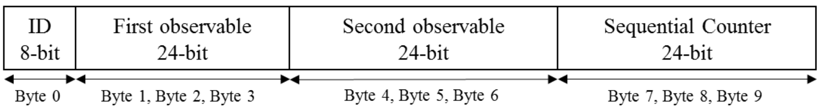

Figure IV-8: Wireless packet format.

The information of five consecutive packets is put together in order to create a global wireless packet of 51 byte long that is sent to the remote PC.

IV.3 The Graphical Unit Interface

A dedicated Graphical User Interface has been implemented in the remote PC using the C# programming language. The software has been purposely designed for data acquisition from several PSNs. Its main functions are: *i)* open and close the wireless connection between the terminal and the single PSN; *ii)* configure the sensor registers; *iii)* configure the threshold value used by the data reduction algorithm; *iv)* start and stop data acquisition; *v)* real time graphical data monitoring of the acquisition. Acquired data are saved in a file with the information of the frame number for off-line data analysis and a log file is produced containing the configuration parameters of the acquisition.

A main control panel manages the wireless connection between the receiver and the PSNs, the start/stop procedure for the data acquisition and performs a real time graphical data monitoring in order to display the data and to trigger immediate action in case of problems during acquisition. A configuration panel has also been designed for configuring each PSN.

IV.3.1 The main control panel

The main control panel has been designed to manage the acquisition from the transmitter unit (Figure IV-9). Its main operations are the opening and the closing of the connection, the start and the stop of the acquisition and the real time graphical data monitoring of the measured dose-rate.

The *"Search for Dosimeters"* button, box (a) of Figure IV-9, performs a scan of the dosimeters available on the network and when the dosimeter is available displays the dosimeter with its identifier. The status of the configuration and the configuration parameters are also reported.

Each dosimeter can be disabled or enabled from the GUI:

- if the dosimeter is enabled, a green circle is visible near the dosimeter (text box (a) of Figure IV-9). The configuration parameters are displayed in the text box below the dosimeter;

- if the dosimeter is disabled, a red circle is visible near the dosimeter (text box (a) of Figure IV-9). The dosimeter is removed from the network and from the acquisition.

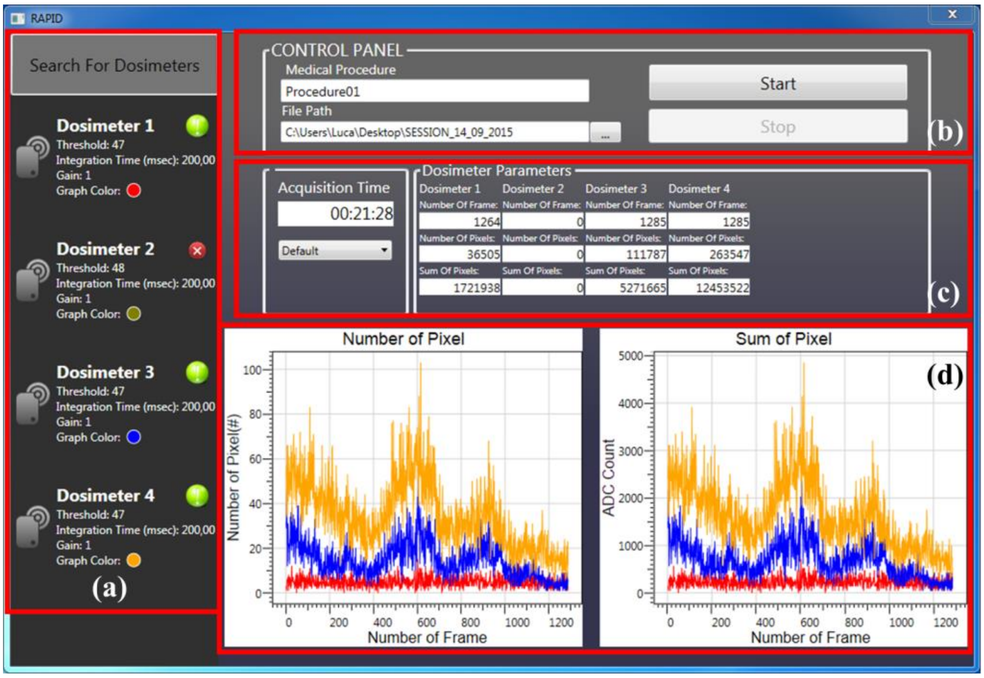

Figure IV-9: Screenshot of the main control window of the GUI implemented in the remote terminal: (a) the list of the available dosimeters are displayed with the status of configuration; (b) the buttons "Start and Stop acquisition" that control the data acquisition procedure; the text box is used for defining the kind of IRad procedure; (c) the information of the acquisition status of all the configured dosimeters; (d) the real-time graphical monitoring.

The acquisition is controlled by using two buttons, box (b) of Figure IV-9, *"Start Acquisition"* and *"Stop Acquisition"*. The name of the procedure can be inserted in the text box and a directory has been created containing the configuration files for each dosimeter, the log file for the acquisition and the data acquisition file (Figure IV-10).

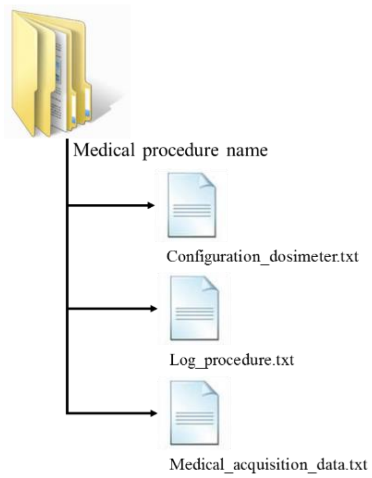

Figure IV-10: The file tree generated by the acquisition system at the beginning of the acquisition.

In the box (c) of Figure IV-9, the duration time of the acquisition has been reported. In addition the acquired values of each dosimeter for the two observables and the number of frames have been monitored.

Finally in the box (d) is shown the real-time graphical monitoring for the two observables recorded by each dosimeter.

IV.3.2 The configuration panel

A dedicated control panel has been designed to configure the acquisition parameters of each PSN (Figure IV-11). The main operations are the configuration of the sensor registers and the definition of the threshold value for the data reduction algorithm.

The latter is performed by using a threshold scan procedure in dark conditions, as shown in graph (a) in Figure IV-11. The choice of the correct threshold is dictated by the request of having few pixels over threshold for each frame due to the noise fluctuations, as well as to measure the noise level. The threshold value chosen by the scan procedure is shown in box (b) of Figure IV-11. The range of the threshold scan for this procedure (hence for the abscissa of graph (a) in Figure IV-11) has to be defined starting from the sensor characterization in dark conditions.

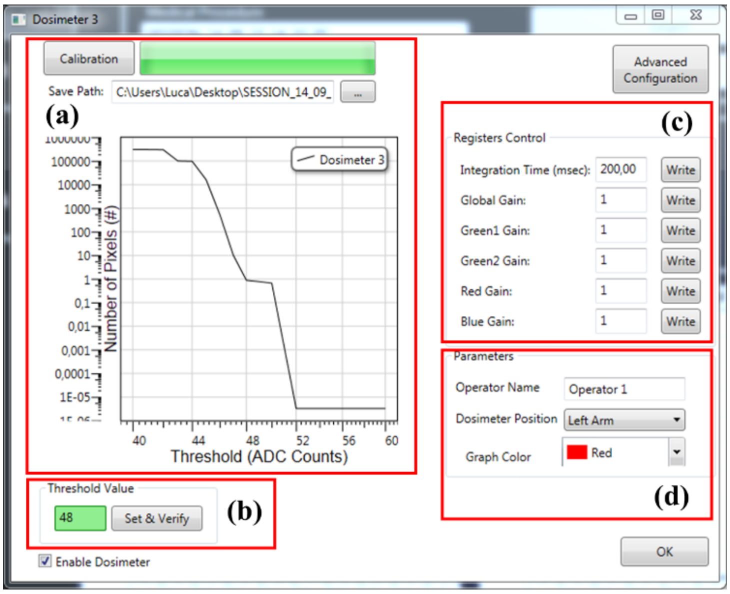

Figure IV-11: Screenshot of the configuration windows of the GUI implemented in the remote terminal: (a) the mean value of the integral number of pixels over a threshold as a function of the threshold itself; (b) the value of the threshold chosen by the scan procedure; (c) integration time and gain selection; (d) name of the operator and position of the dosimeter.

From an extensive characterization of each sensor in dark condition, the mean and RMS values of the pedestal distribution (the mean output value of a single pixel, 42 ± 0.2 ADC counts) and of the single pixel noise distribution (0.89 ± 0.02 ADC counts) have been obtained. While the pedestal distribution is usually Gaussian like with few bad pixels, due to the good quality of the sensor production process, the noise distribution is asymmetric as reported in [106].

In order to define the range for the threshold scan, being 41 the lowest pedestal value, for the minimum value we have chosen 40 because a lower value would essentially yield 100% of pixels over the threshold, while we are interested in getting just few pixels over threshold. For the maximum limit, starting from the greatest value of the pedestals, 47 ADC, and adding 5 ADC (5 times the single pixel noise) to take into account the fluctuation of each pixel due to the noise, an upper value of 52 has been obtained. To this value we have added 8 ADC counts to take into account possible variations due to different environmental conditions, either in laboratory or in operating room, bringing the scan range to 40-60 ADC counts.

The influence of the choice of the number of frames to be used for each point of the threshold scan has been evaluated by performing several procedures and studying four different values of the threshold. Figure IV-12 shows that the mean value of the number of pixels over threshold is stable after 50 frames for each point of the scan. Then if we consider 50 frames for 21 points of the threshold scan and a sensor integration time of 200 ms, the average time needed for finding the threshold value is about 3 minutes for each sensor connected to the transmitter unit.

Regarding the sensor configuration, two main parameters can be varied, visible in the box (c) of the Figure IV-11: integration time (41 µs - 267 ms) and gain (1 - 16). A unitary gain has been selected to avoid saturation of the dynamic range for each pixel, especially for high photon flux conditions. On the other hand, the choice of the integration time impacts the number of photons detected in a single frame, as shown in the plot in Figure IV-13 for the *E* observable with a threshold fixed at 55 ADC counts. A constant behavior can be observed for all the integration times from 50 ms up to 250 ms for a value of the threshold equal to 48 ADC counts. We chose 200 ms as operating point, to allow the collection of enough photons in a single frame, even in low flux regimes and reducing the relative uncertainty due to Poissonian fluctuations, as described in [77].

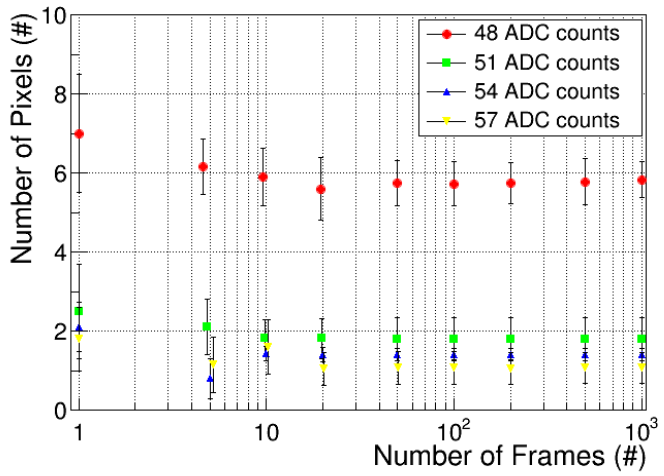

Figure IV-12: Mean value of the integral number of pixels over threshold normalized to the number of frames for four different threshold values as a function of the number of frames.

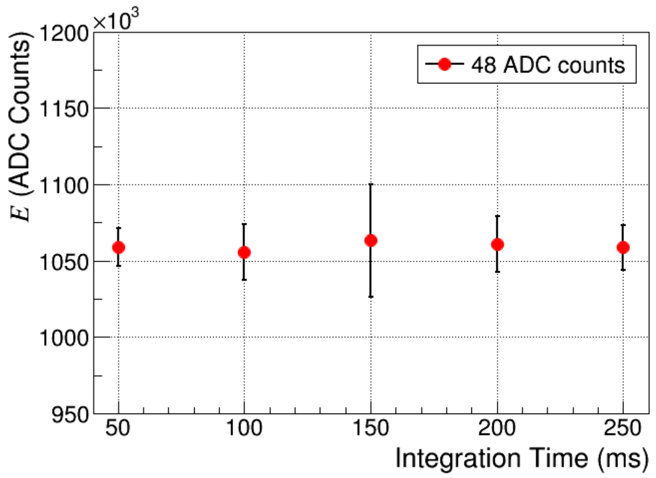

Figure IV-13: *E* observable as a function of the integration time for the 48 ADC counts value of threshold.

Finally to complete the description of Figure IV-11, in the box (d) we can specify the name of the operator and the position of the transmitter unit (arm, body or head).

IV.4 Design and implementation of the system Prototypes

In this section we describe the different versions of the realized prototypes by highlighting the improvement of each version with respect to the previous one.
An early version of the PSN (Prototype 0) was realized by assembling the manufacturer provided development boards for the different components in order to focus on the verification of the sensor functionality with respect to the integration of the system [107]. Three different versions of the same system have been designed: *i)* the Prototype 1 aims to reduce the power consumption; *ii)* the Prototype 1.5 optimizes the wireless interface by using a compact solution for the RF antenna interface; *iii)* the final Prototype 2 integrates in a single board all the components increasing the portability of the entire system.

IV.4.1 Prototype 1

The Prototype 1 has been designed with the aim to reduce the power consumption of the system and it consists of a custom board that integrates the sensor and the digital signal processing unit. It provides a vertical strip connector for the wireless evaluation board CC430F6137 provided by Texas Instrument (Figure IV-14). A cascade of power regulators generates, from the external supply voltage of 3.6 V, the 3.3 V for the SoC and the Input/Output of the CPLD, the 2.8 V for the sensor and the 1.8 V for the core of the CPLD. The power has been distributed by using embedded planes and a common ground plane has been used for all the components. Test points have been used to measure the supply current on each regulator.

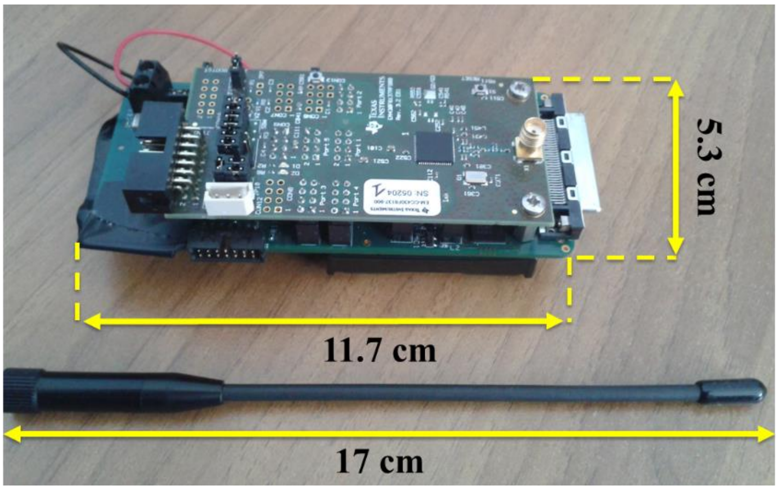

Figure IV-14: The realized Prototype 1

IV.4.1.1 Electrical characterization

The power consumption of the Sensor Node has been assessed by separately measuring the supply current provided to the image sensor, the CPLD and the SoC. A digital multimeter has been positioned in the measurement points highlighted in Figure IV-16; the current consumption is measured during the operative conditions. TABLE IV-3 summarizes the comparison of the power consumption between the two prototypes, Prototype 0 and Prototype 1.

It can be noted that the external power has been reduced from 5 V to 3.6 V in order to be compatible with the typical voltage of a mobile phone battery. The relevant contribution to the power consumption in the Prototype 0, due to the Altera CPLD core (EPM7256SQC208) [108], is reduced in the Prototype 1 by using the last generation of low power CPLD (XC2C512 by Xilinx) [109]. The total power consumption has been reduced from 900 mW to about 200 mW.

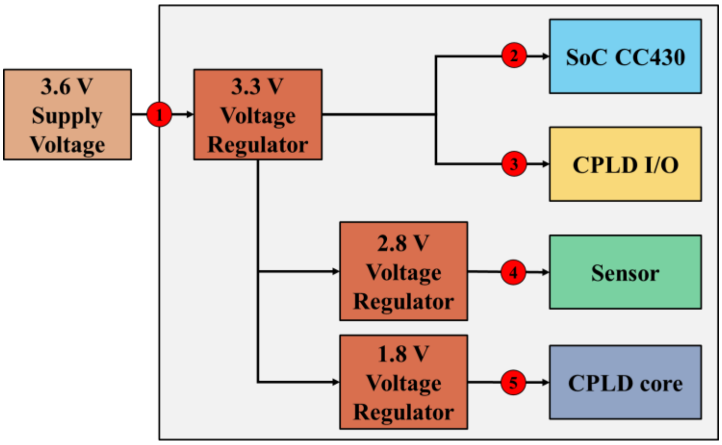

Figure IV-15: Block diagram of the Sensor Node boards; current measurement points are highlighted with red dots.

TABLE IV-3
POWER CONSUMPTION COMPARISON BETWEEN THE PROTOTYPE 0 AND THE PROTOTYPE 1.

Measurement points	**Device**	**Prototype 0 Supply current (mA)**	**Prototype 1 Supply current (mA)**
(1)	Sensor Node	180 @ 5 V	55 @ 3.6 V
(2)	Soc CC430	27 @ 3.3 V	27 @ 3.3 V
(3)	CPLD input/output	5 @ 3.3 V	6.44 @ 3.3 V
(4)	Sensor	41 @ 5 V	25 @ 2.8 V
(5)	CPLD core	120 @ 5 V	3.2 @ 1.8 V

The evaluation of power consumption for this prototype was mainly done in order to estimate battery life for prospective data acquisition sessions in operating rooms. The 8 hours of continuously operative time of the system has been satisfied by using a battery pack of the capacity about 500 mAh, making it suitable for use during all the typical IRad procedures.

IV.4.1.2 Functional characterization

The functionality of the Prototype 1 is evaluated by comparing the response of single pixel when the MT9V011 sensor has been acquired with two different acquisition systems: the dedicate acquisition system provided by the manufacturer (Demo2 system) and the Prototype 1.

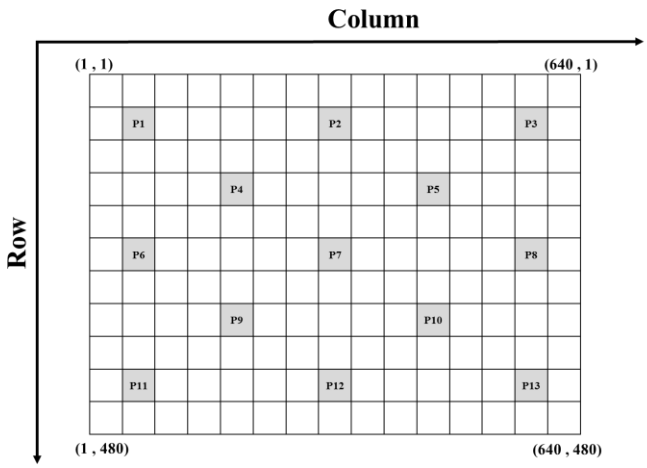

Figure IV-16: Selected pixel’s position in the matrix of the sensor.

A dedicated control firmware for the CPLD has been designed in order to provide the response of the selected pixel by configuring the two coordinates, row and column, in the CPLD register. The homogeneity of the sensor pixels pedestal and noise (Figure III-13) enables to select a subset of pixels in sensor matrix. The chosen subset includes 13 pixels covering geometrically the surface of the sensor matrix as shown in Figure IV-16.

Several acquisitions have been performed by varying two parameters, the environment temperature and the integration time of sensor, as follow:

- environment temperature [15°C, 20°C, 25°C, 30°C];
- integration Time [50 ms, 100 ms, 150 ms, 200 ms, 250 ms].

As first analysis, the central pixel of sensor has been considered for the two acquisition systems at integration time of 100 ms and a fixed temperature of 25 °C. Figure IV-17 shows the distributions of the central pixel while acquiring the sensor with the Prototype 1 and the Demo2 evaluation board.

The mean value and the standard deviation of the distributions have been considered and the absolute error *Q* is obtained as difference between the two mean values of the distributions:

$$Q = X - Y \tag{IV.3}$$

where *X* is the mean value of the Demo2 systems and *Y* is the mean value of the Prototype 1. TABLE IV-4 reports the absolute error and the standard deviation for all the selected pixels at integration time of 100 ms and a fixed temperature of 25°C. All differences lie within $3\sigma_Q$.

The comparison reported in TABLE IV-4 has been extended to all the selected pixels both for the different integration times and temperatures. The results of the comparison for the mean values are in the range of [-0.01, 0.01] with a standard deviation of ± 1.27 confirming the agreement between the two acquisition systems while acquiring the same sensor.

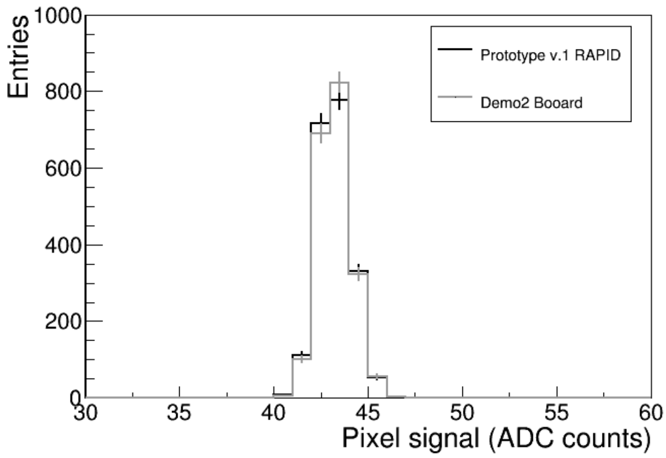

Figure IV-17: Comparison of the central pixel distribution of the mean response in dark conditions acquired with the RAPID prototype and the Demo2 system.

TABLE IV-4
THE ABSOLUTE ERROR AND THE STANDARD DEVIATION OF THE SELECTED PIXELS [INTEGRATION TIME = 100MS; ENVIRONMENT TEMPERATURE = 25°C].

Selected pixel	***Q [ADC Counts]***	σ_Q ***[ADC Counts]***
1	0,00	1,25
2	-0,02	1,28
3	0,00	1,32
4	0,02	1,26
5	0,03	1,29
6	-0,02	1,28
7	-0,02	1,27
8	-0,02	1,27
9	0,00	1,26
10	0,01	1,30
11	0,01	1,28
12	0,00	1,24
13	-0,01	1,27
Mean	-0.0023	± 1.27

IV.4.2 Prototype 1.5

In an effort to improve the portability of the system the wireless interface board has completely been redesigned by using a compact solution for the RF antenna [110]. Figure IV-18 shows the new architecture of the board that hosts the SoC and the RF interface, optimized in size by using a Chip antenna instead of the bulky dipole suitable for a portable device. The Chip Antenna (0868AT43A0020), provided by Johanson Technology works in the frequency range of 858 - 878 MHz and is composed by a Low Temperature Cofired Ceramic (LTCC) material [111].

However the coupling of the dielectric constant of the LTCC package of the antenna with the surrounding objects and human body influences both the antenna gain and the frequency matching point (f_{mp}) causing detuning of the antenna. Therefore, the chip antenna and the matching network, whose recommended operating frequency is 868 MHz, have been extracted from the printed transmitter board, and the antenna detuning has been simulated (and later measured) in the presence of human body.

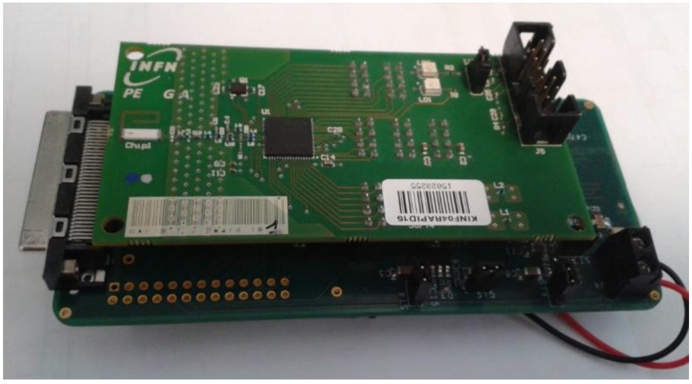

Figure IV-18: Realized transmitter wireless unit with the chip antenna placed on the far left.

A body-equivalent material has been simulated by a stratification of different materials: 1 mm thick skin layer ($\varepsilon_r = 31, \sigma = 8\, S/m$); 4 mm thick fat layer ($\varepsilon_r = 4.6, \sigma = 0.58\, S/m$); 20 mm muscle layer ($\varepsilon_r = 58, \sigma = 1\, S/m$) [112]. The chip antenna physical structure has been modelled by considering multiple loops in a material with high dielectric constant ($\varepsilon_r = 27$) and has been simulated in its installation on the antenna printed board. Figure IV-19 shows the antenna printed board and the artificial body structure realized with the CST (Computer Simulation Technology) electromagnetic simulator software.

The effect of artificial body material to the detuning of the f_{mp} has been simulated in two different scenarios: the first one without artificial body material, the second one with the artificial body material at a distance of 0.5 cm and 1.5 cm with respect to antenna printed board. Figure IV-20 shows the simulation of the reflection coefficient for the different scenarios.

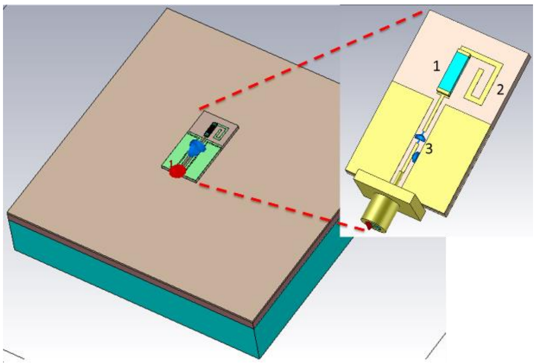

Figure IV-19: The antenna printed board and the artificial body structure. 1) Chip antenna device, 2) printed antenna and 3) matching network.

The simulated structure without the artificial body model shows the f_{mp} equal to 853.6 MHz, in reasonable agreement with the operating frequency of 868 MHz. A reduction of the frequency matching point is observed for decreasing distance between the antennas printed board and the body material.

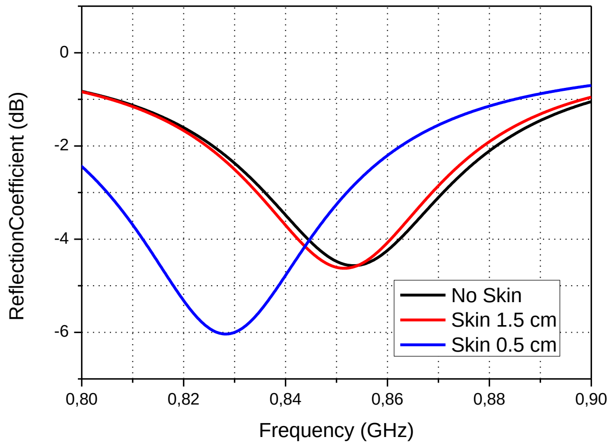

Figure IV-20: Simulation of the antenna reflection coefficient without the artificial body structure and with artificial body structure at two different distances

TABLE IV-5
FREQUENCY MATCHING POINT SHIFT OF THE ANTENNA (SIMULATION RESULTS).

Distance between skin and antenna (cm)	**Frequency shift (%)**
No Skin	0
0.5	-2.97
1.5	-0.25

The simulation provides only a qualitative behavior of the chip antenna performances because the material and the structure of the antenna is unknown. Then the relative frequency shift of the f_{mp} has been considered with respect to the point obtained without the artificial body structure TABLE IV-5 summarizes the percentage of the frequency matching point shift.

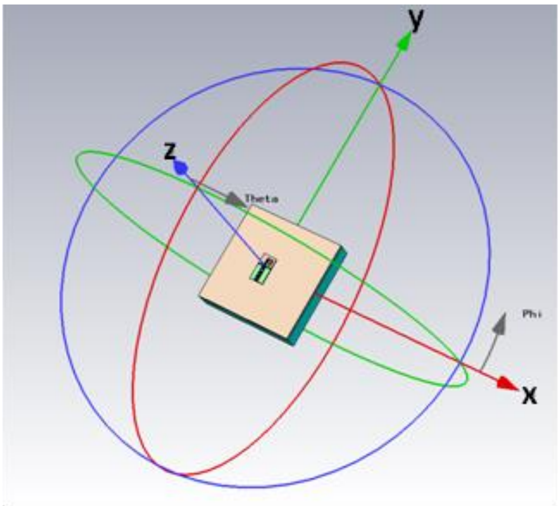

(a)

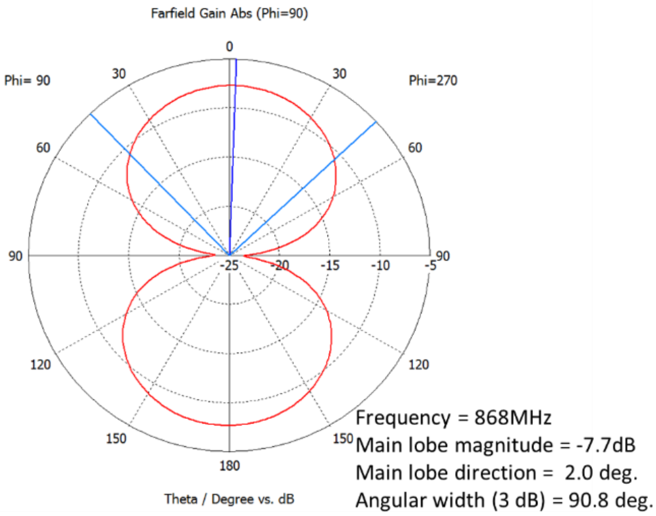

(b)

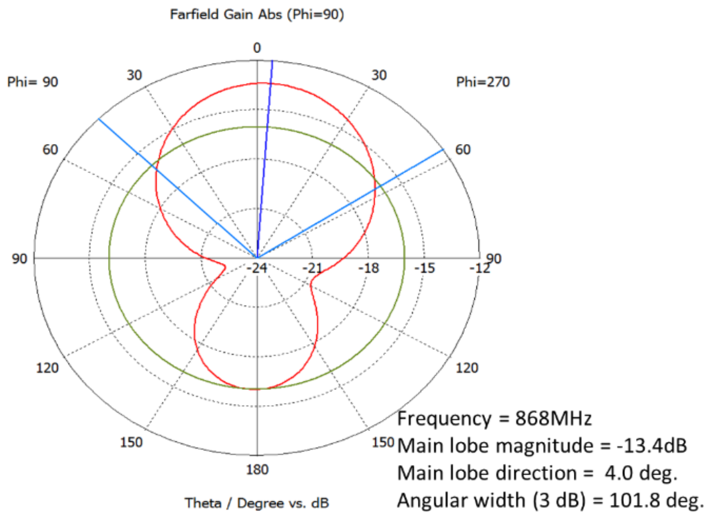

(c)

Figure IV-21: (a) Axis orientation and angles. Antenna radiation pattern and gain, defined from the IEEE standard (IEEE Std 145-1983), (b) free space and (c) including artificial body material.

The detuning can be considered negligible when the antenna is placed at a distance greater than 1.5 cm from the operator body. However, the radiation pattern is also affected by the operator body. Figure IV-21 (a) shows the axis orientation of the radiation pattern while Figure IV-21 (b) and (c) show two different scenarios in free space and with the artificial body material at a distance of 1.5 cm.

The effects of the artificial body structure are a distortion of the radiation pattern of the antenna and a reduction of its gain. The values obtained from the simulation are a radiation gain of -7.7 dB_i for free space radiation and of -13.40 dB_i when the artificial body is at 1.5 cm. Nevertheless, the distorted radiation pattern clearly shows the radiation lobe outside the operator body (Figure IV-21 (c)).

In order to measure the effect of the operator’s body on the performance of the antenna, a test board consisting of the chip antenna and the matching network has been realized (Figure IV-22). The reflection coefficient has been measured with a Vector Network Analyzer and the results are reported in Figure IV-23.

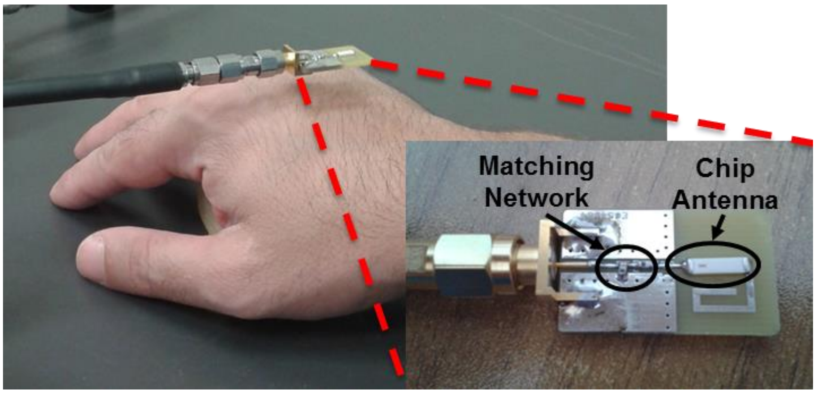

Figure IV-22: The Chip Antenna test board prototype.

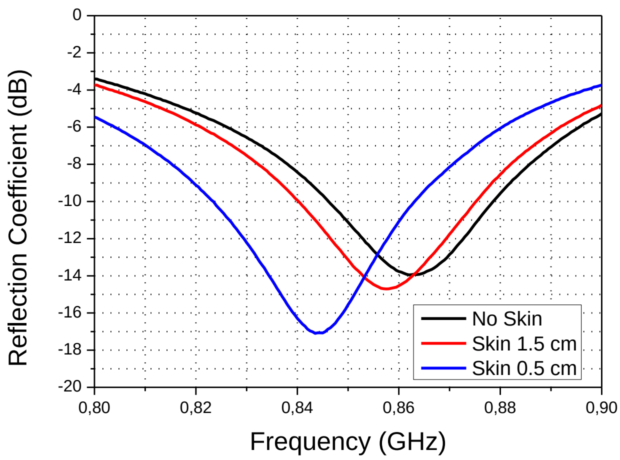

Figure IV-23: Measured antenna reflection coefficient without the operator's hand and with the operator's hand at two different distances.

Figure IV-23 shows the effect to the detuning of the reflection coefficient due to the operator's hand position. Unfortunately, the measurement on biological living body is not completely reproducible with the simulator, however the results show that the measured detuning effect on the reflection coefficient of the antenna is in reasonable qualitative agreement with the simulations and the effect of the operator's hand is negligible at distance greater than 1.5 cm.

In the next section we report about the characterization of the wireless interface by comparing the performances of the system while hosting the wireless interface with the bulky dipole and the optimized wireless interface with the chip antenna.

IV.4.2.1 Wireless interface performances

The comparison of the performances of the wireless interface has been performed by measuring the Packet Error Rate (PER). The PER is defined as:

$$PER = \frac{P_{loss}}{P_{total}} \cdot 100\% \qquad \text{(IV.4)}$$

where P_{loss} is the number of incorrectly received data packets and P_{total} is the number of all sent packets [113]. The NUM_FRAME counter has been used to determine the P_{total} and the P_{loss} values. It should be underlined that the lost packets were measured by setting a Transmitter Power Output of 0 dBm, which is compliant with the IEC 60601-1-2 standard [114].

In the next paragraph the PER measurements were performed in different environment conditions such as open space or operating room.

A. *Measurements in open space and line of sight*

This experiment has been carried out in open space and in line of sight considering the receiver unit in fixed position while the PSN is moved at various distances in a specific range between 1 m and 11 m, which corresponds to the typical dimension of an operating room (10 m). Data have been acquired at different distances for one hour, in order to collect sufficient statistics.

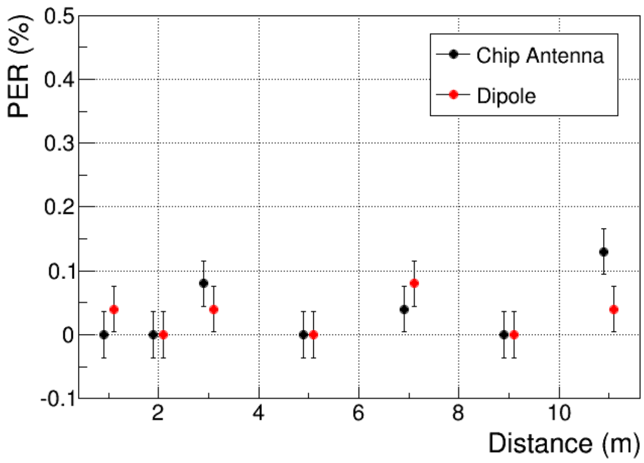

Figure IV-24: Wireless-link PER vs. transmitter-receiver distance considering the Chip and Dipole Antennas with 868 MHz carriers.

The measured PER is lower than 0.1% in the considered distance range (Figure IV-24) for both the Prototype 1 and Prototype 1.5.

The different performance becomes significant at 13 m (not shown in Figure IV-24): the PER for the dipole antenna is 0.12%, whereas for the chip antenna it increases to 15%. In the range less than the typical dimension of an operating room, the performance are comparable then the chip antenna can be used for our application.

B. *Operating room*

A series of measurements has been performed in operating room at the San Giovanni Battista Hospital (Foligno, Italy) fixing the frequency at 868 MHz in order to avoid interference with other devices and to be compliant with the European Standard.

The experimental set-up is shown in Figure IV-25.

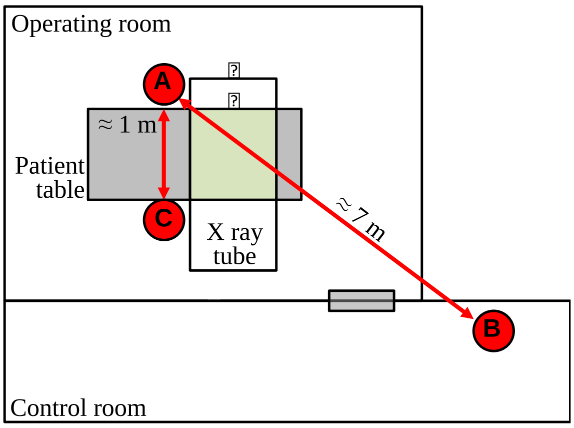

Figure IV-25: Experimental set-up at the San Giovanni Battista Hospital (Foligno, Italy): A = transmitter unit; B = receiver outside the operating room; C = receiver inside the operating room.

The operating room features special walls which shield from X ray radiation introducing RF signal attenuation [115]. For this reason, two different scenarios were considered. The transmitter unit (A) has been hosted in a holder and placed in a fixed position near the X ray tube in order to emulate the position of medical operator. In the first scenario, the receiver (B) is placed outside the operating room at a distance of about 7 m from the transmitter unit. In the second scenario, instead, the receiver (C) is placed inside the operating room: this removes signal attenuation caused by special walls and relative distance between transmitter and receiver unit due to the size of the operating room.

By considering these two scenarios, the amount of lost packets has been determined as a function of time for the two different positions of the receiver. The comparison between acquisitions with the receiver outside and inside the operating room confirms the attenuation of wall, as a matter of fact the PER when the receiver is outside the room is about 3% for different acquisitions and procedures. On the other hand, the set-up with the receiver unit inside the operating room shows a maximum PER of about 0.05% for all the acquisitions.

IV.4.3 Prototype 2

The final Prototype 2 has been designed integrating all the components in a single board (Figure IV-26).

The final dimensions of the board are $10 \times 5 \times 2$ cm^3 and, once enclosed in a thin plastic case, it will be sufficiently small to be easily wearable by the operator.

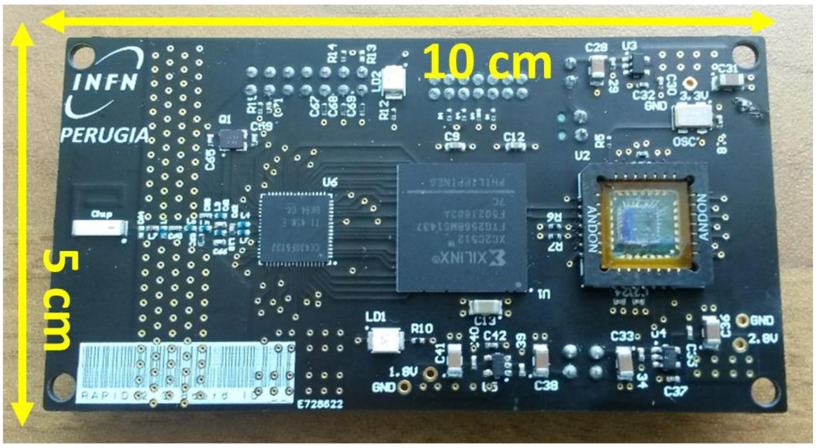

Figure IV-26: The implementation of the final Prototype 2: the chip antenna is placed in the left region, the CPLD and SoC are in the middle and the CMOS image sensor is on the right of the picture

IV.4.3.1 Wireless interface performances

The performance of the transmission antenna has been evaluated in open space by comparing the PER of the three Prototypes. The PER has been evaluated up to 11 m distance, and the measured PER is lower than 0.1% for all of them (Figure IV-27).

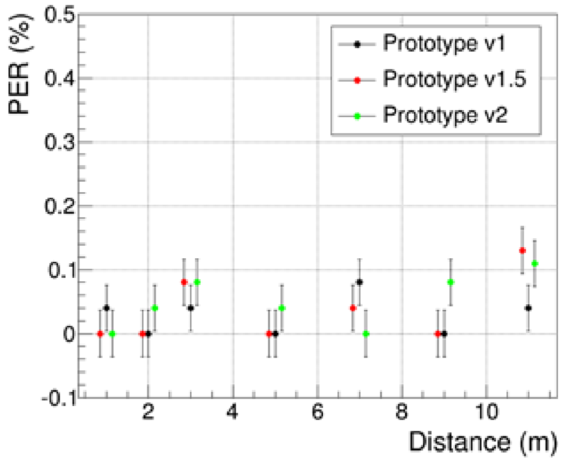

Figure IV-27: Comparison between the PER of the three versions of the Prototypes in open space at different distances up to 11 m between receiver and transmitter unit.

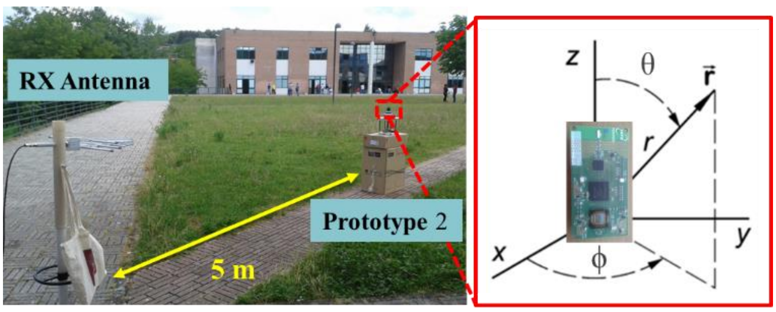

Figure IV-28: Measurement setup in open space for the radiation diagram of the Prototype 2.

The radiation diagram of the Prototype 2 has also been evaluated by using a spectrum analyzer in max-hold configuration to measure the maximum power emitted by the system at 868 MHz. The measurement setup consists of a log-periodic receiving antenna with gain of 7.5 dB_i at 868 MHz placed at a fixed distance of 5 m from the Prototype (Figure IV-28). The Prototype was placed in a holder that can been rotated through 360° degrees.

Two different measurements have been carried out: the first was on the plane perpendicular to the z axis of the chip antenna (ϕ plane, θ=90°), the second on the plane parallel to the z axis (θ plane, ϕ=90°).

The receiving antenna polarization has been kept in agreement with the transmitting antenna polarization that is parallel to the z axis of the chip antenna.

Figure IV-29 (a) shows the received power radiation diagram in the ϕ plane demonstrating, as expected, a circular pattern.

The same kind of measurement has been performed on the θ plane showing the typical dipole radiation pattern with a radiation null along the chip antenna z axis (Figure IV-29 (b)).

Moreover, the influence of the operator body on the antenna performances has been evaluated by measuring the received power when the Prototype 2 has been worn by the operator in the middle of the chest.

TABLE IV-6 summarizes the measurements for the front (0°), rear (180°), left (90°) and right (270°) positions of the Prototype 2 with respect to receiving antenna comparing the results with the received power measured in the front position without the operator body. A small influence of the operator body in the front position and a medium influence on the side positions can be observed while a strong shielding effect of the body for the rear position is evident. The body shielding effect was expected, nevertheless both the front and side positions show good transmission power. This emission behavior represents a useful guide for the installation of the receiver unit inside the operating room [116].

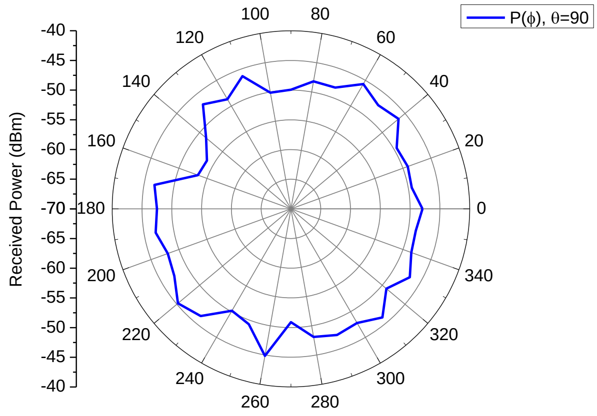

(a)

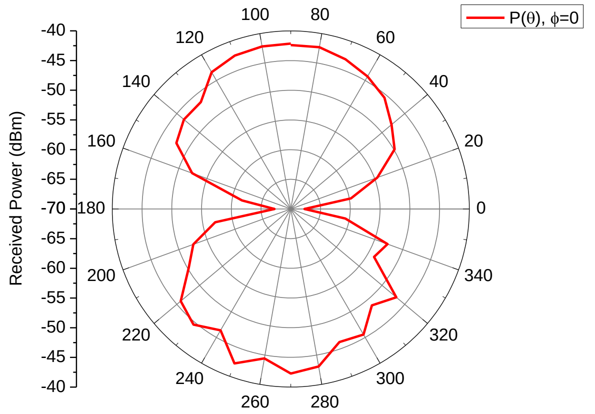

(b)

Figure IV-29: Maximum received power patterns (a) ϕ Plane and (b) θ plane at 868 MHz with the receiving antenna gain of 7.5 dB_i,

TABLE IV-6
RECEIVED POWER FOR THE PROTOTYPE 2 WORN BY THE OPERATOR FOR DIFFERENT POSITION OF THE OPERATOR WITH RESPECT TO THE RECEIVING ANTENNA.

Setup	**Received power (dB_m)**
Front position no body (0°)	-46.64
Front position (0°)	-48.71
Left position (90°)	-51.70
Rear position (180°)	-75.12
Right position (270°)	-53.33

Chapter V

Experimental characterization of the system

This chapter describes the experimental characterization of the RAPID prototypes in different environment conditions such as laboratory and operating room while the system has been exposed to X-ray radiation source. First the prototypes have been characterized in laboratory by comparing the performances of the one-threshold data reduction algorithm with the off-line algorithm applied to the full frames acquired by the Demo2 system. Then, the prototype and the sensor network have also been characterized inside the operating room during several IRad procedures at San Giovanni Battista Hospital (Foligno, Italy), while the operator was performing actual procedures. The wireless losses of the network have been measured and the collected signal has been extracted showing a linearity between the observables. Finally the correlation between the Prototypes and the TLDs has been analyzed and a comparison of the performances with respect to the commercial APDs has been reported.

V.1 Experimental characterization of the prototypes in laboratory

The prototypes have been characterized in laboratory by evaluating the response of the systems to a X-ray radiation beam. The performance of the prototypes has been compared with the Commercial Off-The-Shelf (COTS) acquisition system provided by the manufacture in order to fully validate the functionalities of the prototypes.

The experimental setup is shown in Figure V-1. The prototypes and the Demo2 system were alternatively placed inside the climatic chamber and several measurements have been performed by exposing the systems to a scattered X-ray radiation produced by an Amptek Mini-X device [98] in fluorescence mode with a copper target.

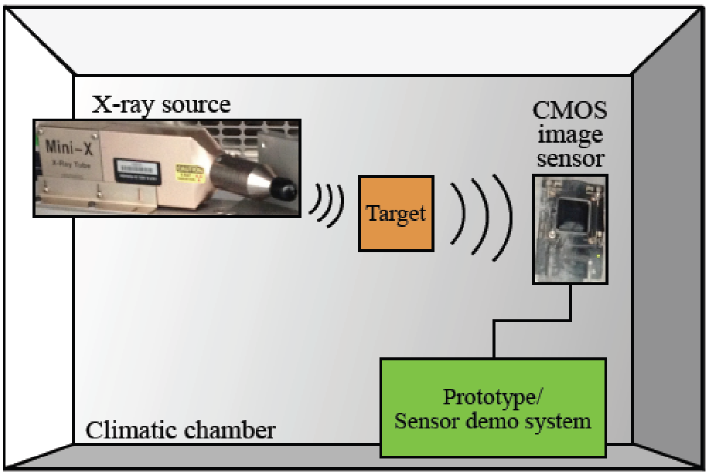

Figure V-1: Experimental setup in thermally controlled environment

V.1.1 The one threshold data reduction algorithm

The one threshold algorithm, implemented in the CPLD, has the aim to use a limited amount of resources to be complaint with the real-time and power consumption requirements of the system. The algorithm is applied it directly to the raw pixel signals expressed in ADC counts and a comparison with an absolute threshold value $V_{threshold}$, has been performed to obtain in dark condition only few pixels over threshold to separate the signal from the background noise.

V.1.1.1 The data reduction algorithm characterization

The algorithm has been characterized in terms of its correlation with the photon counting one. For the characterization, the algorithm has been applied offline to the data acquired in operating room by using a Poly Methyl MethAcrylate (PMMA) phantom to diffuse the X-ray photons from an interventional angiography system. The phantom size is 20 × 20 × 30 cm^3 to simulate the diffusion of X-ray photons from a patient during procedures. The experimental parameters have been varied in order to measure the uncertainty introduced by the simplified algorithm:

- X-ray tube voltage in the range 60–110 kV;
- X-ray tube current in the range 1–4 mA for fluoroscopy in continuous field operation, 50 mA for fluoroscopy in pulsed field operation and in the range 100–800 mA for fluorography;
- pulse rate in the range 5–30 pps and pulse width in the range 1.9–10 ms for pulsed field operation;
- sensor integration time fixed to 100 ms and unitary gain [117].

The N and E observables are plotted in Figure V-2 as a function of the absolute threshold $V_{threshold}$: it can be noticed how both the observables and the error bars decrease as threshold increases.

Then the relative uncertainties have been taken into account, defined for N and E respectively as:

$$\varepsilon_N = \frac{\sigma_N}{N} \tag{V.1}$$

$$\varepsilon_E = \frac{\sigma_E}{E}$$

where σ_N is the uncertainty associated to each point for the *N* observable and σ_E for the *E* observable.

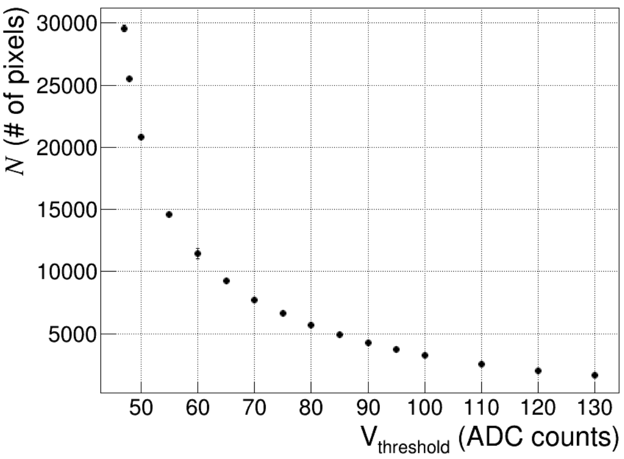

(a)

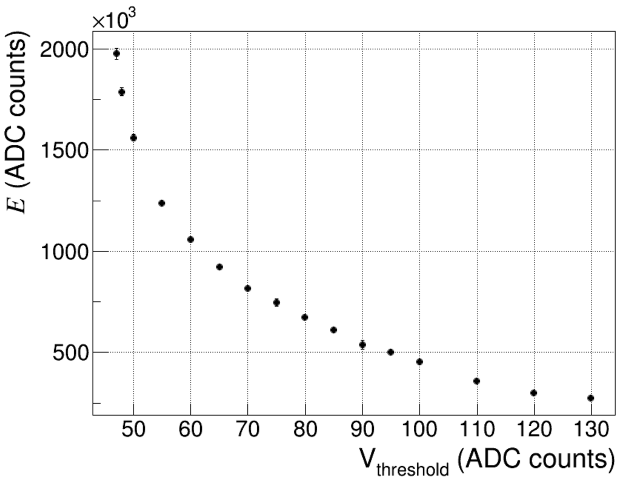

(b)

Figure V-2: (a) Number of pixels above threshold and (b) sum of pixel signals above threshold as a function of the absolute threshold $V_{threshold}$.

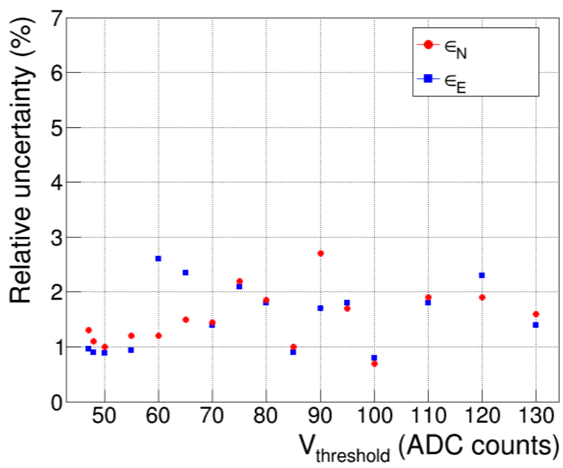

Figure V-3: Uncertainty dependence of the *N* (red bullet) and *E* (green bullet) observables on the absolute threshold $V_{threshold}$ [105].

As already pointed out, the required relative precision in dose measurement of the RAPID system is in the 5–10% range. In the plots in Figure V-3 the results as a function of threshold for both ε_N and ε_E are acceptable (less than 3%), showing no decline in performance for higher $V_{threshold}$.

V.1.2 Algorithm comparison in dark condition

The one-threshold data reduction algorithm has been compared with the off-line algorithm applied to the full frames acquired by the Demo2 system in dark condition without external stimulus. The results of the single pixel response (Section III.4.1) have shown that the sensor is independent from the temperature then a fixed temperature of 25°C has been chosen. The integration time was fixed to 100 ms. The threshold has been varied from 46 to 60 ADC counts moving away to the pedestal value of the sensor, that is around 42 ADC counts, where the fluctuation of the single pixel are lower.

The observables acquired by the prototype (N_P and E_P) has been compared with the observables obtained from the elaboration of the frames acquired by the Demo2 system (N_S and E_S). The minimum variation of the observables has been selected as quantities to compare the results, then as matter of fact the N observable is an integer, the intrinsic minimum variation of this quantities is ± 1 pixel while the minimum variation of the E observable is correlated to that of N.

Plots in Figure V-4 show satisfying agreement between the two systems as the difference of both N and E observables fluctuates within N = ± 1 pixel for all the selected threshold values.

V.1.3 Algorithm comparison with X-ray sources

The performances of the algorithm have also been evaluated while exposing the systems to a X-ray source. A temperature of 25°C, integration time of 100 ms and threshold values between 49 and 110 ADC counts have been considered. The configuration settings for the X-ray tube are 40kV and 90µA in fluorescence mode with a copper target.

The minimum value of the threshold (49 ADC counts) has been selected in order to reduce the statistical fluctuation of the pixel response by considering few pixels over threshold without signal in order to consider only the contribution of the pixel signal.

The difference for both N and E observables is plotted as a function of threshold in Figure V-5. The results are all contained within N = ±1 arbitrary units, showing the agreement of the prototype with the Demo2 system.

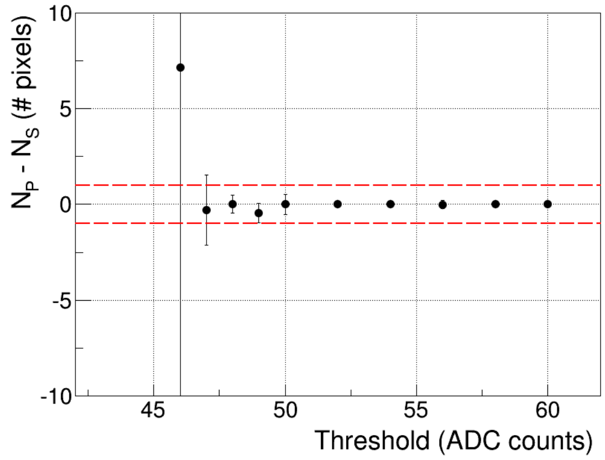

(a)

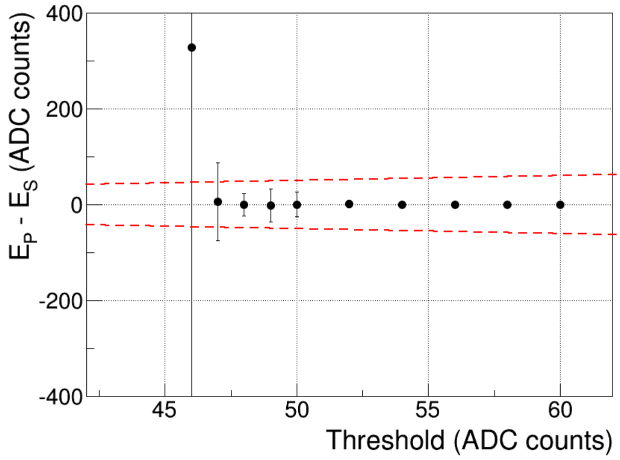

(b)

Figure V-4: Difference of observables (a) *N* and (b) *E* between the RAPID prototype and the Demo2 system at 100ms integration time, 25°C temperature and dark condition.

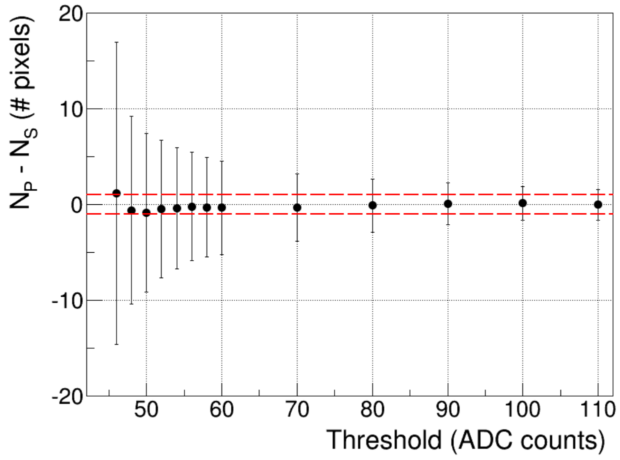

(a)

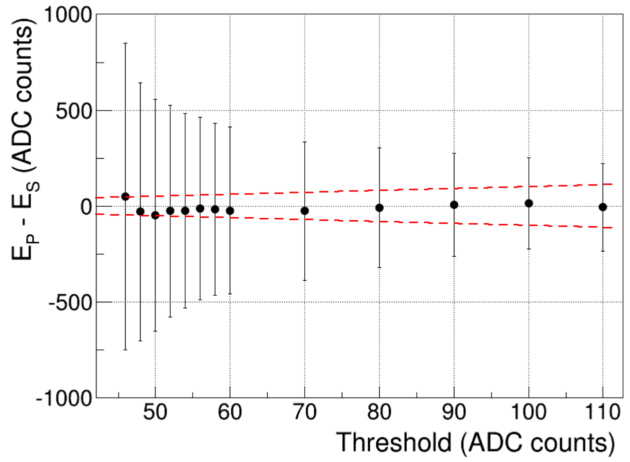

(b)

Figure V-5: Difference of observables (a) *N* and (b) *E* between the RAPID prototype and the Demo2 system at 100ms integration time, 25°C temperature and X-ray fluorescence mode 40kV and 90uA

V.1.4 Response of the observables to the X-ray beam

The response of the prototypes has also been evaluated as function of different dose rates in order to evaluate the maximum range limit. The measurements have been carried out by using an X-ray tube (SEIFERT Pantak [118]) that simulates the effect of the diffused X-ray radiation from the patient's body during the IRad procedure. The energy spectrum of the diffused X-ray photons has a lower limit of 15-20 keV and a peak at 37-40 keV [37] then a X-ray tube energy of 100 kV has been chosen in order to have a direct spectrum with a peak in the same energy region.

The system has been exposed to a X-ray beam with a dose rate varied from 0.5 to 3.3 mGy/s measured by using a PTW 31013 dosimeter [119].

The observables of the prototype have been plotted as a function of dose rate (Figure V-6 (a) and (b)).The observables are linearly correlated with the dose rate up to the maximum value that exceeds by a factor eight the most demanding conditions met during IRad procedures. The residual distribution for the two observables (inset of Figure V-6) evaluated with respect to the fitted line shows an average dispersion less than 1 % with the worst deviation less than 3 %.

V.2 Experimental characterization of the prototypes in the operating room

In this section the experimental characterization of the prototypes has been described while the systems are acquired during several IRad procedures at San Giovanni Battista Hospital (Foligno, Italy).

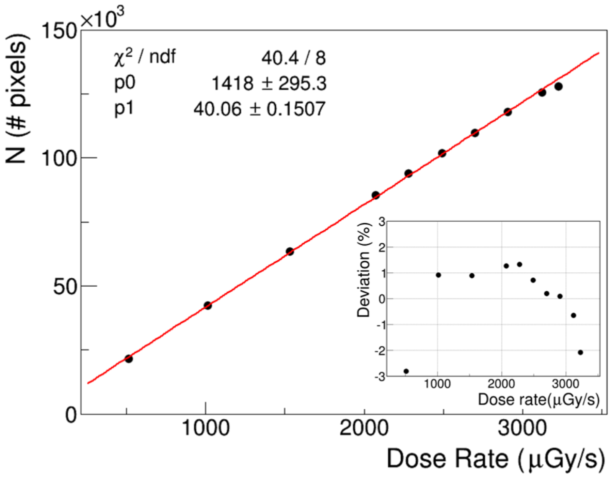

(a)

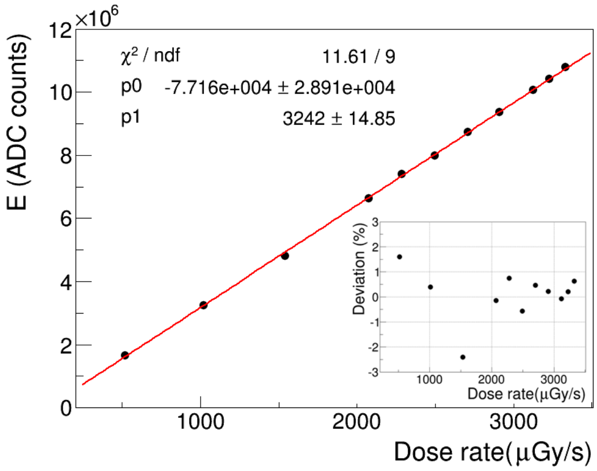

(b)

Figure V-6: Linearity of the response of the *N* and *E* observable as function of dose rate. The insert of the figure shows the residual distribution with respect to the linear fitted line.

The experimental setup is shown in Figure V-7 and it consists of (B) a receiver unit placed inside the operating room and (A) the prototype and the passive TLDs used as dosimetric reference system hosted in a garment worn by the operator.

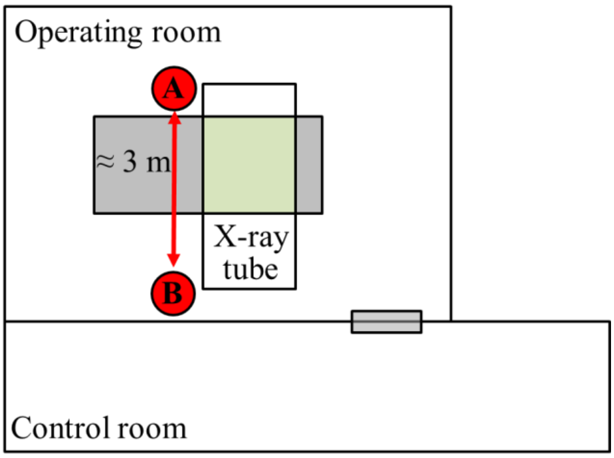

Figure V-7: Experimental set-up at the San Giovanni Battista Hospital (Foligno, Italy): A = transmitter unit; B = receiver inside the operating room.

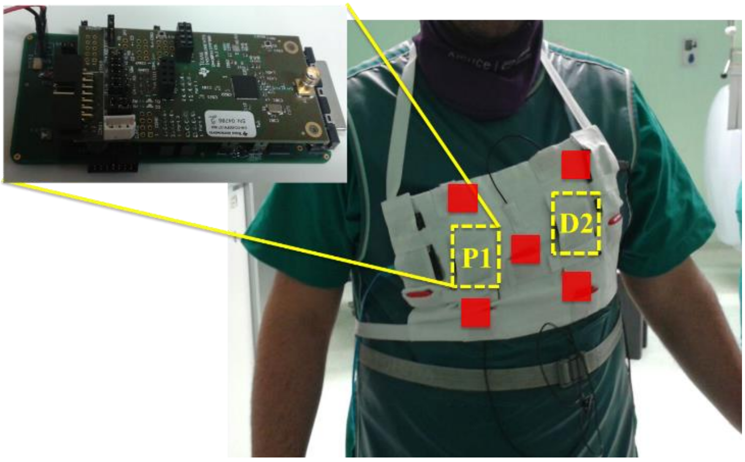

Figure V-8: Custom garment worn by an IRad operator for acquisitions during medical procedures. A = Prototype 1; B = Demo2 system; Red box = TLDs.

V.2.1 Comparison of the performances between the Prototype 1 and the Demo 2 system

The performances of the Prototype 1 has been compared to the Demo2 system (D2) during five IRad procedures. The operator (Figure V-8) wears a garment that hosts the Prototype 1 (P1) and the Demo2 (D2) plus 5 passive TLDs placed around the garment highlighted with the red box.

The TLDs, used as dosimetric reference system in IRad procedures for measuring the dose absorbed, gather the distribution of the X ray radiation field at the level of the chest of the operator. Figure V-9 shows the distribution of the diffused X-ray radiation field that is higher in the left part of the garment where the Demo2 system has been placed while it is lower in the right part where the Prototype 1 has been placed, as expected because the left side of the operator is closer to the patient body [120].

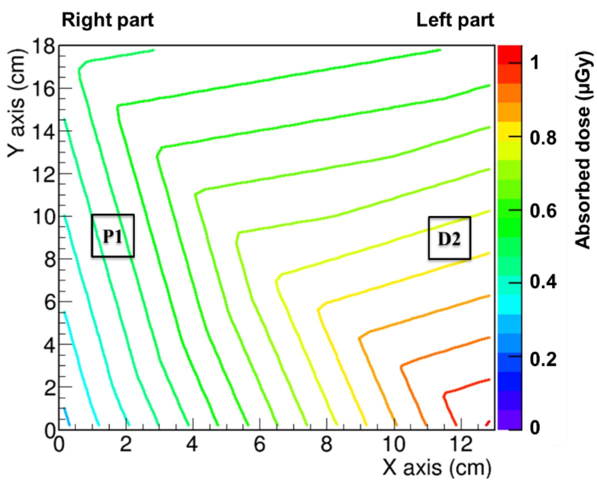

Figure V-9: The radiation field pattern on the garment worn by the operator during one medical procedure.

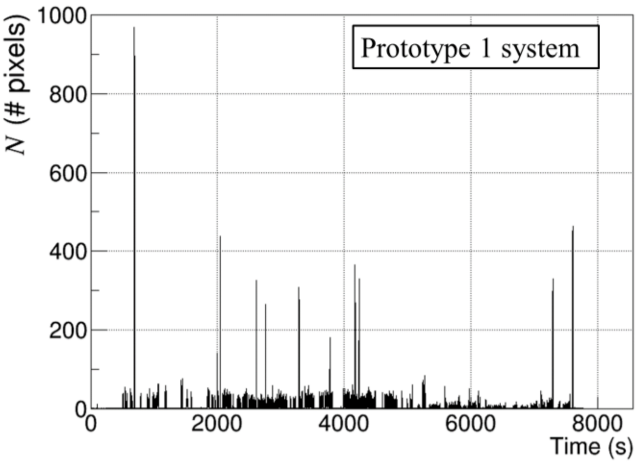

(a)

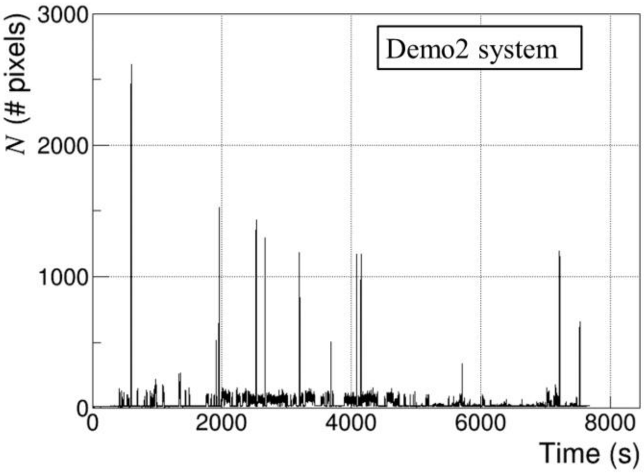

(b)

Figure V-10: The (a) *N* observable acquired by the Prototype 1 and (b) *N* observable acquired by the Demo2 system as function of time for the Uterine varicocele procedure.

The two acquisition systems are used simultaneously during the same acquisition procedure and are capable of following the diffused radiation burst due to the use of the angiograph. The integration time configured to 200 ms is suitable for tracking the pulsed regime during the different procedures, as shown as an example in Figure V-10 (a) and Figure V-10 (b), where each X-ray tube bursts have separately been acquired during the sensor integration time for the *N* observable of the two acquisition systems. In the procedure reported in Figure V-10, three different regimes can be clearly identified: a region where there is no signal and only the background level of noise is measured; regions where the X-ray tube is used in fluoroscopy mode (peaks lower than 100 pixels); regions with high signal peaks generated when the X-ray tube is used in fluorography mode.

A quantitative analysis has been performed, once the two systems have been synchronized with respect to the first peak. A time correlation of the relative maximum of the peaks is not possible due to the following reasons: *i)* the integration interval for the two sensors is still not precisely synchronized (synchronization to ± 1 sensor frame) and the pulsed structure of the X-ray beam (15 to 60 fps) could put a different number of pulses inside the same integration interval, altering the relative height of the peaks with respect to the frame sequence; *ii)* the random loss of a frame due to packet loss in one or the other system spoils the correspondence of frames between the two systems. Moreover, for the Prototype 1 the number of lost frames can be traced by using the sequential counter, while for the Demo2 system this is not feasible.

Hence to study the capability of the two systems to detect the same burst of diffused X-rays, the number of signal frames (NSFs) has been evaluated. In order to discriminate frames where a signal is present from the ones with only noise, the number of frames as a function of the number of pixels over the threshold has been evaluated.

Figure V-11 shows the NSF of Prototype 1 as a function of the number of pixels over threshold. A signal frame has been defined when the number of pixels over threshold is greater than or equal to 3, and the relative difference between the two systems measurements is shown in Figure V-12 for all the medical procedures.

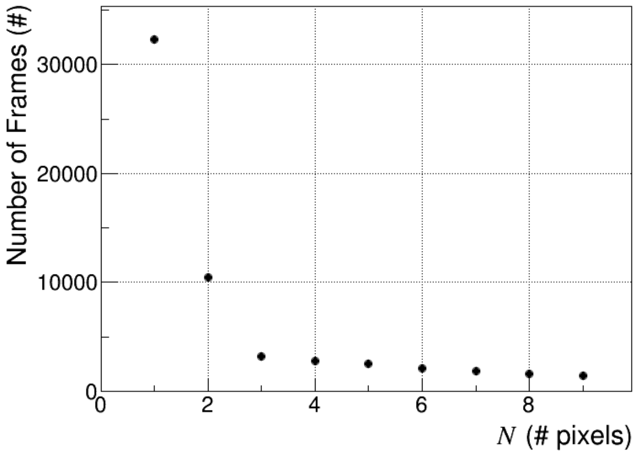

Figure V-11: Number of frames as function of number of pixels over threshold.

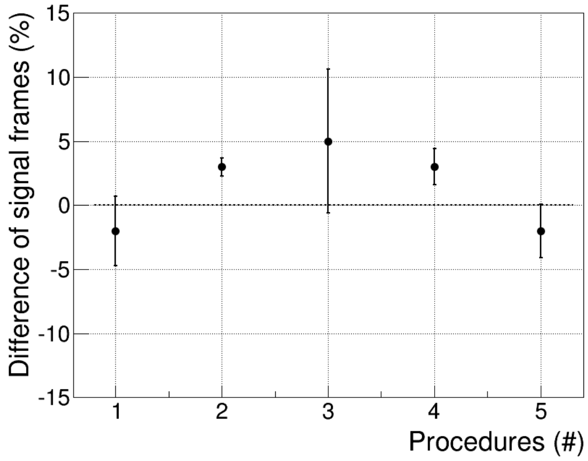

Figure V-12: Difference of number of signal frames between the Demo2 system and the Rapid Prototype 1 for different IRad procedures.

To evaluate the uncertainty of the measurements the set of acquisition frames has been divided in ten sub-sets following a comb-like structure and for each subset the difference $(NSF_{P1}-NSF_{D2})/NSF_{P1}$ has been computed and the RMS of the distribution has been used as error bar. All the points lie within ± 5 % from zero, and the error bars are in the range from 1 % to 5 % (Figure V-12). In two procedures (#2 and #4) the difference observed deviates from zero. This is due to the fact that the Demo2 system acquires more signal frames than the Prototype 1. The difference in these two procedures can be due to several reasons: some signal packets can be lost for the wireless link, geometrical position of the operator with respect to the X ray tube and the patient, non-uniform distribution of the radiation field in the garment. Hence the two systems acquire the same number of frames with signal, within an uncertainty that is compliant with the requirements for the Prototype 1.

V.2.1.1 Signal evaluation

After demonstrating that the two acquisition systems acquire the same NSF during each IRad procedure, the next step has been to evaluate the signal contribution. Figure V-10 shows that the contribution to each observable in the *k*-th frame can be divided in signal (N_{sig} and E_{sig}) and background noise levels (N_b and E_b) as reported in the following equations:

$$\begin{aligned} N_{tot}^k &= N_{sig}^k + N_b^k \\ E_{tot}^k &= E_{sig}^k + E_b^k \end{aligned} \qquad \text{(V.2)}$$

In order to identify the contribution of the signal level in each observable, the background level of the noise of each frame must be removed. The mean value of the background level of the noise has been considered and the equation becomes

$$N_{sig}^{k} = N_{tot}^{k} - \overline{N}_{b} \tag{V.3}$$

where $\overline{N_b}$ is the mean value of the background noise for the N observable. Regarding the E observable the background level of noise consists of the contribution defined in the following equation

$$E_{sig}^{k} = E_{tot}^{k} - \left[\overline{E}_{b} - \left(N_{tot}^{k} - \overline{N}_{b}\right)\cdot V_{ped}\right] \tag{V.4}$$

where $\left(N_{tot}^{k} - \overline{N}_{b}\right)\cdot V_{ped}$ is the contribution of the pixel pedestal to the E observable and $\overline{E}_{b}$ is the mean value of the background noise. The correlation between N_{sig}^{k} and E_{sig}^{k} observable for the Prototype 1 acquired during the Uterine Varicocele procedure is pictured in Figure V-13.

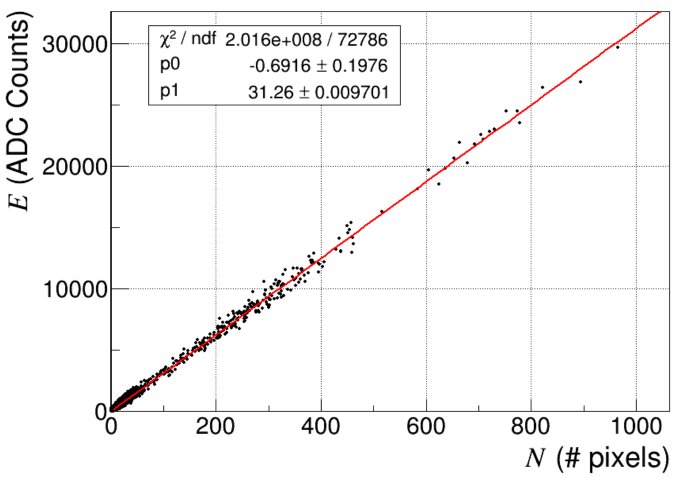

Figure V-13: Correlation between the N and E observables after the subtraction of the noise for the Prototype 1 for each acquired frame in the Uterine Varicocele procedure.

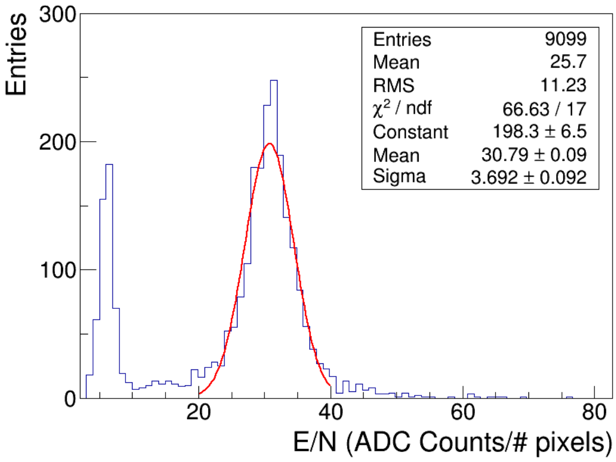

Figure V-14: Distribution of the *E*/*N* ratio when 8 consecutive frames are added to reduce the contribution of the number of X-ray pulses in a single frame.

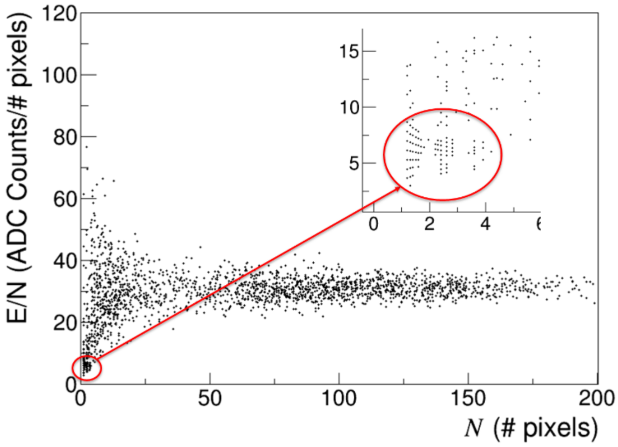

Figure V-15: *E*/*N* ratio as a function of the number of pixels over threshold. The insert zooms the region with few pixels over threshold.

The linear correlation holds up to the highest values of *E* and *N*, corresponding to the fluorography mode, hence the ratio E/N, the mean signal per each pixel over threshold, should be a characteristic variable of the system. In principle this variable is linked to the energy spectrum and the response of the sensor to photons of different energy.

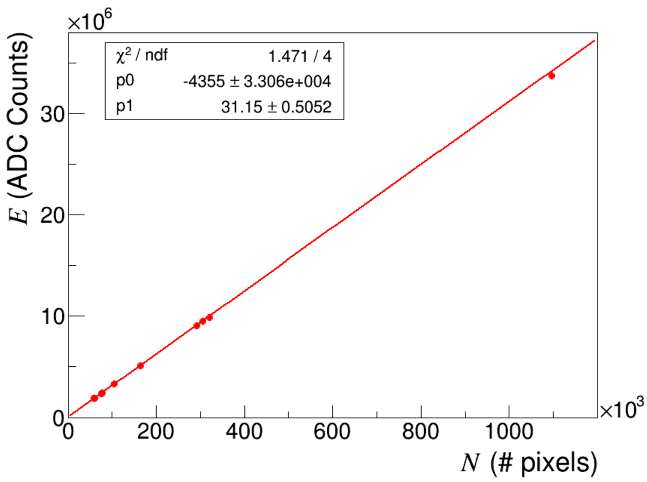

Figure V-16: Correlation between the *E* and *N* observables for all the procedures and for both acquisition systems.

To study this variable we joined the content of 8 consecutive frames to reduce the signal fluctuation due to the pulsed structure of the diffused beam, and built the E/N distribution (Figure V-14) for the Uterine Varicocele procedure.

Two different peaks can be observed, one corresponding to the signal frames (the peak at 31 ADC/pixel) and the other one at about 5 ADC/pixel corresponding to the noise frames. This interpretation is justified by Figure V-15 where the ratio E/N is plotted as a function of *N*. The peak at 5 ADC/pixel is due to frames with few pixels (2-3), i.e. fluctuations due to the noise. The same analysis has been extended to all the procedures and the correlation between the observables is plotted in Figure V-16 considering all the procedures. A good linearity can be observed for all the operating conditions.

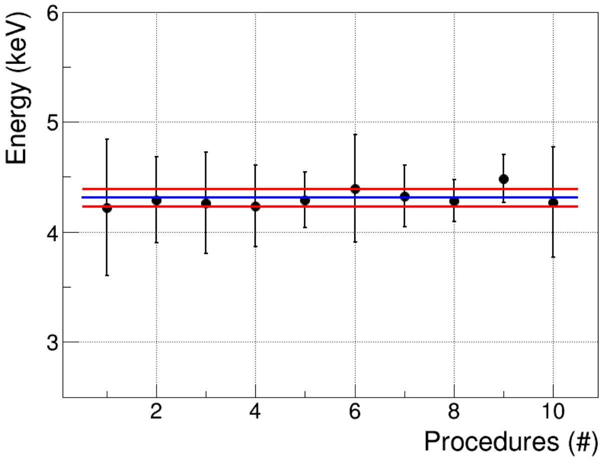

Figure V-17: Collected energy by the photodiode obtained as mean value of the Gaussian distribution as a function of the procedures for the two acquisition systems. The first 5 points are the procedures as measured from the Prototype 1 and the last 5 points are obtained by using the Demo2 system. The blue line and the red lines are the mean value and the uncertainty calculated by considering all the points.

Finally in order to compare the performance of the two acquisition systems we apply the calibration constants found for the two sensors. The mean value of the Gaussian distribution of Figure V-14 that represents the average signal associated to each pixel over threshold could be converted from ADC counts to collected energy (keV) by the pixel photodiode [92].

Figure V-17 shows how the ratio E/N as measured by the two systems for all the medical procedures is essentially constant with a value of collected energy 4.28 ± 0.11 keV/pixel. The results show that the average pixel response does not depend on the procedure, hence does not depend on the different spectra of the diffused radiation. Then the parameter could be used as an indicator of the goodness of the data acquisition for a given procedure.

V.2.2 *Analysis of the performances of the PSNs network with two Prototypes 1*

The sensor network has been characterized inside the operating room during several IRad procedures in order to test the capability of the system to manage more than one dosimeter Prototype working simultaneously in the network while the operator was performing actual procedures.

The operator wears a garment (Figure V-18) hosting two Prototypes 1, called $P1_A$ and $P1_B$, at the level of the chest and two additional TLDs very close to the sensor (less than 1 cm). The close position of the TLDs to the prototypes allows to measure essentially the same dose as measured by the prototypes (see radiation field distribution of Figure V-9.

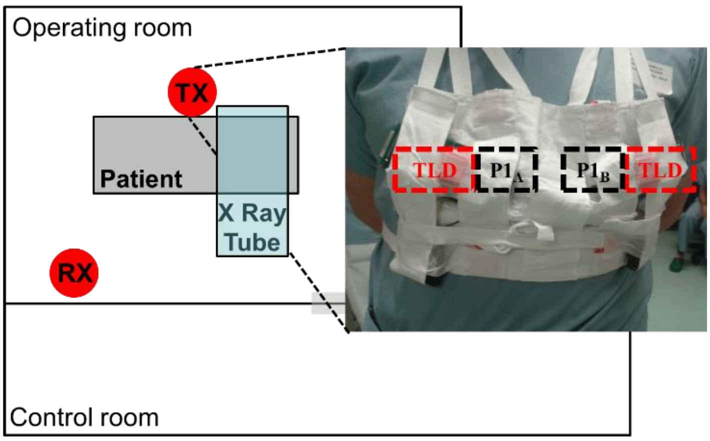

Figure V-18: Measurement setup in operating room during IRad procedures. The insert shows the garment worn by the operator highlighting the position of the two Prototypes 1 and the relative TLDs.

V.2.2.1 Network performances

The PER has been measured in order to evaluate the losses of the network during operating conditions. The distribution of the PER is shown in Figure V-19 for both the Prototypes. The values are almost below 1% while the average value is about 0.25% and a RMS of 0.27% excluding a single high value. The PER is strongly influenced by the actions taken by the operator during the IRad procedures. In fact the operator can walk between the operating room and control room and the PER can increase when the operator stands in the control room because the receiver unit is placed inside the operating room on the other side of the shielding walls.

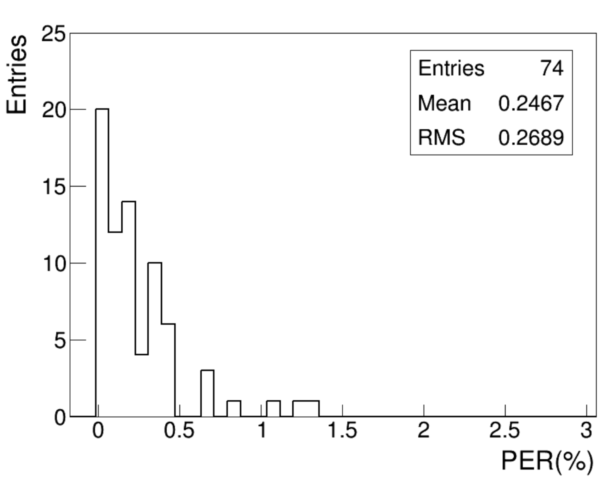

Figure V-19: Distribution of the PER for the two Prototypes 1 for all the considered medical procedures.

Moreover the packets have been lost randomly during the entire procedure and a study of the correlation between the lost packets and the presence of the diffused X-ray radiation has been realized.

Figure V-20 shows the points when one or more packets have been lost for the $P1_A$ (blue line) and the $P1_B$ (red line) as function of time.

The yellow regions represent the time interval where the diffused X-ray radiation is present during the acquisition. We observe no correlation between the lost packets of the two Prototypes hence the two systems work in parallel in the network. Moreover, as expected, there is a higher density of lost packets at the beginning of the procedure, when the operator was entering and exiting the operating room several times due to the medical procedure tasks.

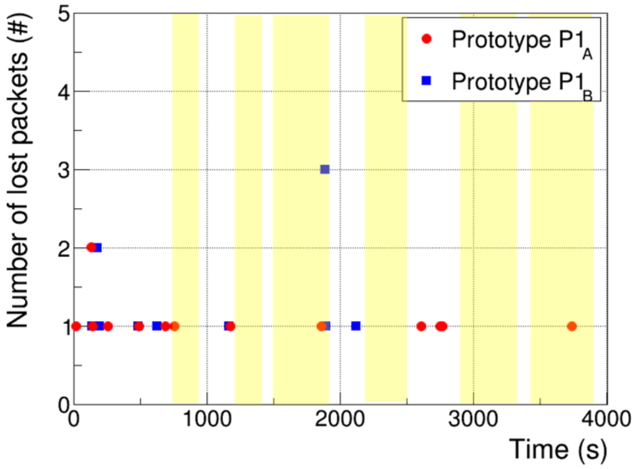

Figure V-20: Number of lost packets between two consecutive received frames as a function of time for the two Prototypes 1 during one medical procedure. The yellow region identifies the presence of the diffused X-ray radiation.

In order to evaluate the correlation of the lost packets with the X-ray diffused radiation, the probable content of the lost packets has been evaluated by considering the value of the preceding and following packets.

The total lost packets for all considered procedures is 232 frames and the 89% of the lost packets are noise frames while only 11% are signal frames.

The presence of the sequential counter inside the transmitted packets allows us to identify the position in time of lost packets. This information can be used to resynchronize the two Prototypes and to verify the level of synchronization between them with respect to the bursts of the diffused X-ray radiation.

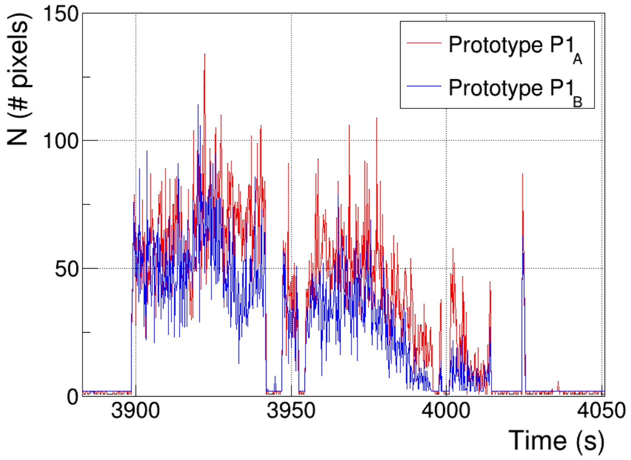

Figure V-21: *N* observable acquired by the two Prototypes 1 during 160 s interval time of a medical procedure.

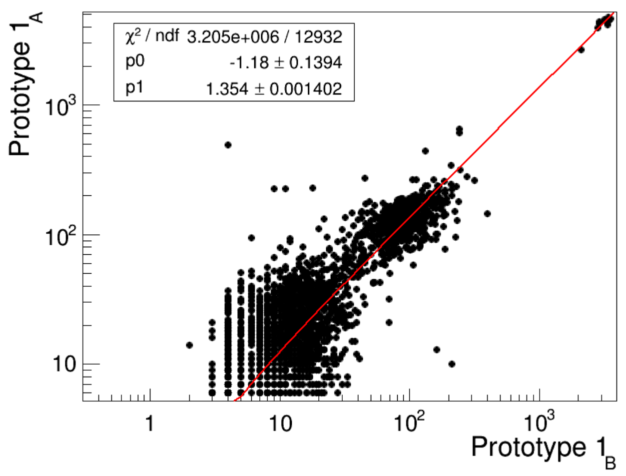

Figure V-22: Correlation for *N* observables acquired by the two Prototypes 1 during the same medical procedure.

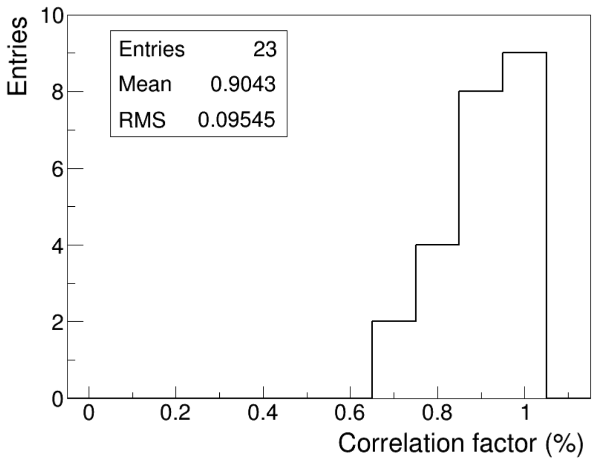

Figure V-23: Correlation factor between the two Prototypes 1 for all the different IRad procedures.

Figure V-21 shows the *N* observable of the two Prototypes, recorded during one part of the procedure, after the resynchronization of the lost packets.

The synchronicity between the two responses is qualitatively evident and the different amplitude of the peaks can be ascribed to the different positions of the Prototypes in the garment of the operator with respect to the patient body and the X-ray tube.

A more quantitative analysis, based on the correspondence between the *N* values of each Prototype, frame by frame, shows a linear correlation between the *N* observable acquired with the two Prototypes in the same procedure (Figure V-22).

Once again is evident the presence of three distinct regions corresponding to no irradiation, fluoroscopy and fluorography modalities. The slope of the correlation is due to the different positions of the two prototypes on the chest of the operator with respect to the diffused radiation field. The correlation factor has been obtained for all the different IRad procedures and the mean value of the distribution (Figure

V-23) is equal to 0.90 % confirming a strong correlation between the two Prototypes 1 while acquiring the same IRad procedure.

V.2.3 Analysis of the performances of the final Prototype 2

The Prototype 2 has been characterized in operating room by using four dosimeters simultaneously worn by the operator in different part of the operator body during several IRad procedures.

The operator wears a garment hosting two Prototypes 2, called $P2_A$ and $P2_B$, at the level of the chest and two wrist garments for the left and right arm hosting respectively the $P2_C$ and $P2_D$ prototypes. Each prototype has an additional TLD used as reference dosimetric system (Figure V-24).

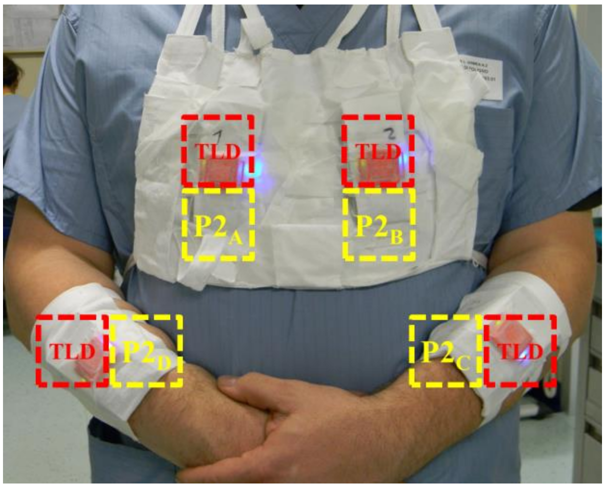

Figure V-24: Measurement setup in operating room during IRad procedures. The operator wear a garment at level of chest with the Prototypes 2 and two garments wrist for the left and right arm.

TABLE V-1 summarizes the position of the prototypes in the operator body and the kind of sensor used for each systems.

The synchronicity between the *N* observable acquired by the four prototypes has been analyzed (Figure V-25).

TABLE V-1
Measurement setup of the dosimeters worn by the operator.

Operator body	Dosimeter	Kind of Sensor
Chest Right	$P2_A$	MT9V011F
Chest Left	$P2_B$	MT9V011C
Left Arm	$P2_C$	MT9V011E
Right Arm	$P2_D$	MT9V011G

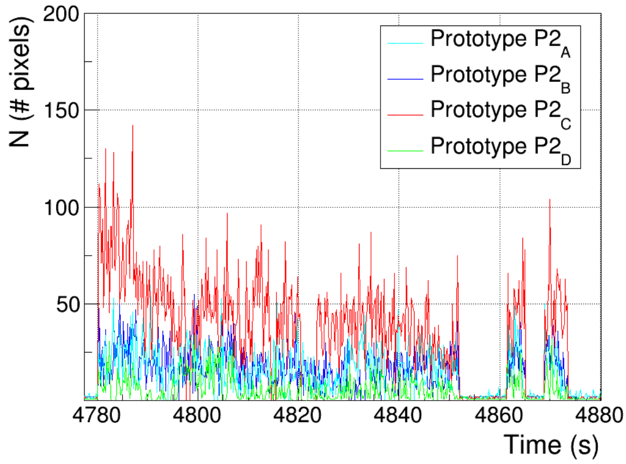

Figure V-25: *N* observable acquired by the four Prototypes 2 during a time interval of a medical procedure.

It should be noted that all the dosimeters are synchronized and follow the burst of the X-ray tube. The different peak amplitudes for the dosimeters can be explained by considering the different positions of the prototypes in the operator's body with respect to the patient and the X-ray tube. The nearest prototype to the X-ray tube and the patients is the one placed on the operator's left arm ($P2_C$) that records the biggest value of the observable.

V.2.3.1 Network performances

The network performances have been evaluated by measuring the PER of the acquisitions performed by all the Prototypes 2. The distribution of the PER is shown in Figure V-26 and it should be noted that the mean value has been increased with respect to the one of the Prototype 1 due to the different design of the wireless interface. However, the values are always below 2.5% while the average value is about 0.83% and a RMS of 0.51%.

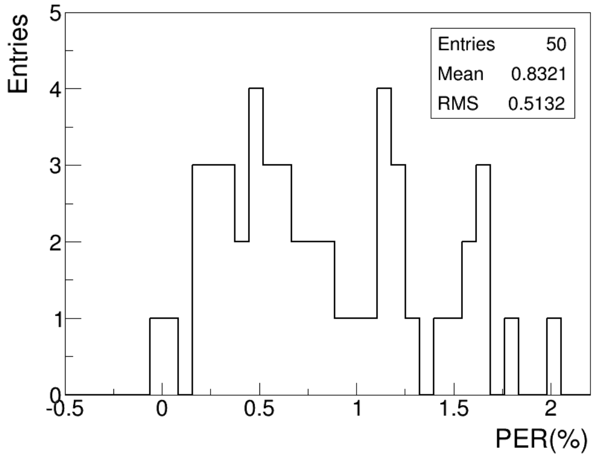

Figure V-26: Distribution of the PER for the four Prototypes 2 for all medical procedures.

V.2.3.2 Signal evaluation

The signal contribution has been extracted for all the IRad procedures (about seventy) and the correlation between the integral value of the observables is plotted in Figure V-27 considering both the Prototype 1 (red points) and Prototype 2 (blue points). A good linearity can be observed for all the operating conditions.

Moreover to compare the performance of all the Prototypes we apply the calibration constants found for each sensors (Section III.5) and we evaluate the mean value of the Gaussian distribution of Figure V-14 for all the operating conditions.

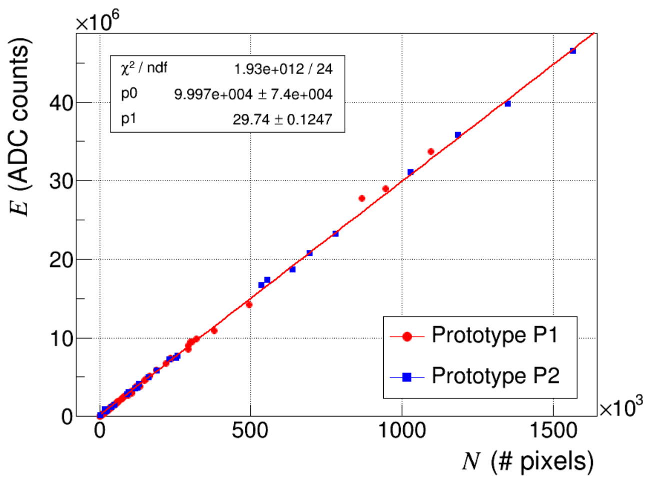

Figure V-27: Correlation between the *E* and *N* observables for all the procedures considering both the Prototypes 1 (red points) and Prototypes 2 (blue points).

Figure V-28 shows the ratio E/N as measured by the Demo2 system, the Prototype 1 and the Prototype 2 for all the medical procedures. The mean value of the ratio is essentially constant with an average collected energy of 4.26 ± 0.03 keV. The results show that the average pixel response does not depend on the procedure, hence does not depend on the different spectra of the diffused radiation. Moreover the average pixel response does not depend on the different acquisition systems.

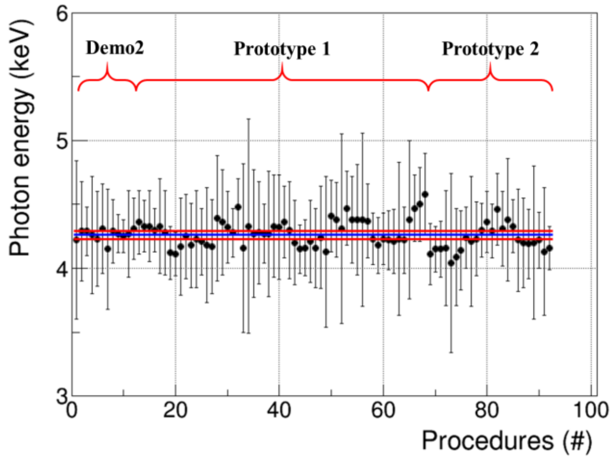

Figure V-28: Energy photons obtained as mean value of the Gaussian distribution as a function of all the procedures by highlighting the results for the different acquisition systems. The blue line and the red lines are the mean value and the uncertainty calculated by considering all the points.

V.2.3.3 Absorbed dose measurement

After the verification of the correlation between the Prototypes, the signal has been evaluated in order to extract the total value of the absorbed dose. The relevance of the lost packets for the dose measurement has been assessed through a dedicated expression which exploits the global counters for the two observables (*N* and *E*). The equation (V.5) measures the ratio between the lost signal value and the total value of acquired signal (the same equation is used for the *E* observable):

$$Ratio = \frac{N_{lost\,sig}}{N_{acquired}} = \frac{N_{Global} - \sum_{k_1} N_{sig}^{k_1} - \sum_{k} \overline{N}_b}{N_{Global} - \sum_{k} \overline{N}_b} \tag{V.5}$$

where $N_{sig}^{k_1}$ is the measured signal in the k_1 received frames and $\overline{N}_b$ is the mean value of the background level of noise. In the denominator, the $N_{acquired}$ value is equal to the difference between the global counter and the average background level of noise multiplied by the number of frames; while in the numerator $N_{lostsig}$ is equal to the denominator minus the integral of the measured signal in the k_1 received frames $N_{sig}^{k_1}$.

TABLE V-2
COMPARISON BETWEEN THE GLOBAL COUNTER AND THE MEASURED VALUE FOR THE *N* OBSERVABLE FOR DIFFERENT IRAD PROCEDURES FOR THE PROTOTYPE 1 AND THE PROTOTYPE 2.

Prototype 1			Prototype 2		
Global counter	Frame counter	Contribution of each lost frame	Global counter	Frame counter	Contribution of each lost frame
99728	99586	28.4	980367	980242	2.3
530701	530577	2.1	154096	153913	36.6
154751	154634	2.1	194116	194039	2.2
181170	200716	229.9	32855	32794	1.2
42791	42766	2.5	48018	48007	2.2
45295	45200	2.1	121484	114997	648.7
26451	26393	2.3	328758	327819	9.36
50006	49954	2.6	78739	78664	1.4
14737	14655	2.3	17249	17224	1.7
12863	12790	2.4	23183	23168	3.0

TABLE V-2 shows, for some example of procedures for both the two Prototypes, the global counter values, the sum of the N observables over the received frames and the contribution of each lost packet to the total value. The lost packets are clearly divided into two categories, the first one due only to noisy frames with no signal and the other one with some signal frames in it.

The global counters can be used to recover the information lost because of the non ideality of the wireless interface. The percentage of the lost signal is below 3.5 % (Figure V-29) with a mean value of 0.45 % and a RMS of 0.82 % showing a contribution of the lost signal comparable with the mean value of the PER.

Finally the correlation between the Prototypes and the TLDs is shown in Figure V-30, where the difference among the error bars of the TLD measurements (about 10%) and the corresponding error bar of our Prototypes that are smaller than the dimension of symbols (dots or squares, order of 2% or less [117]. For both the Prototypes the points lie on the line with slope almost equal to 1, showing that they can be used to perform both a real time monitoring of dose-rate and also to measure the total absorbed dose of the operator [116].

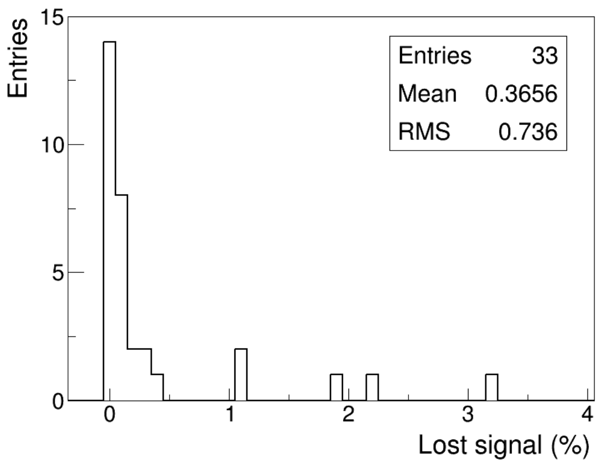

Figure V-29: Distribution of the relative difference between the signal extracted from the global counter and from all the received frames for the *N* observable.

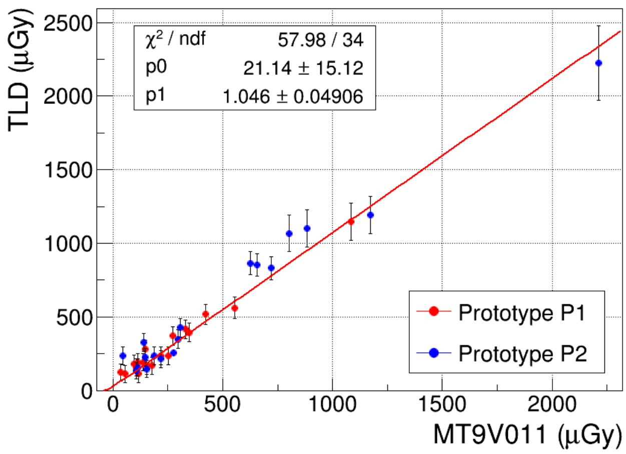

Figure V-30: Correlation among dose as measured by the two Prototypes and by the corresponding TLDs, after correction with calibration constants from certified center. Slope equal to 1 means TLD and Prototype measure correctly the same quantity.

V.3 Comparison with the state of the art

Now that the prototype has reached a final form and the design characteristics needed for real medical procedures have been achieved, it is possible to compare the RAPID system with commercial devices. TABLE V-3 compares the characteristics of the proposed approach with present commercial systems.

For the RAPID system, the energy range values are derived from the dynamic range of the single pixel ADC [92] and the upper limit should be intended as the maximum signal that could be recorded by one pixel without losing response linearity. However, as shown in Figure III-21, each photon signal is shared among several pixels, so the actual energy range is higher. It is worthwhile to underline that the highest settings of the X-ray tube during interventional radiation procedures are at about 120 kV, yielding a maximum photon energy of 120 keV.

TABLE V-3
COMPARISON OF COMMERCIAL ACTIVE PERSONAL DOSIMETERS WITH THE RAPID PROTOTYPE (*ADC DYNAMIC RANGE OF EACH PIXEL OF THE SENSOR; **1 GY=1 SV FOR PHOTONS [61]).

Device name	**Energy range**	**Dose rate range**	**Personal Dose range ($H_p(10)$)**	**Dimensions**	**PSN**
MGPi DMC2000XB [64];	20 keV-6 MeV	1 µSv-10 Sv	0.1 µSv/h-10 Sv/h	87 × 48 × 28 mm^3	no
Thermoscientific EPD Mk2+ [65]	15 - 10000 keV (±20%)	0 µSv/h – 4 Sv/h	0 Sv - 16 Sv	85 × 63 × 19 mm^3	no
Dosilab EDM III [66]	20 - 6000 keV	0.5 µSv/h – 1 Sv/h	1 µSv - 1 Sv	n.a.	no
Unfors EDD-30 [67]	14 - 120 keV (±10%)	0.03 mSv/h – 24 Sv/h	10 nSv - 9999 Sv	6 × 11 × 22 mm^3	no
Atomtex AT3509C [68]	15 -10000 keV	0.1 µSv/h 5 Sv/h	1 µSv – 10 Sv	105 × 58 × 23 mm^3	no
Philips DoseAware [69]	48 - 118 keV (±30%)	40 µSv/h – 300 mSv/h	1 µSv - 10 Sv	45 × 45 × 10 mm^3	yes
RaySafe i2 [70]	33 – 101 keV	40 µSv/h – 300 mSv/h	1 µSv – 10 Sv	45 × 45 × 10 mm^3	yes
RAPID System	2-150 keV*[92]	0.3 µSv/h – 11 Sv/h**[117]	90 pSv - 9999 Sv	50 × 100 × 20 mm^3	yes

Concerning the dose-rate limits, the lower one is calculated asking for a 10% precision in the measurement (100 pixels over threshold) and the upper one is derived from the measurements of Figure V-6. We have also checked the linearity of the response in a certified beam [117] confirming it up to 450 µGy/s, that is already greater than what delivered by the most demanding medical procedures.

The dose sensitivity is essentially the smallest dose that could be recorded in one frame with 10% precision (100 pixels over threshold), while the upper limit is due to the duration of the batteries, being the sensor refreshed after readout of each frame. Hence, for all of the characteristics the RAPID system is better than or at least in the same range of the other commercial devices. Lastly, the angular dependence of the RAPID system has also been measured obtaining a relative efficiency of 50% at ±80°.

Conclusions

A sensor node of a wireless network for the dosimetry of the Interventional Radiology operators has been described. The Personal Sensor Node is based on a commercial CMOS image sensor that has been characterized as sensitive element for X-ray radiation and complies with the energy efficiency requirement of a WSN thanks to the data reduction algorithm implemented in the digital processing unit.

The performances of the CMOS image sensor have been analyzed in laboratory by exposing the system to an X-ray source. A photon counting algorithm has been analyzed for measuring the amount of energy deposited by the impinging photon beam in the sensor as a methodology to obtain dosimetric measurements. Two system observables, the number of pixels over threshold and the sum of the signals of the pixels over threshold, are extracted and correlated with the dosimetric quantities in order to measure the dose absorbed by the operator. A linear correlation between the two observables has been demonstrated, and both could reach a small enough uncertainty in the measurement. The experimental characterization confirms that the observables can be used to measure the dose rate and the total absorbed dose and the response of the sensor is independent from the different IRad procedures, the different parameters of the X-ray tube and from the emitted spectrum because the different response to the sensor to the different energies and the different coefficient to different energies.

Different versions of the system prototype have been produced with the aim to improve the power consumption and the portability of the final system. The total power consumption of the implemented system is compatible with the operative time defined for the specific application and the final dimension is compatible with a portable device.

The network performances have been characterized in different environmental conditions by comparing the different implementations of the Prototypes. The results show that the wireless losses, in the range of 11 m are comparable and are acceptable for the required accuracy in the dose and dose rate measurement of the system. The radiation diagram of the final Prototype has been measured showing a behavior similar to the dipole antenna as expected.

The performance of the network has also been evaluated in operating room during several IRad procedures. The correlation of the measured absorbed dose with respect to the TLD reference dosimetric system shows an overall uncertainty of 2%, well below the standard 10% obtainable by TLDs. Moreover the capacity of the PSN to track the pulse regime of the X-ray tube has been demonstrated thus allowing us to correlate the absorbed dose with the operator’s activity to optimize the unnecessary radiation exposure during the IRad procedures.

Further developments include *i)* the correlation of the measured absorbed dose performed by multiple PSNs placed in different parts of the operator body, i.e. on the chest and the arm; *ii)* the collection of enough procedures with equipped personnel to study the dependence of absorbed dose on operators, procedure's type, relative fraction of fluoroscopy and fluorography time.

References

[1]. J. Yick, B. Mukherjee, and D. Ghosal, "Wireless sensor network survey", *Computer Network*, vol. 52, no.12, pp.2292-2330, Aug 2008.

[2]. Th. Arampatzis, J. Lygeros, and S. Manesis, "A Survey of Applications of Wireless Sensors and Wireless Sensor Networks", in *Proceedings of the IEEE International Symposium on Mediterrean Conference on Control and Automation*, June 27-29, 2005, Limassol, Cyprus, pp 719-724.

[3]. D. Li, K. D. Wong, Y. H. Hu, and A. M. Sayeed, "Detection, classification, and tracking of targets", *IEEE Signal Processing Magazine*, vol. 19, no. 2, pp. 17-29, Mar 2002.

[4]. T. He, S. Krishnamurthy, J. A. Stankovic, T. Abdelzaher, L. Luo, R. Stoleru, T. Yan, L. Gu, J. Hui and B. Krogh, "An energy-efficient surveillance system using wireless sensor networks", in *Proceedings of the 2nd international conference on Mobile systems, applications, and services*, June 6-9, 2004, Boston, USA, pp 270-283.

[5]. P. Zhoua, G. Huanga, L. Zhangb, and K. F. Tsangc, "Wireless sensor network based monitoring system for a large-scale indoor space: data process and supply air allocation optimization" in *Energy and Buildings*, vol 103, 15 September 2015, pp 365–374.

[6]. J. Li, and, E. Xu, "Development on Smart Agriculture by Wireless Sensor Networks" in *Proceedings of 1st International Conference on Industrial Economics and Industrial Security*, Springer US 2015, pp 41-47.

[7]. R. S. Ransing, Fr. C. Rodrigues, and M. Rajput, M, "Smart home for elderly care, based on Wireless Sensor Network", in *International Conference of Nascent Technologies in the Engineering Field (ICNTE)*, 9-10 Jan, 2015, Navi Mumbai, India, pp. 1-5.

[8]. W. Ye, J. Heidemann, and D. Estrin, "An energy-efficient MAC protocol for wireless sensor networks," in *Proceedings of Twenty-First Annual Joint Conference of the IEEE Computer and Communications Societies*, vol. 3, pp. 1567-1576, 2002.

[9]. M. Z. A. Bhuiyan, W. Guojun; C. Jiannong; and W. Jie, “Deploying Wireless Sensor Networks with Fault-Tolerance for Structural Health Monitoring,” in *IEEE Transactions on Computers*, vol. 64, no. 2, pp. 382-395, 2013.

[10]. M. Magno, T. Polonelli, L. Benini, and E. Popovici, “A Low Cost, Highly Scalable Wireless Sensor Network Solution to Achieve Smart LED Light Control for Green Buildings,” *IEEE Sensors Journal*, vol 15, no. 5, pp. 2963-2973,2015.

[11]. ECA table, “The European table of frequency allocations and application in the frequency range 8.3 kHz to 3000 GHz” [Online]. Available: http://www.erodocdb.dk/Docs/doc98/official/pdf/ERCREP025.PDF

[12]. N. K. Kapoor, S. Majumdar, and B. Nandy, “Techniques for Allocation of Sensors in Shared Wireless Sensor Networks, ” *Journal of Networks*, vol 10, no. 1, 2015.

[13]. K. Kinsella, and D.R. Phillips, “Global aging: the challenge of success”, Population Bulletin, 60 (2005) [Online]. Available http://www.prb.org/pdf05/60.1globalaging.pdf

[14]. World Health Organization page, [Online]. Available: http://www.who.int/en/

[15]. T. Gao, C. Pesto, L. Selavo, and C. Yin, “Wireless Medical Sensor Networks in Emergency Response: Implementation and Pilot Results,” *IEEE Conference on Technologies for Homeland Security*, 12-13 May, 2008, Waltham, USA, pp 187-192.

[16]. Y. Hao and R. Foster, “Wireless body sensor networks for health monitoring applications,” in *Physiological Measurement*, vol. 29, No. 11, R27, Nov. 2008.

[17]. G. Acampora, D. J. Cook, P. Rashidi, and A. V. Vasilakos, “A Survey on Ambient Intelligence in Healthcare”, in *Proceedings of the IEEE*, vol. 101, no. 12, pp. 2470 – 2494, 2013.

[18]. E. Aarts and R. Wichert, ‘‘Ambient intelligence,’’ in *Technology Guide*, Springer US 2009, pp. 244-249.

[19]. S. Movassaghi, M. Abolhasan, J. Lipman, D. Smith, A. Jamalipour, “Wireless Body Area Networks: A Survey”, in *IEEE Communications Surveys & Tutorials*, vol. 16 , no. 3, pp. 1658-1686, 2014.

[20]. A. Hande, and E. Cem, “Wireless sensor networks for healthcare: A survey”, in *Computer Networks*, vol. 54, no. 15, pp. 2688-2710, 2010.

[21]. E. Jovanov, A. O. D. Lords, D. Raskovic, P. G. Cox, R. Adhami, and F. Andrasik, "Stress Monitoring Using a Distributed Wireless Intelligent Sensor System," in *IEEE Engineering in Medicine and Biology Magazine*, vol. 2, no. 3, pp. 49-55, 2003.

[22]. J.-L. Lin, H. C. Liu, Y.-T. Tai, H.-S. Wu, S.-J. Hsu, F.-S. Jaw, and Y.-Y. Chen, "The Development of Wireless Sensor Network for ECG Monitoring," in *IEEE International Conference of Engineering in Medicine and Biology Society*, 30 Aug.-3 Sept., 2006, New York, USA, pp. 3513-3516.

[23]. T. Shany, S. J. Redmond, M. R. Narayanan, and N. H. Lovell, “Sensors based wearable systems for monitoring of human movement and falls,” in *IEEE Sensors Journal*, vol. 12, no. 3, pp. 658–670, Mar. 2012.

[24]. Y. C. Kan, and C. K. Chen, “A wearable inertial sensor node for body motion analysis,” in *IEEE Sensors Journal*, vol. 12, no. 3, pp. 651–657, Mar. 2012.

[25]. J. Zhu; L. Gao, and X. Zhang, “Preliminary Research on Wearable Healthcare in Ubiquitous Computing Age”, in *International Conference on Computer Science and Software Engineering*, 12-14 Dec., 2008, Wuhan, Hubei, pp 519-523.

[26]. K. Kwak, S. Ullah, and N. Ullah, “An overview of IEEE 802.15.6 standard,” *IEEE International Symposium on Applied Sciences in Biomedical and Communication Technologies (ISABEL)*, 7-10 Nov, 2010, Rome, Italy, pp. 1-6.

[27]. V. Reghunath; and S.K. Sukumaran, “Printed monopole UWB antenna with EBG structure for Wireless Body Area Network”, *IEEE International Conference on Contemporary Computing and Informatics (IC3I)*, 27-29 Nov., 2014,.Mysore, India, pp. 1310-1314.

[28]. H.J. Lee, S.H. Lee, K.S. Ha, H.C. Jang, W.Y. Chung, J.Y. Kim, Y.S. Chang, and D.H. Yoo, “Ubiquitous healthcare service using Zigbee and mobile phone for elderly patients,” in *International Journal of Medical Informatics*, vol. 78, no. 3, pp. 193-198, 2009.

[29]. H. Strey, P. Richman, R. Rozensky, S. Smith, and L. Endee, “Bluetooth low energy technologies for applications in health care: proximity and physiological signals monitors,” in *IEEE International Conference and Expo on Emerging Technologies for a Smarter World (CEWIT)*, 21-22 Oct., 2013, Melville, USA, pp. 1-4.

[30]. A. Lahtela, M. Hassinen, and V. Jylha, “RFID and NFC in healthcare: safety of hospitals medication care”, in *IEEE International Conference on Pervasive Computing Technologies for Healthcare*, 30 Jan.-01 Feb., 2008, Tampere, Finland, pp 241-244.

[31]. E. Y. Song, and K. B. Lee, "IEEE 1451.5 standard-based wireless sensor networks," in *Advances in Wireless Sensors and Sensor Networks*, Springer Berlin, vol. 46, pp. 243-272, 2010.

[32]. J. Ryckaert, P. De Doncker, R. Meys, A. de Le Hoye, and S. Donnay, "Channel model for wireless communication around human body," *Electronics Letters*, vol. 40, no. 9, pp. 543-544, 2004.

[33]. D. Domenicali and M.-G. Di Benedetto, "Performance analysis for a body area network composed of IEEE 802.15.4a devices," in *IEEE Workshop on Positioning, Navigation and Communication (WPNC07),* 22-23 Mar., 2007, Hannover, Germany, pp. 273 –276.

[34]. K. Bilstrup, "A preliminary study of wireless body area networks," tech. rep., *IDE0854*, Halmstad University, Sweden, Aug. 2008.

[35]. E. Vañó, L. González, E. Guibelalde, J. M. Fernández, and J. I. Ten, "Radiation exposure to medical staff in interventional and cardiac radiology," *An international journal of radiology, radiation oncology and all related science,* The British Institute of Radiology, vol. 71, no. 849, 2014.

[36]. A. R. Reeves, R. Seshadri, and S. O. Trerotola, "Recent Trends in Central Venous Catheter Placement: A Comparison of Interventional Radiology with Other Specialties," *Journal of Vascular and Interventional Radiology*, vol. 12, no. 10, pp. 1211-1214, 2001.

[37]. M. Paolucci, D. Battisti, M. Biasini, B. Checcucci, R. Di Lorenzo, A. Esposito, L. Fanò, D. Passeri, P. Placidi, and L. Servoli, "A real time active pixel dosimeter for interventional radiology," *Radiation Measurements,* vol. 46, No. 11, pp. 1271-1276, 2011.

[38]. R. Laitano, "L'importanza delle misure di dose assorbita in radioprotezione e nelle applicazioni mediche delle radiazioni ionizzanti." [Online]. Available:

http://www.tsrmtorinoaosta.org/SharedFiles/Download.aspx?pageid=60&mid=172&fileid=215, 2012. [In Italian]

[39]. A. H. Elgazzar, and N. Kazem, "Biological Effects of Ionizing Radiation," *The Pathophysiologic Basis of Nuclear Medicine*, Springer 2015, pp 715-726.

[40]. F.C.Vinas and H.I.Wilner, "Brain aneurysm imaging." [Online]. Available: http://emedicine.medscape.com/article/337027

[41]. A. Uchino, A. Kato, M. Abe, and S. Kudo, "Association of cerebral arteriovenous malformation with cerebral arterial fenestration," *European Radiology*, vol. 11, No. 3, pp. 493-496, 2001.

[42]. A. Goel, and D. D'Souza "Caroticocavernous fistula." [Online]. Available: http://radiopaedia.org/articles/caroticocavernous-fistula

[43]. "Amptek complete X-ray spectrometer." [Online]. Available: http://www.amptek.com/pdf/x123.pdf.

[44]. V. Tsapaki, S. Kottou, E. Vano, T. Parviainen, R. Padovani, A. Dowling, M. Molfetas, and V. Neofotistou, "Correlation of patient and staff doses in interventional cardiology," *Radiation Protection Dosimetry*, vol. 117, No. 1-3, pp. 26-29, 2005.

[45]. NCRP, "Use of personal monitor to estimate affective dose equivalent to workers for external exposure to low-let radiation (NCRP report no. 122)," tech. rep., *National Council on Radiation Protection and Measurements*, 1995.

[46]. ICRP "International Commission on Radiological Protection", [Online]. Available: http://www.icrp.org/

[47]. ICRU "International Commission on Radiation Units and Measurements", [Online]. Available: http://www.icru.org/

[48]. EURATOM "European Atomic Energy Agency", [Online]. Available: http://www.euratom.org/

[49]. H. Johns and J. Cunningham, The Physics of Radiology. Thomas, 1983.

[50]. ISO, "X and gamma reference radiation for calibrating dosemeters and dose rate meters and for determining their response as a function of photon energy. Part 3: Calibration of area and personal dosemeters and the measurement of their response as a function of energy and angle of incidence," ISO 4037, *International Organization for Standardization*, 1996.

[51]. ICRU, "Fundamental quantities and units for ionizing radiation (report 60)," tech. rep., *International Commission on Radiation Units and Measurements*, 1998.

[52]. C. Wernli, "External dosimetry: operational quantities and their measurement," in *11th International Congress of the International Radiation Protection Association (IRPA)*, pp. 2–17, 2004.

[53]. ICRP, "1990 recommendations of the international commission on radiological protection. ICRP publication 60," tech. rep., *International Commission on Radiological Protection*, 1991.

[54]. AA.VV., "Council directive 97/43/EURATOM of 30 June 1997 on health protection of individuals against the dangers of ionizing radiation in relation to medical exposure, and repealing directive 84/466/EURATOM," *Official Journal of the European Union L*, vol. 180, no. 40, p. 9, 1997.

[55]. UNSCEAR, Sources and effects of ionizing radiation: sources, vol. 1. *United Nations Publications*, 2000.

[56]. AA.VV., "Decreto legislativo 17 marzo 1995, n. 230 - attuazione delle direttive 89/618/EURATOM, 90/641/EURATOM, 92/3/EURATOM e 96/29/EURATOM in materia di radiazioni ionizzanti.," *Gazzetta Ufficiale*, vol. 136 S.O., 1995. [In Italian].

[57]. ISTISAN, “Linee guida per la garanzia di qualità in radiologia diagnostica e interventistica - rapporti ISTISAN 07/26,” tech. rep., *Istituto Superiore di Sanità*, 2007. [In Italian]

[58]. Piccagli, Sghedoni, and Tassoni, “Caratterizzazione dell’irraggiamento del personale medico in chirurgia vascolare,” in *Atti del V Congresso Nazionale AIFM*, 2007. [In Italian]

[59]. R. Corbett, R. Fong, and C. Lewis, “IRPA-10: 10th international congress of the International Radiation Protection Association,” *The British Journal of Radiology*, vol. 74, no. 886, pp. 883–885, 2001.

[60]. ICRP, “Radiological protection and safety in medicine, ICRP publication 73,” tech. rep., *International Commission on Radiological Protection*, 1996.

[61]. ICRP, “2007 recommendations of the international commission on radiological protection. ICRP publication 103,” tech. rep., *International Commission on Radiological Protection*, 2007.

[62]. G. F. Knoll, Radiation detection and measurement. *John Wiley & Sons*, 4th ed., 2010.

[63]. E. Vano, J.M. Fernandez, and R. Sanchez, “Occupational dosimetry in real time. Benefits for interventional radiology”, *Radiation Measurements*, vol. 46, no. 11, pp. 1262-1265, 2011.

[64]. “DMC 2000 | Electronic Radiation Dosimeter” [Online]. Available: https://www.mirion.com/products/dmc-2000-electronic-radiation-dosimeter/.

[65]. “Thermo scientific EPD Mk2+ electronic personal dosimeter product specifications.” [Online]. Available: http://www.thermoscientific.com/content/dam/tfs/ATG/EPD/EPD%20Documents/Product%20Manuals%20&%20Specifications/Radiation%20Measurement%.

[66]. “Dosilab” [Online]. Available: http://www.dosilab.fr/home.

[67]. “Educational Direct Dosimeter.” [Online]. Available: http://www2.unfors.se/products.php?prodkey=55&catid=9.

[68]. AT3509C Personal Dosimeters”, [Online]. Available: http://www.atomtex.com/en/products/personal-dosimeters/at3509-at3509a-at3509b-and-at3509c-personal-dosimeters.

[69]. Making the invisible visible - Philips DoseAware system.” [Online]. Available:http://www.healthcare.philips.com/main/products/solutions/doseaware/index.wpd.

[70]. RaySafe, “RaySafe i2” [Online]. Avaliable: http://www.raysafe.com/Products/Staff/RaySafe%20i2

[71]. T. Bolognese-Milsztajn, M. Ginjaume, M. Luszik-Bhadra, F. Vanhavere, W. Wahl, and A. Weeks, “Active personal dosemeters for individual monitoring and other new developments”, *Radiation Protection Dosimetry*, vol. 112, no. 1, pp. 141-168, 2004.

[72]. I. Clairand, J.-M. Bordy, E. Carinou, J. Daures, J. Debroas, M. Denozière, L. Donadille, M. Ginjaume, C. Itié, C. Koukorava, S. Krim, A.-L. Lebacq, P. Martin, L. Struelens, M. Sans-Merce, and F. Vanhavere, “Use of active personal dosemeters in interventional radiology and cardiology: Tests in laboratory conditions and recommendations-ORAMED project,” *Radiation Measurements*, vol. 46, no. 11, pp. 1252–1257, 2011.

[73]. I. Clairand, J.-M. Bordy, E. Carinou, J. Daures, J. Debroas, M. Denozière, L. Donadille, M. Ginjaume, C. Itié, C. Koukorava, S. Krim, A.-L. Lebacq, P. Martin, L. Struelens, M. Sans-Mercé, and F. Vanhavere, “Use of active personal dosemeters in interventional radiology cardiology: Tests with continuous and pulsed fields in laboratory conditions-ORAMED project,” in *Workshop on optimization of Radiation Protection of Medical Staff* (ORAMED), 2011.

[74]. E. Conti, P. Placidi, M. Biasini, L. Bissi, A. Calandra, B. Checcucci, S. Chiocchini, R. Cicioni, R. Di Lorenzo, A. C. Dipilato, A. Esposito, M. Paolucci, D. Passeri, A. Pentiricci, A. Scorzoni, and L. Servoli, “Use of a CMOS image sensor for an active personal dosimeter in Interventional Radiology,” *IEEE Transactions on Instrumentation and Measurement*, vol. 62, no. 5, pp. 1065–1072, 2013.

[75]. International Electrotechnical Commission (IEC) IEC 61526 (Ed. 3.0, 2010-07), “Radiation Protection Instrumentation. Measurement of Personal Dose Equivalent Hp(10) and Hp(0.07) for X, Gamma, Neutron and Beta Radiation: Direct Reading Personal Dose Equivalent and/or Dose Equivalent Rate Dosemeters”, Geneva (2010).

[76]. L. Servoli, F. Baldaccini, M. Biasini, B. Checcucci, S. Chiocchini, R. Cicioni, E. Conti, R. Di Lorenzo, A. Dipilato, A. Esposito, L. Fanó, M. Paolucci, D. Passeri, A. Pentiricci, and P. Placidi, “Active pixel as dosimetric device for Interventional Radiology,” *Nuclear Instruments and Methods in Physics Research Section A: Accelerators, Spectrometers, Detectors and Associated Equipment*, vol. 720, pp. 26–30, 2013.

[77]. L. Servoli, D. Battisti, M. Biasini, B. Checcucci, E. Conti, R. Di Lorenzo, A. Esposito, L. Fanó, L., M. Paolucci, D. Passeri, A. Pentiricci, and P. Placidi, “An active pixel sensor to detect diffused X-ray during Interventional Radiology procedure,” *Journal of Instrumentation*, vol. 7, no. 04, p. P04004, 2012.

[78]. W. Dulinski, J.-D. Berst, A. Besson, G. Claus, C. Colledani, G. Deptuch, M. Deveaux, A. Gay, D. Grandjean, Y. Gornushkin, A. Himmi, C. Hu, J.-L. Riester, I. Valin, and M. Winter, “CMOS monolithic active pixel sensors for minimum ionizing particle tracking using non-epitaxial silicon substrate,” *IEEE Transactions on Nuclear Science*, vol. 51, no. 4, pp. 1613-1617, 2004.

[79]. E. Fossum, "CMOS image sensors: electronic camera-on-a-chip," *IEEE Transactions on Electron Devices*, vol. 44, no. 10, pp. 1689–1698, 1997.

[80]. R. Turchetta, J. Berst, B. Casadei, G. Claus, C. Colledani, W. Dulinski, Y. Hu, D. Husson, J. L. Normand, J. Riester, G. Deptuch, U. Goerlach, S. Higueret, and M. Winter, "A monolithic active pixel sensor for charged particle tracking and imaging using standard VLSI CMOS technology," *Nuclear Instruments and Methods in Physics Research Section A: Accelerators, Spectrometers, Detectors and Associated Equipment*, vol. 458, no. 3, pp. 677-689, 2001.

[81]. R. Turchetta, A. Fant, P. Gasiorek, C. Esbrand, J. Griffiths, M. Metaxas, G. Royle, R. Speller, C. Venanzi, P. van der Stelt, H. Verheij, G. Li, S. Theodoridis, H. Georgiou, D. Cavouras, G. Hall, M. Noy, J. Jones, J. Leaver, D. Machin, S. Greenwood, M. Khaleeq, H. Schulerud, J. Østby, F. Triantis, A. Asimidis, D. Bolanakis, N. Manthos, R. Longo, and A. Bergamaschi, "CMOS monolithic active pixel sensors (MAPS): Developments and future outlook," *Nuclear Instruments and Methods in Physics Research Section A: Accelerators, Spectrometers, Detectors and Associated Equipment*, vol. 582, pp. 866–870, 2007.

[82]. L. Rossi, P. Fischer, T. Rohe, and N. Wermes, Pixel detectors: From fundamentals to applications. *Springer*, 2006.

[83]. G. Deptuch, J.-D. Berst, G. Claus, C. Colledani, W. Dulinski, Y. Gornushkin, D. Husson, J.-L. Riester, and M. Winter, "Design and testing of monolithic active pixel sensors for charged particle tracking," *IEEE Transactions on Nuclear Science*, vol. 49, no. 2, pp. 601–610, 2002.

[84]. D. Passeri, P. Placidi, L. Verducci, P. Ciampolini, G. Matrella, A. Marras, and G. Bilei, "High-resolution CMOS particle detectors: design and test

issues," in *IEEE Nuclear Science Symposium Conference Record*, vol. 1, pp. 331–334, Oct 2003.

[85]. L. Servoli, G. Bilei, D. Passeri, P. Placidi, D. Biagetti, T. Bianchi, P. Ciampolini, A. Marras, and A. Delfanti, "Test of a MAPS realized in standard non-epitaxial CMOS technology," *Nuclear Instruments and Methods in Physics Research Section A: Accelerators, Spectrometers, Detectors and Associated Equipment*, vol. 581, no. 1—2, pp. 335–338, 2007.

[86]. L Servoli, S Meroli, D Passeri and P Tucceri, "Measurement of submicrometric intrinsic spatial resolution for active pixel sensors," *Journal of Instrumentation*, vol. 8, no. 11, p. P11007, 2013.

[87]. J. H. Hubbell, W. J. Veigele, E. A. Briggs, R. T. Brown, D. T. Cromer, and R. J. Howerton, "Atomic Form Factors, Incoherent Scattering Functions, and Photon Scattering Cross Sections," *J. Phys. Chem. Ref. Data* 4, 471 (1975).

[88]. C. Grupen and B. Shwartz, Particle detectors. *Cambridge university press*, 2008.

[89]. D. Passeri, P. Placidi, L. Verducci, P. Ciampolini, G. Matrella, A. Marras, and G. M. Bilei, "RAPS: an innovative active pixel for particle detection integrated in CMOS technology," *Nuclear Instruments and Methods in Physics Research Section A: Accelerators, Spectrometers, Detectors and Associated Equipment*, vol. 518, no. 1–2, pp. 482–485, 2004.

[90]. D. Biagetti, P. Delfanti, D. Passeri, A. Marras, P. Placidi, L. Servoli, and P. Ciampolini, "CMOS active pixel sensors for soft X-rays detection applications," in *IEEE Nuclear Science Symposium Conference Record*, pp. 3459–3463, Oct 2008.

[91]. L. Servoli, D. Biagetti, S. Meroli, P. Placidi, D. Passeri, and P. Tucceri, "Use of a standard CMOS imager as position detector for charged particles," *Nuclear Physics B - Proceedings Supplements*, vol. 215, no. 1, pp. 228 –

231, 2011. Proceedings of the 12th Topical Seminar on Innovative article and Radiation Detectors (IPRD10).

[92]. L. Servoli, D. Biagetti, D. Passeri, and E. S. Gattuso, “Characterization of standard CMOS pixel imagers as ionizing radiation detectors,” *Journal of Instrumentation*, vol. 5, no. 07, p. P07003, 2010.

[93]. L. Servoli, D. Biagetti, D. Passeri, and E. S. Gattuso, “Use of standard CMOS pixel imagers as ionizing radiation detectors,” in *IEEE Nuclear Science Symposium Conference Record*, pp. 2484–2488, Oct 2008.

[94]. “MT9V011: 1/4-inch VGA digital image sensor features.” [Online]. Available: http://www.aptina.com/assets/downloadDocument.do?id=493.

[95]. T. Michel, M. Böhnel, J. Durst, P. Sievers, and G. Anton, “Low energy dosimetry with photon counting pixel detectors such as Medipix,” *IEEE Transactions on Nuclear Science*, vol. 56, no. 2, pp. 417–423, Apr 2009.

[96]. W. S. Wong, G. Anton, R. Ballabriga, M. Böhnel, M. Campbell, E. Heijne, X. Llopart, T. Michel, I. Münster, R. Plackett, P. Sievers, P. Takoukam, L. Tlustos, and P. Valerio, “A pixel detector ASIC for dosimetry using time-over-threshold energy measurements,” *Radiation Measurements*, vol. 46, no. 12, pp. 1619–1623, 2011.

[97]. M. Weaver, M. Petasecca, M. L. F. Lerch, D. Cutajar, J. Jakubek, S. Pospíšil, and A. B. Rosenfeld, “Dosimetry verification in eye brachytherapy using silicon pixelated detectors,” *Radiation Measurements*, vol. 46, no. 12, pp. 2010–2013, 2011.

[98]. “Miniature X-ray source data sheet.” [Online]. Available: http://www.amptek.com/pdf/minix.pdf.

[99]. “XCOM program tool.” [Online]. Available: http://www.nist.gov/pml/data/xray_gammaraya.cmf.

[100]. S. Oonsiri, C. Jumpangern, T. Sanghangthum, A. Krisanachinda, and S. Suriyapee, “Radiation dose to medical staff in Interventional Radiology,” *Journal of the Medical Association of Thailand*, vol. 90, no. 4, pp. 823–828, 2007.

[101]. D. Magalotti, P. Pisana, M. Paolucci, A. Scorzoni, and L. Servoli “Experimental Characterization of a Wireless Personal Sensor Node for the Dosimetry during Interventional Radiology Procedures,” to be published on *IEEE Transactions on Instrumentation and Measurement*.

[102]. “MSP430TM SoC with RF core data sheet.” [Online]. Available: http://www.ti.com/lit/ds/symlink/cc430f6137.pdf, Sep 2013.

[103]. “Introduction to simpliciTI.” [Online]. Available: http://www.ti.com/lit/ml/swru130b/swru130b.pdf, Dec 2008.

[104]. “Low-power SoC (system-on-chip) with MCU, memory, sub-1 GHz RF transceiver, and USB controller.” [Online]. Available: http://www.ti.com/lit/ds/symlink/cc1111f32.pdf, Jul 2013.

[105]. L. Bissi, P. Placidi, E. Conti, D. Magalotti, M. Paolucci, A. Scorzoni, G. Verzellesi, L. Servoli, and F. Crescioli, “Study of dosimetric observables to be used in active pixel sensor based devices for Interventional Radiology applications,” in *IEEE Nuclear Science Symposium and Medical Imaging Conference (NSS-MIC)*, pp. 1–5, 2013.

[106]. L Servoli, D. Biagetti, D. Passeri, and E. S. Gattuso, “Characterization of standard CMOS pixel imagers as ionizing radiation detectors,” *Journal of Instrumentation*, vol. 5, no. 7, pp. P07003, Jul. 2010.

[107]. E. Conti, P. Placidi, D. Magalotti, L. Bissi, M. Paolucci, A. Scorzoni, and L. Servoli, “A portable dosimetric system based on a CMOS image sensor for radiation protection in Interventional Radiology,” in *IEEE Proceedings of*

International of Instrumentation and Measurement Technology Conference, May 12-15, 2014, Montevideo, Uruguay, pp. 288–292, 2014.

[108]. “MAX 7000 programmable logic device family data sheet.” [Online]. Available: http://www.altera.com/literature/ds/m7000.pdf, 2005.

[109]. “Xilinx XC2C512 CoolRunner-II CPLD programmable logic device family data sheet.” [Online]. Available: http://www.xilinx.com/support/documentation/data_sheets/ds096.pdf.

[110]. D. Magalotti, P. Placidi, M. Dionigi, A. Scorzoni, L. Bissi, L. Servoli, “A Wireless Personal Sensor Node for the Dosimetry of Interventional Radiology Operators, ” in *IEEE Proceedings of International Symposium on Medical Measurements and Applications*, May 7-9, 2015, Torino, Italy, pp. 196-200.

[111]. Johanson Technology Chip Antenna 0868AT43A0020, [Online]. Available: http://www.johansontechnology.com/datasheets/antennas/0868AT43A0020.pdf.

[112]. CST – Computer Simulation Technology, [Online] Available: http://www.cst.com.

[113]. L. Skrzypczak, D. Grimaldi, R. Rak, “Analysis of the different wireless transmission technologies in distributed measurement systems,” *IEEE International Workshop on Intelligent Data Acquisition and Advanced Computing Systems: Technology and Applications (IDAACS)*, pp.673-678, 21-23 Sept. 2009.

[114]. International Electrotechnical Commission. “IEC EN 60601-1-2. Medical electrical equipment. Part 1: General requirements for safety. 2. Collateral standard: electromagnetic compatibility. Requirements and tests,” 2003.

[115]. T.M. Schafer, J. Maurer, J. V. Hagen, and W. Wiesbeck, “Experimental Characterization of Radio Wave Propagation in Hospitals,” *IEEE*

transactions on Electromagnetic Compatibility, vol. 47, no. 2, pp. 304-311, 2005.

[116]. D. Magalotti et al., “Experimental Characterization of a Personal Wireless Sensor Network for the Medical X Ray Dosimetry,” to be published on *IEEE Transactions on Instrumentation and Measurement*.

[117]. D. Magalotti, L Bissi, E Conti, M Paolucci, P Placidi, A Scorzoni and L Servoli, “Performance of CMOS imager as sensing element for a Real-time Active Pixel Dosimeter for Interventional Radiology procedures,” *Journal of Instrumentation*, vol. 9, no. 1, pp. C01036, 2014.

[118]. SEIFERT Pantak X-ray equipment [Online] Available: http://www.ccp14.ac.uk/ccp/webmirrors/commercial/seifert/NewFiles/frampress.html

[119]. PTW 31013 dosimeter [Online] Available: http://www.rpdinc.com/ptw-31013-03cc-semiflex-chamber-973.html

[120]. D. Magalotti et al., “Experimental Characterization of a Wireless Personal Sensor Node for the Dosimetry during Interventional Radiology Procedures,” to be published on *IEEE Transactions on Instrumentation and Measurement*.

Author's Publications

Journals

[1]. P. Daniele et al., "A Two-Tier Monolithically Stacked CMOS Active Pixel Sensor to Measure Charged Particle Direction" *Journal of Instrumentation (JINST)*, vol. 9, Issue 5, pp. 2 - 9, May 2014.

[2]. D. Magalotti et al .,"Performance of CMOS imager as sensing element for a Real-time Active Pixel Dosimeter for Interventional Radiology procedures," *Journal of Instrumentation (JINST)*, vol. 9, Issue 1, pp. 2-12, Jan 2014.

[3]. Serguei Chatrchyan and CMS Collaboration "Description and performance of track and primary-vertex reconstruction with the CMS tracker,". *Journal of Instrumentation (JINST)*, vol 9 May 2014.

[4]. Serguei Chatrchyan and CMS Collaboration "Alignment of the CMS tracker with LHC and cosmic ray data," *Journal of Instrumentation (JINST)*, vol 9, Mar 10 2014

[5]. A. Andreani et al., "The Serial Link Processor for the Fast TracKer (FTK) at ATLAS," *Journal of Instrumentation (JINST)*, vol 9, C11006, November 2014

[6]. L. Servoli et al., "3D Monolithically Stacked CMOS Active Pixel Sensors for Particle Position and Direction Measurements" *Journal of Instrumentation (JINST)*, vol. 10, C01001, Jan 2015.

[7]. S. Citrato et al., "The Associative Memory system for the FTK processor at ATLAS", *PoS - Proceeding of Science*.

[8]. A Andreani et al, "The Associative Memory Serial Link Processor for the Fast TracKer (FTK) at ATLAS," *Journal of Instrumentation (JINST)*, vol. 9, C11006, Nov. 2014

[9]. C. Gentsos et al., “Future evolution of the Fast TracKer (FTK) processing unit” PoS - Proceedings of Science, TIPP2014, 209.

Journals (accepted)

[1]. D. Magalotti et al., “Experimental Characterization of a Wireless Personal Sensor Node for the Dosimetry during Interventional Radiology Procedures,” to be published on *IEEE Transactions on Instrumentation and Measurement*.

[2]. D. Magalotti et al., “Experimental Characterization of a Personal Wireless Sensor Network for the Medical X Ray Dosimetry,” to be published on *IEEE Transactions on Instrumentation and Measurement*.

[3]. D. Magalotti et al., “A Pattern Recognition Mezzanine based on Associative Memory and FPGA technology for Level 1 Track Triggers for the HL-LHC upgrade,” to be published on *Journal of Instrumentation*

International Conferences

[1]. L. Bissi et al., “Study of Dosimetric Observables to be used in Active Pixel Sensor based devices for Interventional Radiology Applications” *in Proc. of IEEE Nuclear Science Symposium and Medical Imaging Conference*, Oct. 27-Nov. 2, 2013, COEX, Seoul, Korea.

[2]. D. Calabrò et al. “The Associative Memory Boards for the FTK Processor at ATLAS”, *in Proc. of IEEE Nuclear Science Symposium and Medical Imaging Conference*, Oct. 27-Nov. 2, 2013, COEX, Seoul, Korea.

[3]. M. Bogdan et al., “Method for Backplane Data Communication with the VME Rear Transition Modules Developed for the ATLAS FTK Project”, *in*

Proc. of IEEE Nuclear Science Symposium and Medical Imaging Conference, Oct. 27-Nov. 2, 2013, COEX, Seoul, Korea.

[4]. W. Billereau et al., “The Associative Memory system for the FTK processor at ALTAS”, *Proceeding at 4th ICATPP Conference on Astroparticle, Particle, Space Physics and Detectors for Physics Applications*, 23 – 27 September 2013 , Como, Italy.

[5]. L. Servoli et al., “Characterization of wireless personal dosimeter prototype for Interventional Radiology medical operators”, *International Conference on Translational Research in Radio-Oncology and Physics for Health in Europe (ICTR-PHE)*, Geneva, Switzerland, vol. 110- Supplement 1, 2014

[6]. E. Conti et al. “A Portable Dosimetric System Based on a CMOS Image Sensor for Radiation Protection in Interventional Radiology”, *in Proc. of IEEE International Instrumentation and Measurement Technology Conference (I²MTC)*, May 12-15, 2014, Montevideo, Uruguay.

[7]. D. Magalotti et al., "Design and Implementation of a Wireless Intelligent Personal Sensor Node for the Dosimetry of Interventional Radiology Operators", *in Proc. of IEEE International Instrumentation and Measurement Technology Conference (I²MTC)*, May 11-14, 2015, Pisa, Italy.

[8]. D. Magalotti et al., “A Wireless Personal Sensor Node for the Dosimetry of Interventional Radiology Operators”, *in Proc. of IEEE International Symposium on Medical Measurement and Application (MeMea)*, May 7-9, 2015 Torino, Italy.

[9]. D. Magalotti et al., “A Wireless Personal Sensor Node for Real Time Dosimetry of Interventional Radiology Operators”, *Applications in Electronics Pervading Industry, Environment and Society*, May 14-15, 2015 Roma, Italy

[10]. G. Fedi et al. “A Pattern Recognition Mezzanine based on Associative Memory and FPGA technology for Level 1 Track Triggers for the HL-LHC upgrade”, *13th Pisa Meeting on Advanced Detectors*, La Biodola, Isola d'Elba, Italy 24-30 May 2015

International Conferences (accepted)

[1]. G. Fedi et al. “A Pattern Recognition Mezzanine Based on Associative Memory and FPGA Technology for Level- 1 Track Triggers for the HL-LHC Upgrade” *2015 IEEE Nuclear Science Symposium and Medical Imaging Conference together*, 31 October – 7 November, San Diego, USA

[2]. D Magalotti et al. “A Pattern Recognition Mezzanine based on Associative Memory and FPGA technology for Level 1 Track Triggers for the HL-LHC upgrade” *Topical Workshop on Electronics for Particle Physics (TWEPP)*, 28 September to 02 October, 2015 Lisbon Portugal.

[3]. C. Christos et al. “The Fast TracKer Processing Unit future evolution” *2015 IEEE Nuclear Science Symposium and Medical Imaging Conference together*, 31 October – 7 November, San Diego, USA

Book chapters

[1]. E. Conti E., D. Magalotti, P. Placidi, L. Bissi, M. Paolucci, D. Passeri, A. Scorzoni, L. Servoli, “A Dosimetric Device Based on a CMOS Image Sensor for Interventional Radiology”, Applications in Electronics Pervading Industry, Environment and Society, Lecture Notes in Electrical Engineering, vol. 289. De Gloria, Alessandro (Ed.) 2014 (ISBN 978-3-319-04369-2).

National Conference

[1]. L. Servoli et al. "RAPID: A prototype for personnel dosimetry during interventional radiology procedures", *abstract AIFM 8° Congresso Nazionale*, 16-19 Novembre 2013, Torino, Italia

[2]. L. Servoli, L. Bissi, A. Calandra, S. Chiocchini, R. Cicioni, E. Conti, R. Di Lorenzo, A.C. Dipilato, D. Magalotti, M. Paolucci, A. Pentiricci, P. Placidi "Analysis of performance of Active Pixel Sensor (APS) as sensing element for a Real-time Active Pixel Dosimeter for Interventional Radiology", *abstract AIFM 8° Congresso Nazionale*, 16-19 Novembre 2013, Torino, Italia

[3]. L. Bissi, L. Servoli, P. Placidi, E. Conti, D. Magalotti, M. Paolucci, A. Pentiricci, R. Di Lorenzo, A. Calandra, S. Chiocchini, R. Cicioni, A.C. Dipilato, "Dosimetric Observables to be used in Active Pixel Sensor based devices for Interventional Radiology Applications", *abstract AIFM 8° Congresso Nazionale*, 16-19 Novembre 2013, Torino, Italia